

Subcutaneous depth-selective spectral imaging with μ SORS enables noninvasive glucose monitoring

Received: 7 May 2024

Accepted: 8 January 2025

Published online: 05 February 2025

 Check for updates

Yifei Zhang^{1,2,8}, Lili Zhang^{3,8}, Long Wang^{1,2,8}, Shuai Shao^{3,8}, Bei Tao^{1,2}, Chunrui Hu³, Yufei Chen^{1,2}, Yue Shen³, Xianbiao Zhang³, Shijia Pan^{1,2}, Hua Cao⁴, Ming Sun³, Jia Shi^{1,2}, Chunhong Jiang^{1,2}, Minghui Chen⁵, Lin Zhou³✉, Guang Ning^{1,2}✉, Chang Chen^{3,6,7}✉ & Weiqing Wang^{1,2}✉

Noninvasive blood glucose monitoring offers substantial advantages for patients, but current technologies are often not sufficiently accurate for clinical applications or require personalized calibration. Here we report multiple μ -spatially offset Raman spectroscopy, which captures Raman signals at varying skin depths, and show that it accurately detects blood glucose levels in humans. In 35 individuals with or without type 2 diabetes, we first determine the optimal depth for glucose detection to be at or below the capillary-rich dermal–epidermal junction, where we observe a strong correlation between specific Raman bands and venous plasma glucose concentrations. In a second study, comprising 230 participants, we then improve accuracy of our regression model to reach a mean absolute relative difference of 14.6%, without personalized calibration, whereby 99.4% of calculated glucose values fall into clinically acceptable zones of the consensus error grid (zones A and B). These findings highlight the ability and robustness of multiple μ -spatially offset Raman spectroscopy for noninvasive blood glucose measurement in a clinical setting.

Blood glucose monitoring is critical for health management, especially for the over 500 million people with diabetes worldwide^{1,2}. Patients with diabetes typically receive recommendations to monitor their blood glucose level multiple times per day³. Nevertheless, conventional finger pricks induce pain and risk of infection, which thereby reduced the patients' quality of life and their adherence to treatment^{4,5}. More recently, minimally invasive continuous blood glucose monitoring technologies have been developed, utilizing indwelling sensors to measure glucose levels in interstitial compartments^{6,7}. However, these sensors require constant attachment to the user and cause inconvenience⁸. Hence, there remains a persistent need for practical solutions to noninvasive blood glucose monitoring⁹.

So far, the route to clinically applicable noninvasive blood glucose monitoring remains elusive^{10,11}. Among the various approaches,

including iontophoresis¹², transdermal impedance spectroscopy¹³, photoacoustic spectroscopy^{14,15} and infrared spectroscopy^{16,17}, Raman spectroscopy is highly anticipated due to its direct identification of glucose molecules with high specificity by spectral information^{18–22}, along with its selectable wavelengths for deep penetration in human skin. Recently developed paraboloidal mirror Raman¹⁸, confocal Raman¹⁹ and spatially offset Raman spectroscopy (SORS)²² have shown promising results for noninvasive blood glucose testing. However, these Raman spectroscopy methods require subject-specific training to build a proper mathematical model for each user, introducing additional procedures in practical applications. The main hindrance to higher robustness and accuracy in Raman spectroscopic measurements is the broad and strong fluorescence background signal from the skin surface. Therefore, a Raman spectroscopy method to reduce

A full list of affiliations appears at the end of the paper. ✉e-mail: lin.zhou@photoniview.com; gning@sibs.ac.cn; changchen@sjtu.edu.cn; wqingw@shsmu.edu.cn

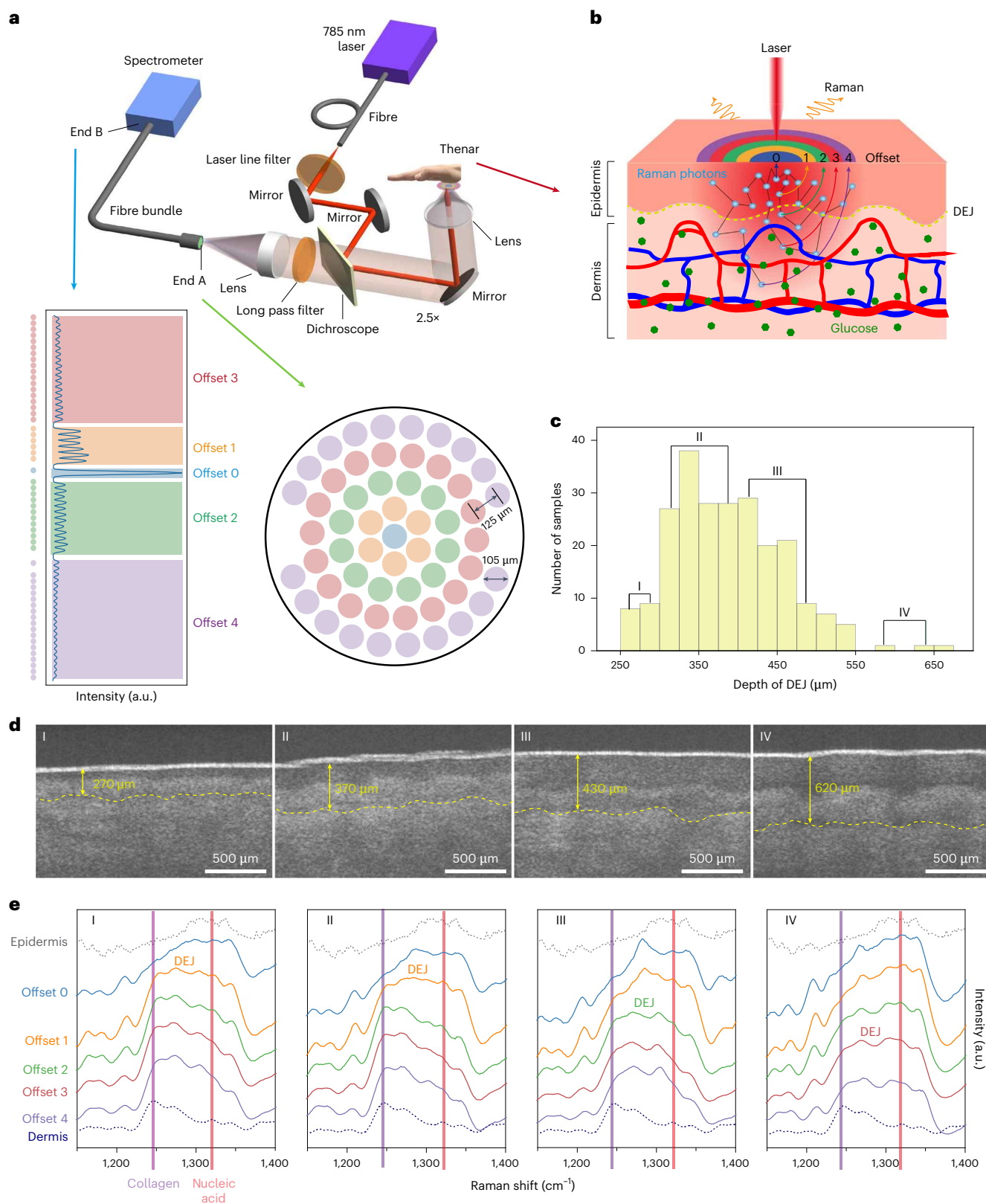


Fig. 1 | μ SORS system detects Raman signals from epidermis to dermis with depth selectivity. **a, Schematic of μ SORS system. μ SORS setup (top). Zoomed-in layout of fibres in the fibre bundle at End A (bottom right). Typical intensity profile across offsets 0–4 in the fibre bundle at End B (bottom left). **b**, Schematic of μ SORS detection on thenar. Yellow dashed curve indicates DEJ; green hexagons show glucose molecules; cyan dots indicate Raman photons. Schematics of blood vessels and skin layers were adapted from ref. 47 with permission. **c**, Histogram of DEJ depths from 232 human thenar samples**

identified by OCT. Roman numerals (I–IV) indicate four different depth ranges of DEJ, corresponding to OCT images in **d**. I, 250–300 μ m; II, 300–400 μ m; III, 400–500 μ m; IV, 575–600 μ m. **d**, Typical OCT images of four samples with mean DEJ depths of 270 μ m, 370 μ m, 430 μ m and 620 μ m were selected from I–IV marked in **c**. **e**, μ SORS spectra from the same samples in **d**, along with reference Raman spectra taken from ex vivo epidermis and dermis samples of human skin. Pink and purple shades indicate characteristic Raman peaks of nucleic acid and collagen.

Table 1 | Detection depth of each offset gauged by OCT and μ SORS spectra

Samples	I	II	III	IV	Depth (μ m)	Suitable
Thickness (μ m)	270	370	430	620	Depth (μ m)	Suitable
Offset 0	Epidermis	Epidermis	Epidermis	Epidermis	<270	0
Offset 1	Mix	Mix	Epidermis	Epidermis	270–370	46%
Offset 2	Dermis	Dermis	Mix	Epidermis	370–430	72%
Offset 3	Dermis	Dermis	Dermis	Mix	430–620	99%
Offset 4	Dermis	Dermis	Dermis	Dermis	>620	100%

Table 2 | Statistics of the 35 participants in the preliminary BESH

Statistics	Preliminary BESH (n=35)	
Participants (n)	With T2D (n=20)	Without diabetes (n=15)
Sex, male: female (%)	17 (85.0): 3 (15.0)	8 (53.3): 7 (46.7)
Age, years (mean \pm s.d., range)	47.6 \pm 8.4, 30–60	35.7 \pm 3.8, 30–60
BMI, kg m^{-2} (mean \pm s.d., range)	24.5 \pm 4.1, 17.7–31.8	24.3 \pm 4.0, 19.2–32.7
FPG, mmol l^{-1} (mean \pm s.d., range)	8.9 \pm 2.0, 5.1–12.4	5.4 \pm 0.4, 4.4–5.7
OGTT time, h (points)	5 (12)	
Sampling point, min	0, 10, 30, 60, 90, 120, 150, 180, 210, 240, 270, 300	
VPG, mmol l^{-1} (range)	2.9–31.8	
Data pairs, VPG and spectra	415	

the interference of the skin surface signal when capturing deeper glucose signals is imperative for clinically applicable noninvasive blood glucose monitoring.

In this work, we present multiple μ -spatially offset Raman spectroscopy (μ SORS), a technique capable of directly measuring Raman signals from both epidermal and dermal layers of human skin, and thus, potentially feasible for clinical noninvasive blood glucose monitoring. Utilizing an optical probe with fibre layout at five different offsets, μ SORS realized depth-selective detection of Raman signals, with larger offsets capturing a higher proportion of signals from greater depths. We first conducted a preliminary basic experimental study with humans (BESH) involving 35 participants that demonstrated that in contrast to the Raman signal from the skin surface, the μ SORS signal from deeper layers, especially around or below the dermal–epidermal junction (DEJ)²³, exhibits a statistically notable correlation of Raman glucose peaks to venous plasma glucose (VPG) levels. Based on this optimal detection depth, we then expanded the BESHs, monitoring the VPG of additional 230 participants while collecting Raman spectra from the optimal offsets using μ SORS. A partial least squares (PLS) regression model²⁴ was applied to predict the blood glucose level from the Raman spectra. Using independent training and test dataset consisting of data from different individuals (individual-independent), the model reached a mean absolute relative difference (MARD) of 14.6%, with 99.4% of the predictions in clinically acceptable zones of the consensus error grid (CEG; A + B)²⁵. This result indicates that μ SORS achieves a high accuracy in blood glucose measurement without personalized calibration and data acquisition, marking a valid demonstration of a clinically applicable technology for noninvasive blood glucose monitoring.

Results

μ SORS detects depth-selective Raman signals in skin layers

We tailored μ SORS for depth-selective detection of Raman signals from human skins. SORS is an advanced spectroscopic technology,

known for its ability to detect Raman signals beneath surfaces²⁶, and is widely applied in applications such as cargo content inspection²⁷, archaeology²⁸, cancer screening²⁹ and pharmaceutical analysis³⁰. Here, we reformed this technology at the scale of tens to hundreds of micrometres, aiming to obtain Raman signals from various depths of the skin to realize noninvasive blood glucose monitoring. An optical probe focused a 785-nm laser on the sample (human thenar in this work) and then collected the backscattered photons, directing them to a concentrically organized fibre bundle (Fig. 1a, top). The concentric layers of fibres were designed to capture photons emitted at specific lateral offsets, which were 0 μ m (offset 0), 50 μ m (offset 1), 100 μ m (offset 2), 150 μ m (offset 3) and 200 μ m (offset 4) from the incident beam centre, respectively (Fig. 1a, bottom right). The signal intensity is notably lower for larger offsets (Fig. 1a, bottom left). Nevertheless, the concentric layout led to more fibres at greater offsets, compensating for the decrease in signal intensity. We used a series of bilayer samples to assess the depth-selective detection capability of μ SORS^{26,31} (Extended Data Fig. 1a,b and Methods). Each offset exhibited a maximum intensity of the bottom layer at a different detection depth, indicating that Raman photons backscattered from larger offsets had a higher probability to have originated from greater depths (Extended Data Fig. 1c). Therefore, μ SORS technology proves capable of selectively collecting Raman signals at various depths on a sub-millimetre scale.

For the purpose of noninvasive glucose detection, the key is to acquire Raman signals dominated from the dermis, which is rich in interstitial fluid (ISF) and capillary loops and could provide direct evidence of blood glucose levels (Fig. 1b)³². The dermis lies under the DEJ, the depth of which can be identified from the optical coherence tomography (OCT) image (Extended Data Fig. 2). We first observed the biological variation in the histogram of DEJ depths from 232 samples (thenar from both hands of 116 individuals), which ranged from 250 to 700 μ m, with the most common depth around 350 μ m (Fig. 1c). We then selected four typical individuals with different DEJ depths (labelled I–IV, in the order of increasing DEJ depth; Fig. 1d and Extended Data Fig. 3) and measured their μ SORS spectra (Fig. 1e, offsets 0–4). Compared with the reference Raman spectra taken from ex vivo human epidermis and dermis samples (dashed lines in Fig. 1e, Extended Data Fig. 4 and Methods), the shape of spectra from offsets 0–4 exhibited a clear transition from epidermis-like to dermis-like for all four individuals, with corresponding shifts in the relative intensities of the Raman peaks assigned to collagen and nucleic acid (Fig. 1e). It is assumed that the distinct spectral features within the 1,200–1,400 cm^{-1} range, particularly evident in the relative intensities of the collagen Raman peak (1,240 cm^{-1}) and the nucleic acid Raman peak (1,320 cm^{-1})^{33–35}, mainly result from the compositional difference. This difference is shown in the skin tissue cross-section, where the epidermis consists of densely packed cells, whereas the dermis is rich in collagen (Extended Data Fig. 4 and Methods).

Combining the spectral transition and the DEJ depths derived from OCT, we can roughly characterize the detection depth of μ SORS in human thenar skin. The transition of μ SORS spectra from epidermis-like to dermis-like occurred at smaller offsets for samples with shallower DEJ depths and vice versa (Fig. 1e). Based on this trend,

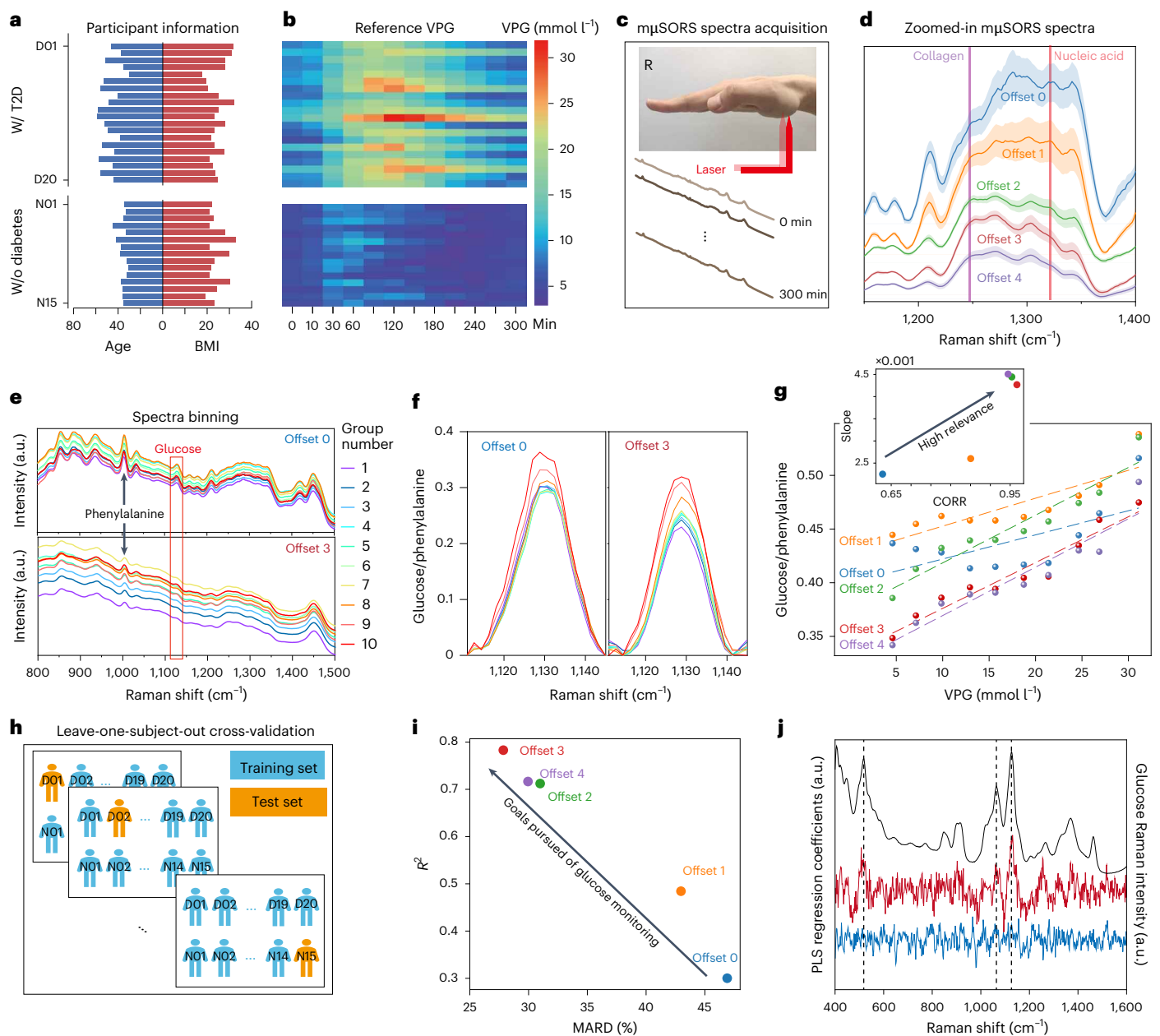


Fig. 2 | Correlation between μ SORS spectra and blood glucose levels in the preliminary BESH on 35 participants. **a**, Distribution of age and BMI of the 35 participants. **b**, VPG levels measured at 12 sampling points over the 5-h OGTT. **c**, Schematic of μ SORS spectra acquisition during OGTT. R, Right hand. **d**, Spectra averaged over all participants at each offset, zoomed in between 1,150 and 1,400 cm^{-1} . Solid lines indicate mean spectra. Shaded areas indicate s.d. Pink and purple shades show characteristic Raman peaks of nucleic acid and collagen. **e**, Mean μ SORS spectra from ten VPG bins with group number from 1 to 10. Offset 0 (top); offset 3 (bottom). **f**, Zoomed-in spectra around glucose

peak (red rectangle in **e**) after normalized by the phenylalanine band. Offset 0 (left). Offset 3 (right). **g**, Normalized glucose Raman band (**f**) against VPG levels for each offset. Dashed lines, linear fittings. Inset shows Pearson correlation coefficients and slopes of linear fittings. **h**, Schematic of the leave-one-subject-out cross-validation scheme for the PLS model. **i**, Metrics of model performance in **h** at different offsets. R^2 , coefficient of determination. **j**, Averaged regression coefficients obtained from **h** (light blue, offset 0; red, offset 3) and Raman spectrum of glucose solution (black). Black dashed lines indicate that the regression coefficients of offset 3 captured important spectral peaks of glucose.

we can use the DEJ depth determined by OCT as a 'ruler' to gauge the depth measured by a given offset of μ SORS. We thus roughly estimated the detection depths of five μ SORS offsets: 0–270 μm for offset 0, 270–370 μm for offset 1, 370–430 μm for offset 2, 430–620 μm for offset 3 and >620 μm for offset 4 (Table 1). In addition, μ SORS spectra at offsets 3 and 4 displayed dermis-like shapes or at least a mixture of epidermis-like and dermis-like features in all samples. Even offset 2 showed mixed features in Sample III, where the DEJ is deeper than 72% of all the 232 samples (Table 1). These results indicate that μ SORS also has a capability for depth-selective detection in human

skin, and it could effectively capture signals from the dermis for most individuals using offsets 2–4.

Dermal Raman spectra demonstrate high correlation with VPG
Having verified that μ SORS can selectively detect signals from various depths, including those deeper than the DEJ in human thenar skin, we proceeded to evaluate its capability for measuring glucose in the skin and predicting the blood glucose at a clinical setting. We conducted a preliminary BESH with 35 participants (Table 2 and Fig. 2a), in which we measured both μ SORS spectra from their right-hand thenar and their

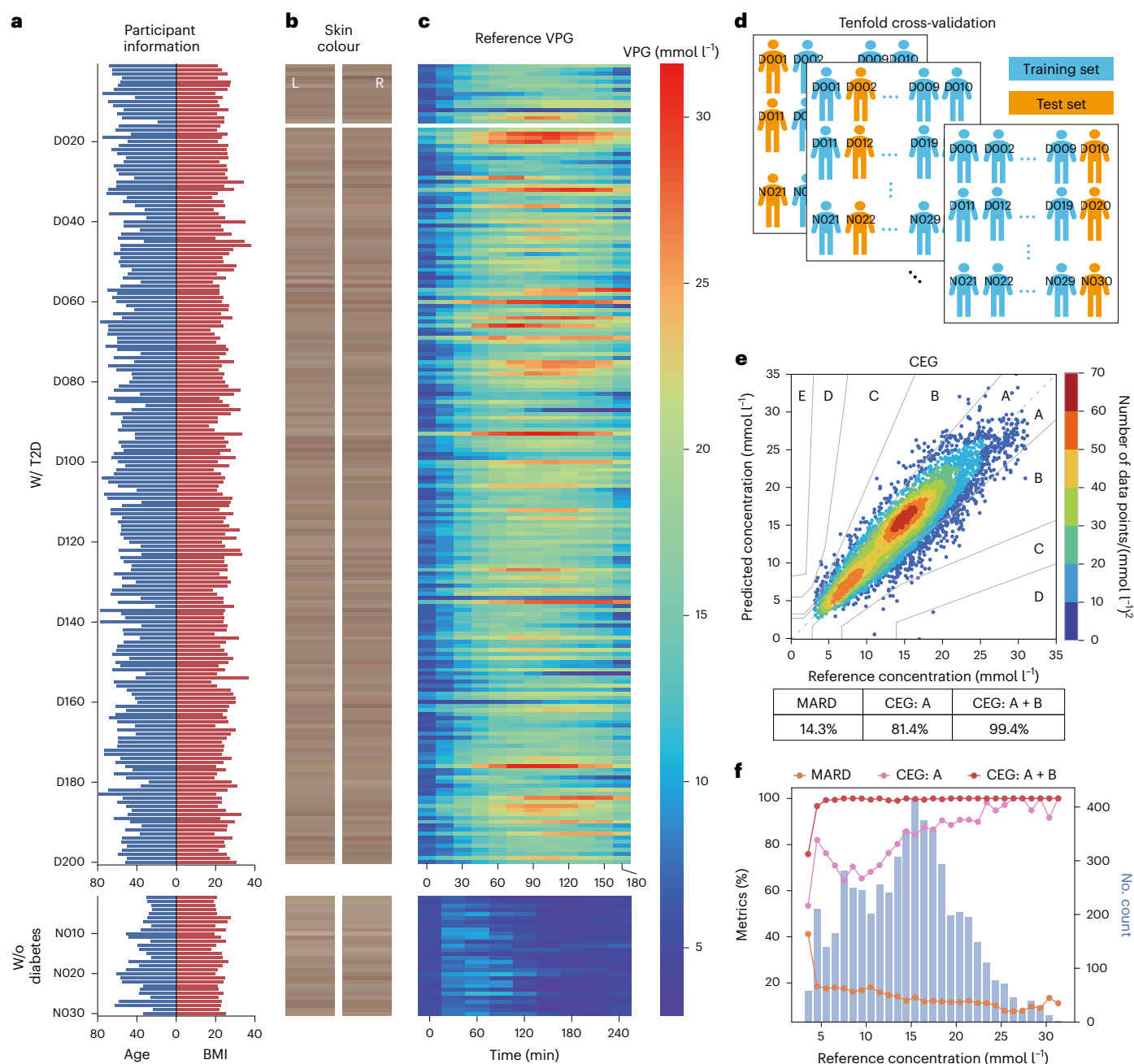


Fig. 3 | Blood glucose prediction of the 230 participants in expanded BESHs with subject-wise tenfold cross-validation. **a**, Distribution of age and BMI among the 230 participants. **b**, Thenar skin colours of the 230 participants. L and R indicate left and right hands, respectively. Missing data are marked in blank white. **c**, VPG levels of 230 participants measured during OGTT. **d**, Schematic of the subject-wise tenfold cross-validation scheme. Blue, training

set. Orange, test set. **e**, CEG of predictions from the PLS regression model in the cross-validation (**d**). Colours indicate the local density of data points. **f**, Model performance metrics plotted against reference glucose concentration. Orange, MARD. Magenta, percentage of data points in the A zone of the CEG (CEG A). Red, percentage of data points in the A or B zones of the CEG (CEG A + B). Blue shade, histogram of reference glucose concentrations (VPG).

VPG concentrations during a 5-h oral glucose tolerance test (OGTT) (Fig. 2b,c). Their VPG levels ranged from 2.9 to 31.8 mmol l⁻¹, covering the physiological to pathological blood glucose region (Table 2 and Fig. 2b). Individuals were free to take their hands off the setup or walk around in the sampling intervals (Fig. 2c). A total of 415 μSORS spectra sets (offsets 0–4) were acquired (Fig. 2d), each corresponding to VPG levels measured at the same time points, yielding 415 VPG–spectra data pairs. Consistent with before (Fig. 1e), the average spectra from the preliminary BESH exhibited a transition from epidermis-like to dermis-like with increasing offsets. Moreover, offsets 2–4 displayed highly similar spectral shapes and dermis-like spectral features between

1,150 and 1,400 cm⁻¹, indicating that all these three offsets are capable of detecting dermal signals (Fig. 2d).

To analyse Raman spectra across different glucose levels at different offsets, we categorized all the 415 VPG–spectra data pairs into ten groups based on the VPG level (equal binning; Fig. 2e and Supplementary Table 1). To account for variations in absolute spectrum intensity across groups, we normalized the glucose Raman band using the phenylalanine Raman band at 1,001 cm⁻¹, because phenylalanine is abundant in solid skin tissue compartments such as lipids, proteins and collagen. With a larger offset that can detect dermal signals, such as offset 3, the normalized glucose Raman peak increased notably

Table 3 | Statistics of the 230 participants in expanded BESHs

Statistics	Expanded BESHs (n=230)	
Participants (n)	With T2D (n=200)	Without diabetes (n=30)
Sex, male: female (%)	124 (62): 76 (38)	15 (50): 15 (50)
Age, years (mean±s.d., range)	55.1±11.4, 18–80	36.1±11.3, 22–59
BMI, kg m ⁻² (mean±s.d., range)	24.8±3.8, 16.2–38.1	22.5±2.5, 21.6–25.5
FPG, mmol l ⁻¹ (mean±s.d., range)	8.50±2.18, 4.82–17.84	5.15±0.32, 4.37–5.98
OGTT time, h (points)	3 (12)	4 (9)
Sampling, min	0, 15, 30, 45, 60, 75, 90, 105, 120, 135, 150, 180	0, 30, 60, 90, 120, 150, 180, 210, 240
VPG, mmol l ⁻¹ (range)	3.9–31.2	2.94–11.48
Data pairs, VPG and spectra	4,768	540
Statistics	Total data pairs (n=5,308)	

with VPG across the ten groups, exhibiting a trend not seen at offset 0 (Fig. 2f and Extended Data Fig. 5). Linear correlation analysis revealed a high correlation (with a Pearson correlation coefficient (CORR) of 0.94–0.97) between VPG and the normalized glucose Raman band at offsets 2–4, much higher than the correlation at offset 0 (CORR = 0.63) and offset 1 (CORR = 0.85) (Fig. 2g). The normalized glucose Raman band at offsets 2–4 also demonstrated notably greater sensitivity to VPG, as indicated by the steeper slopes in the linear fit (Fig. 2g, inset), suggesting that Raman spectra from dermal skin layers offer more relevant information about blood glucose levels. Both correlation and sensitivity to VPG are very similar for offsets 2–4 (Fig. 2g, inset), consistent with the highly similar shapes of average spectra observed at these three offsets (Fig. 2d).

To further determine the optimal offsets for individual-independent blood glucose monitoring, we built a PLS regression model to fit the VPG–spectra pairs from each offset individually, taking advantage of Raman features across the full spectral range. A leave-one-subject-out cross-validation scheme (Fig. 2h) was applied²⁴. The results indicated that offset 3 yielded the highest accuracy, closely followed by offset 4 and offset 2 (Fig. 2i). Notably, these offsets encompass the DEJ depths in the majority of individuals (Figs. 1c–e and 2d), supporting our hypothesis that signals from below the DEJ are more suitable for noninvasive blood glucose monitoring. In addition, our data analysis algorithm provided direct evidence of leveraging glucose-specific Raman spectral information. The PLS regression coefficients trained on spectra from offset 3 (Fig. 2j, red curve) aligned well with the characteristic Raman bands of glucose solution (Fig. 2j, black curve), a distinctive feature absent at offset 0 (Fig. 2j, blue curve). This alignment suggests that while analysing Raman signals from offset 3, we can leverage more directly relevant spectroscopic information of glucose molecules than other biomolecules in human skin. In contrast, at offset 0, neither glucose nor other biomolecular signals could be clearly identified.

Accurate and individual-independent glucose predictions

With the preliminary BESH, we identified direct evidence of glucose molecules in m μ SORS spectra, and determined that the optimal offsets to detect blood glucose Raman signals were offsets 2–4. However, due to the small sample size, the prediction accuracy remained low (MARD = 28.0% for offset 3) and failed to meet the clinical standards. To further improve the prediction accuracy, we initiated expanded BESHs of 230 individuals with two major improvements: (1) Raman spectra

were collected from the thenar of both hands to augment the dataset and eliminate hand-specificity; (2) spectra from offsets 2 and 3 were combined as the input to the PLS model according to the results of the preliminary BESH (Fig. 2i), whereas offset 4 was removed from the device due to its high spatial cost (requiring more fibres than other offsets; Fig. 1a) despite its high prediction accuracy. The 230 participants covered a wide range of age (18–80 years) and body mass indices (BMIs; 16.2–38.1 kg m⁻²) (Fig. 3a and Table 3). A relatively balanced representation of sex (91 female and 139 male; Table 3) and varied skin colours were also achieved (Fig. 3b). VPG levels of individuals ranged between 2.94 to 31.64, effectively covering the entire extent of physiological to pathological blood glucose levels (Fig. 3c and Table 3).

At each sampling point of the OGTT, we measured VPG and two m μ SORS spectra from the two hands of the participant, yielding a total of 5,308 VPG–spectra data pairs, -13 times larger than the dataset in the preliminary BESH. Each of these spectra was averaged over 60 frames (8 s per frame), providing a database with 318,480 single spectra in total. Spectra from offsets 2–3 and both hands were simultaneously used for model training and testing (with more details in Methods), generating separate predicted glucose concentrations for the left and right hands. Practically, this hand-independent approach allows users to freely choose either hand for blood glucose monitoring, thereby adding flexibility in the clinical use.

We employed a subject-wise tenfold cross-validation scheme (Fig. 3d)³⁶ to evaluate the prediction accuracy of m μ SORS for individual-independent blood glucose monitoring. Similar to the leave-one-subject-out scheme used in the preliminary BESH (Fig. 2), this approach simulated a scenario where a user's blood glucose levels can be directly measured and monitored without the need for personalized pre-calibration, validating the applicability of m μ SORS in real-life clinical settings and distinguishing it from various other works in the field¹⁹. Consequently, a total of 5,308 predicted glucose concentration values were generated, with each VPG value corresponding to two predicted concentration values, one from the left hand and the other from the right hand. Overall, 99.4% of these points fell within the clinically acceptable range (CEG A + B), achieving a MARD value of 14.3% (Fig. 3e). No significant difference in accuracy between female and male participants (13.43 ± 5.79% versus 14.98 ± 6.23%; $P = 0.06$, two-sample t -test) or between left and right hand (14.62 ± 6.65% versus 14.12 ± 7.16%; $P = 0.247$, paired sample t -test) was observed (Extended Data Figs. 6–8). For each participant, the predictions from the left-hand and right-hand spectra exhibited good consistency with each other, closely aligning with the VPG values and trends (Extended Data Figs. 6–8). Furthermore, the MARD value consistently remained below 20%, and the CEG A + B exceeded 99% across nearly all VPG intervals (Fig. 3f). In summary, m μ SORS provides real noninvasive blood glucose monitoring that is both accurate and flexible in clinical settings, without the need for personalized calibration.

Practical glucose monitoring on an independent test set

To mimic the conditions of clinical blood glucose monitoring even more closely and further validate the clinical applicability of m μ SORS, we performed model training and testing on two independent datasets. Overall, 30 participants (25 with type 2 diabetes (T2D) and 5 without diabetes) recruited at the end of each BESH were selected as an independent test set, while the rest 200 participants comprised the training set (Fig. 4a, Supplementary Table 2 and Extended Data Fig. 9). This generated 4,618 VPG–spectra data pairs in the training set and 690 in the test set, with diverse blood glucose trends and broad VPG distributions in both datasets. A PLS model was exclusively trained on the training set, after which the resulting regression coefficients were locked, and then used to predict the blood glucose level in the test set (Fig. 4a). A MARD value of 14.6% was achieved in the test set with 99.4% of predictions within the CEG A + B zone (Fig. 4b). Examining the prediction accuracy across different VPG concentrations, the

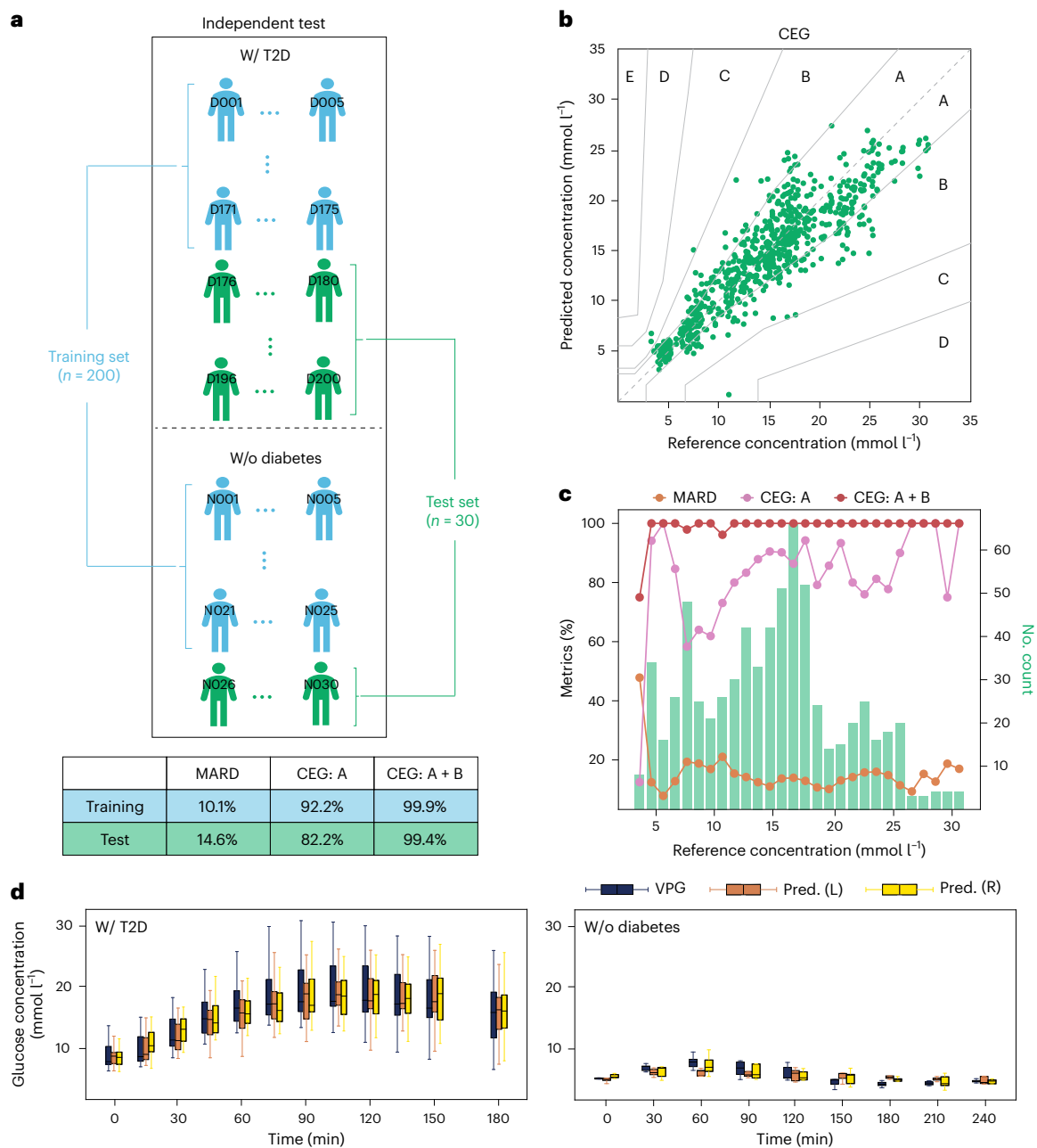


Fig. 4 | Blood glucose predictions on an independent test dataset. **a**, Schematic of model training ($n = 200$) and testing ($n = 30$) on independent datasets (top). Metrics of model performance on the training and test sets, respectively (bottom). **b**, CEG of predictions from the PLS regression model on the test set. **c**, Model performance metrics plotted against reference glucose concentration in the test set. Orange, MARD. Magenta, CEG A. Red, CEG A + B. Green shade, histogram of reference glucose concentration. **d**, Overall trends of predicted (orange, left hand; yellow, right hand) and reference glucose concentrations (dark blue) for participants with T2D (left, $n = 25$) and without diabetes (right, $n = 5$) in the test set during OGTT. In the box plot, box boundaries indicate Q1 (25th percentile) and Q3 (75th percentile), whiskers indicate Q1 $- 1.5 \times$ IQR and Q3 $+ 1.5 \times$ IQR and the centre indicates the median.

CEG A + B ratio consistently reached 100% in 25 out of 28 VPG intervals (1 mmol l^{-1} each), and the MARD value was lower than 20% in 26 out of 28 VPG intervals (Fig. 4c). These results in the independent test dataset again underscored the prominent capability of μSORS for noninvasive blood glucose monitoring.

For both hands, the predicted trends of blood glucose during OGTT closely matched the VPG trends, regardless of whether the individuals had diabetes (Fig. 4d). For participants with T2D, both VPG and predictions depicted monophasic OGTT response curves typical of T2D patients, in which the blood glucose level increases after the ingest of glucose and then decreases after reaching a peak³⁷. On the

other hand, the flat response curves observed in participants without diabetes reflected the capability of μSORS to generate accurate trend predictions even within the normal VPG range.

When it comes to every individual, the predicted glucose concentrations still demonstrated high accuracy and good alignment with the VPG, regardless of which hand the predictions came from (Fig. 5). This confirms the robustness of our system and offers users the flexibility to choose either hand for blood glucose measurements. In greater detail, participant D190 with the most accurate predictions in the test set showed a MARD value for both hands as small as 7.6%. Most participants showed typical prediction accuracy with MARD values

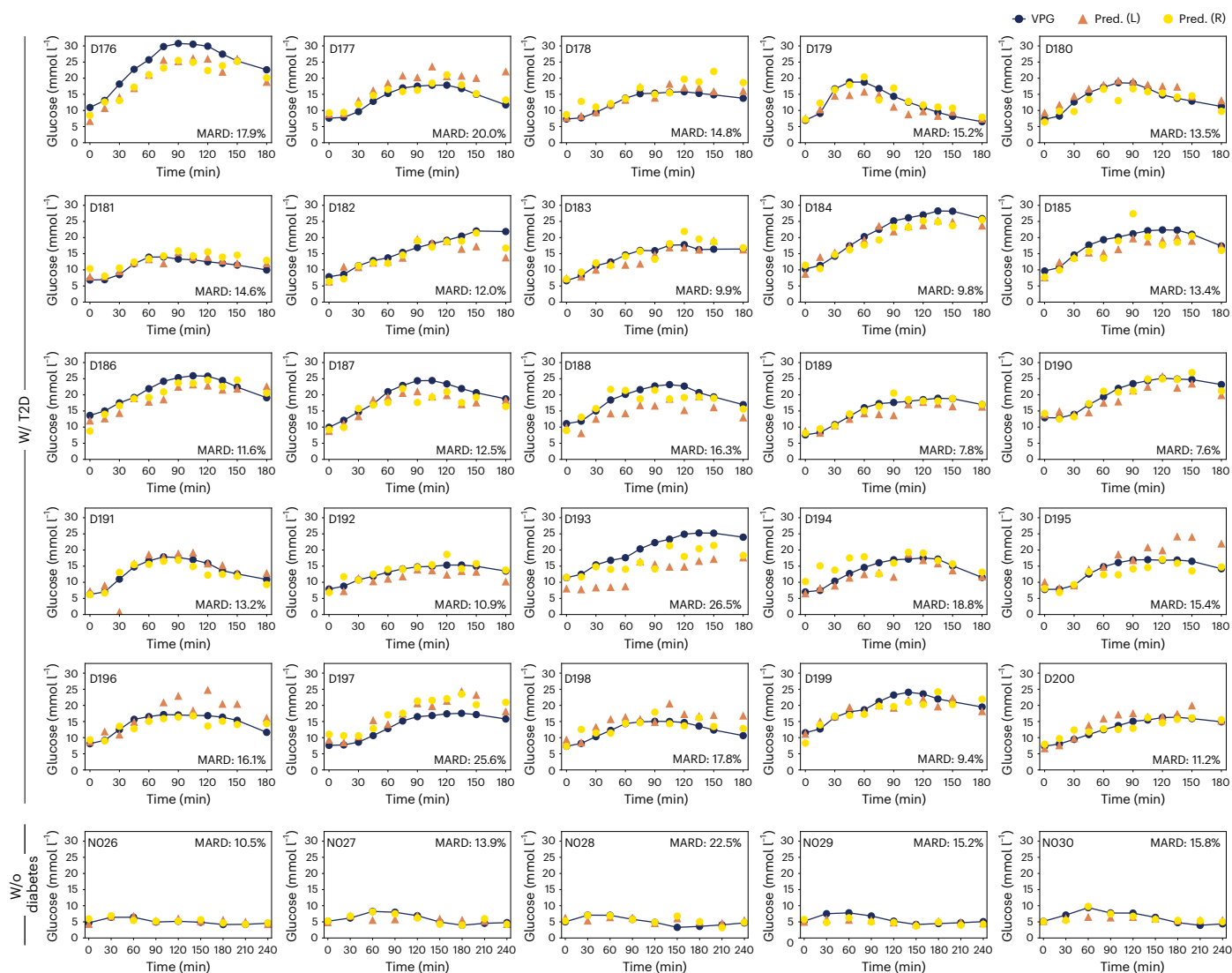


Fig. 5 Blood glucose prediction results for 30 participants in the test set with independent model testing. Dark blue shows reference glucose concentration during OGTT. Orange triangles show predictions from the left hand. Yellow circles show predictions from the right hand.

between 10% and 15%. Even for the participant with the highest MARD in the test set (D193, MARD = 26.5%), the predictions demonstrated a clear trend of increasing blood glucose concentration, consistent with the change of VPG, as well as a close proximity between predictions given by the two hands (Fig. 5). In summary, with the more rigorous validation provided by the independent test set, μ SORS once again proved itself of high accuracy and solid practical viability in clinical blood glucose monitoring.

Discussion

Depth-selectable sensing is critical to robust measurement of chemical levels in the blood. Based on the SORS technology^{22,38}, we developed the μ SORS system, in which the specially designed optical probe allows lateral offsets at the scale of tens of micrometres (Fig. 1a,b). Tested on a bilayer sample with tunable thickness of the surface layer, μ SORS achieved a depth resolution of 50–100 μ m (Extended Data Fig. 1c), which is a notable improvement from the millimetre resolution of the traditional SORS technology. Furthermore, combining the Raman spectral features and the DEJ depth estimated from the OCT data, we can conclude that the depth resolution of μ SORS in human skin is around 100–200 μ m (Fig. 1d,e and Table 1) and that for the majority of participants, the Raman signals from dermis layer can be captured

with offsets 2–4 (Table 1), which is well suited for noninvasive blood glucose sensing. In our preliminary BESH, a clear distinction emerged that Raman signals from the skin surface exhibited a much weaker correlation to VPG, whereas those from deeper depths corresponding to larger offsets displayed a precise linear correlation. In the expanded BESHs, utilizing spectra from offsets 2–3, our PLS model achieved high prediction accuracy for individual-independent and noninvasive blood glucose monitoring, with a MARD less than 15% and more than 99% predictions falling within the A + B zone of the CEG plot. Therefore, the critical and irreplaceable advantage of μ SORS in noninvasive blood glucose monitoring becomes evident. Meanwhile, it also offers a practical solution to systemic study on subsurface sensing.

Offsets 2–4 emerged as the most critical offsets with the highest relevance to the VPG concentration in the preliminary BESH (Fig. 2i). Combining OCT images and μ SORS spectra, we concluded that these offsets measured signals deeper than 370 μ m and up to over 620 μ m, beyond the DEJ in most participants (Fig. 1c and Table 1). This observation reaffirms our conclusion that DEJ is a critical depth for blood glucose monitoring, where both ISF and capillaries contribute to the detection of glucose Raman signals by μ SORS (Fig. 1b). Despite offset 4 having the deepest detection depth, its prediction accuracy was slightly lower than offset 3. This suggests that excessive detection

depths may actually reduce the accuracy of blood glucose measurement, likely due to the low signal-to-noise ratio caused by intensity decay in deeper layers. Therefore, considering the trade-off between human skin composition and the signal-to-noise ratio, the optimal depth for blood glucose monitoring could be just below the DEJ. Recent experiments of noninvasive blood glucose measurements in mice also targeted this depth, agreeing with our results that the signal from the DEJ is highly related to the VPG level¹⁵.

μ SORS-based blood glucose monitoring is characterized by its exceptional robustness, which provides great flexibility for the users. First, the depth-specificity of the signal and the high signal-to-noise ratio of the optical system enabled a completely noninvasive approach, effectively substituting traditional needles with laser technology. Second, users can freely move away from the device during sampling intervals. This design highlights an important advantage of our technology: it is highly robust to the reposition of hands which is usually considered as a difficult challenge in previous work. With this unique feature, there is no need to constantly attach the device on the patient, providing more convenience and comfort of using noninvasive glucose measurements. Most notably, μ SORS allows for individual-independent blood glucose monitoring. It eliminates the need for user-specific device calibration or model training, while still reaching clinically valuable MARD lower than 15%. Last but not least, a high accuracy was consistently achieved across the vast majority of VPG levels, covering nearly the entire physiological to pathological blood glucose range (Figs. 3f and 4c). It was also independent of the sex of the user and from which hand the spectra were measured. Therefore, μ SORS-based blood glucose monitoring can be applied to most random participants without any previous preparation and instantaneously acquire reliable predictions, a distinctive feature not achieved by many other recent technologies in the field^{18,19}.

Despite substantial technological advances and clinical applicability, μ SORS is still faced with several challenges. First, the prediction accuracy is still limited for a small percentage of participants. Second, μ SORS requires a relatively long acquisition time to reduce noise and distinguish Raman bands from the background signal. This potentially limits the model's accuracy to capture rapid glucose fluctuations, such as those during immediate correction of hypoglycaemia episodes caused by antidiabetic medication. Another important shortcoming is that μ SORS is still a large setup with a size comparable to a desktop computer. Moreover, thenar is the only measuring site so far due to its flat, large and soft surface, and we lack data for other possible areas of human skin. Finally, given that our BESHs were performed in China, additional local datasets are to be built when using μ SORS in other countries, considering potential physiological differences across ethnicities.

Future technological advances are expected to improve μ SORS from multiple aspects and address the challenges above. With the accumulation of more cases in further BESH or clinical studies, our PLS model could be refined to cover the physiological diversity of the population. More complicated algorithms, especially deep neural networks³⁹, are also expected to enhance the prediction accuracy of μ SORS and make it effective for a broader spectrum of users. The cause of the long acquisition time is that fluorescence from the tissue is still dominating, forming a strong optical background and also introducing considerable shot noise. Multiple newly developed technologies, such as time-gating technology, are promising to reduce the fluorescence background⁴⁰. Incorporating these technologies may reduce the time and laser power required for spectra collection, and even enable noninvasive monitoring of other chemicals in human bodies. Efforts are underway to transform this machine into a portable or even wearable device. This involves miniaturizing the Raman spectrometer to a chip level using spatial heterodyne spectroscopy that can be fabricated in a 200 mm CMOS compatible silicon

photonics platform⁴¹. Such chip technology may also reduce the cost of μ SORS, making it more affordable to the general public. Furthermore, packing μ SORS into a wearable device could extend its capability to measure various sites on human skin, some of which may have a thinner epidermis compared with the thenar region (for example, neck, abdomen, wrist or thigh)⁴². Glucose Raman spectra measured at these sites may attain higher signal-to-noise ratios due to shallower DEJ depths.

To sum up, we presented μ SORS technology, which is capable of measuring a depth-selective Raman signal, including glucose-related spectra from the dermis of human skin. This detection capability enables μ SORS to realize noninvasive blood glucose monitoring with high accuracy, without the need for personalized calibration.

Methods

μ SORS system design and setup

As shown in the overall schematic (Fig. 1a), a 65-mW laser was generated using a 785-nm diode multimode laser source (Cobolt 08-NLD) and directed through an optical probe to focus on the sample in a \sim 40- μ m spot. The scattered photons were collected using the same probe, filtered with a long-pass filter and then directed to a fibre bundle. The fibre bundle directed the signal to a near-infrared spectrometer (Blaze 400HR, LS785, Teledyne Princeton Instruments) equipped with an electrically cooled charge-coupled device.

To distinguish photons emitted with different offsets from the incident beam, at End A of the fibre bundle, the optical fibres were arranged in concentric ring structures (Fig. 1a). Each ring corresponded to a different offset between 0 μ m and 200 μ m at the surface of the sample, with a spacing of 50 μ m between adjacent offsets. This spacing step matches the distance between adjacent fibres of 125 μ m, after the 2.5-fold magnification by the lens (Fig. 1a). At End B of the fibre bundle, the fibres were arranged linearly and grouped according to their offsets before being directed to the spectrometer (Fig. 1a).

μ SORS system characterization with bilayer samples

0–15 Scotch tapes with 50- μ m thickness were layered on silicon substrate to create 16 bilayer samples, with the total tape thicknesses (top layer) ranging from 0 μ m to 750 μ m. We tested each sample three times at different locations with an acquisition time of 6 s. The Raman band area of Si was calculated with the integrals within the range of 500–540 cm^{-1} (Extended Data Fig. 1). For each offset, the areas of Si band from all 16 bilayer samples were normalized by their maximal value (Extended Data Fig. 1c).

Spectral calibration

After the acquisition of μ SORS spectra, a spectral calibration was performed using a neon–argon lamp (IntelliCal, Princeton Instrument). For each fibre, the pixels corresponding to ten standard neon–argon peaks were identified, and a four-order polynomial function was fitted between these identified pixels and the corresponding wavelengths for each fibre independently, thereby establishing the desired correspondence between spectrometer pixels and wavelengths. The wavelengths were then converted to the wavenumbers, which were later interpolated to the same abscissa for the spectra from all the fibres.

Human DEJ depth determination with OCT imaging

We performed OCT (Ganymede SD-OCT System, Thorlabs) on 232 thenars of both hands for $n = 116$ participants. For each hand, an area of 3 mm (x) \times 3 mm (y) was scanned up to a maximal depth (z) of 1.95 mm. The spatial resolution was 3.81 μ m in x and z dimensions and 12 μ m in the y dimension (Extended Data Fig. 2a). The refractive index of the target was set to 1.3. An intensity profile along the z dimension was calculated by averaging all the pixels along both x and y dimensions. The DEJ depth of the skin was manually annotated from the intensity profile using the characteristic points (Fig. 1d and Extended Data Fig. 2b).

Measurements on ex vivo human skin samples

After obtaining human skin tissue via punch biopsy, the sample was immediately fixed in 10% formaldehyde to preserve its architecture. It was then dehydrated through a gradient of alcohol, cleared with xylene and infiltrated with paraffin wax to form a solid block. The paraffin block was sliced into thin sections using a microtome and affixed to glass slides. These slides were subsequently analysed under bright-field microscopy using a WITec alpha 300 imaging system.

Ex vivo fresh human skin tissue from a participant was cut manually to prepare epidermal and dermal samples, which were diluted with phosphate-buffered saline (Hyclone), placed on a glass slide and sealed with a cover glass for Raman spectra measurements (WITec alpha 300) with a laser power of 75 mW and acquisition time of 120 s. Ex vivo human skin tissues used in this study have been sourced from the study approved by the Institutional Review Board of Ruijin Hospital (no. 2023-166) and Human Genetic Resource Administration of China. Both participants have provided written informed consent, which include a written description authorizing the use of his/her samples for other research.

Raman spectrum of glucose solution

The 1,000 mmol l⁻¹ glucose stock solution (Macklin, G885129) was loaded onto the probe with a pipette and its m μ SORS spectra were measured with an acquisition time of 8 s. The Raman spectra of glucose solution detected by offset 0 of m μ SORS system was used in this work (Fig. 2j).

Basic experimental study with humans

In the preliminary BESH, 20 participants with T2D and 15 participants without diabetes were selected. For the expanded BESHs, 200 participants with T2D and 30 participants without diabetes were included (Supplementary Table 2). The statistics of their age, sex (determined based on self-report and government-issued personal identity card) and fasting plasma glucose (FPG) levels are given in Tables 2 and 3. The study protocols were approved by the Institutional Review Board of Ruijin Hospital, affiliated with Shanghai Jiao Tong University School of Medicine, according to the Declaration of Helsinki. The studies are registered at ClinicalTrials.gov (NCT05504005, NCT05921344 and NCT06512077). All BESHs were open, and data collection and analysis were not performed blind to the conditions of the experiments. All the participants provided written informed consent and were compensated for their travel reimbursement and sampling.

The individuals were screened 1–7 days before the experiment. In the preliminary BESH, the recruiting criteria for participants without diabetes were that the FPG should be less than 6.1 mmol l⁻¹ and the glycosylated haemoglobin (HbA1c) should be less than 5.7%. For participants with T2D, their FPG levels were between 6.1–13.3 mmol l⁻¹. For the enrolment of T2D participants, it was required that no acute complications of diabetes within 3 months before enrolment, or severe chronic complications of diabetes and comorbidities (including severe structural heart disease, chronic congestive heart failure (NYHA \geq III) and history of severe liver or kidney dysfunction) were observed. All participants had no scars, pigmentation and other factors interfering with the test on the tested part of palm skin. Baseline physical examination, blood biochemistry test and a pregnancy test were conducted to confirm that no clinically notable abnormality was found for any of the participants.

All individuals had been fasted for at least 10 h before an OGTT with 75 g (50 g for individuals without diabetes in the expanded BESHs) glucose was given. Both m μ SORS spectra and the VPG concentration were taken for each participant at 12 (9 for individuals without diabetes in the expanded BESHs) sampling points, where individuals were allowed to move freely between sampling points. In the preliminary BESH, the 12 sampling points spanned across 5 h (0, 10, 30, 60, 90, 120, 150, 180, 210, 240, 270 and 300 min after glucose administration). In the expanded

BESHs, for individuals with T2D, the 12 sampling points spanned across 3 h (0, 15, 30, 45, 60, 75, 90, 105, 120, 135, 150 and 180 min after glucose administration); for individuals without diabetes, the 9 sampling points spanned across 4 h (0, 30, 60, 90, 120, 150, 180, 210 and 240 min after glucose administration) (Tables 2 and 3 and Supplementary Table 2). To measure the VPG concentration in both studies, 2 ml venous blood was taken and the plasma glucose concentration was measured by the biochemistry laboratory using the glucose oxidation method on an autoanalyser (AU5800, BECKMAN).

In the preliminary BESH, m μ SORS spectra (offsets 0–4) were taken from right hand with a total time of 8 min, a spectral range of 214 cm⁻¹ and 2,400 cm⁻¹, an integration time of 8 s and 60 frames averaged for each sampling point. Then, 415 valid VPG–m μ SORS spectra data pairs were acquired and used for data analysis (Fig. 2), while 5 pairs were discarded due to technical problems. In the expanded BESHs, different from before, m μ SORS spectra were taken from both hands simultaneously with two m μ SORS setups. A break was set at 4 min for participants to adjust their hand positions during the 8 min measurement. Overall, 5,308 VPG–m μ SORS spectra (offsets 0, 2 and 3, 0–2,450 cm⁻¹) data pairs were available for data analysis (Figs. 3 and 4), after excluding participant D016 who dropped out of the BESH and eight sampling points of participant D119's left hand due to technical problems. The skin colour of participants was measured using colorimeters (Colorimeter Max, CHN Spec) and saved as coordinates in the CIELAB colour space (Fig. 3b). No substantial improvement was found when skin colour was included in the PLS models.

Evaluation of the correlation between m μ SORS spectra and VPG

In the preliminary BESH, we divided the 415 VPG–spectra data pairs into ten groups based on equal binning of the VPG level (Supplementary Table 1). For each of the ten groups of spectra corresponding to different VPG, the average spectra for each offset were calculated (Fig. 2e and Extended Data Fig. 5). The glucose Raman band was defined as the area under the curve between 1,115 cm⁻¹ and 1,142 cm⁻¹ after removing the baseline (the straight line between the two end points) while that of phenylalanine was defined in the same way but between 990 cm⁻¹ and 1,020 cm⁻¹ (Extended Data Fig. 5)²¹. The ratio between these two was defined as the normalized glucose Raman band. The Pearson correlation coefficient (CORR) between the normalized glucose Raman band and the VPG was calculated to quantify the relevance of the spectra to the VPG (Fig. 2g). The slopes of linear fitting between the normalized glucose Raman band and the VPG were calculated to quantify the sensitivity of the spectra to the VPG (Fig. 2g, inset).

PLS cross-validation

We applied a PLS regression model⁴³ to predict the VPG concentrations from the Raman spectra in the BESHs. In the preliminary BESH, m μ SORS spectra between 400 cm⁻¹ and 1,600 cm⁻¹ from each offset were used as the input to the PLS model. Model cross-validation was conducted in the leave-one-subject-out procedure, where data from one participant was left to be predicted with the model trained on all the other data points, and this process was iterated to cover all participants once in the prediction (Fig. 2h). In the expanded BESHs, different from before, m μ SORS spectra between 320 cm⁻¹ and 2,000 cm⁻¹ from offsets 2 and 3 were concatenated into a single vector as the input to the PLS model. The model performance was evaluated using subject-wise tenfold cross-validation (Fig. 3d), where the dataset of all VPG–spectra pairs was partitioned into ten subsets ('tenfold') based on the last digit of the participant ID ('subject-wise'). In each iteration, one subset was selected as the validation set, while the remaining subsets were combined as the training set to train the PLS model. This process was iterated ten times, ensuring that every data point was included in the validation set once and only once (Fig. 3e,f). Considering that m μ SORS measures the spectra of the skin, where the glucose level is reported to have a time

lag (Δt) from the VPG^{44,45}, backtracked VPG concentrations were used as the reference for the PLS model (Extended Data Fig. 10).

PLS modelling and independent test

In the expanded BESHs, the PLS model was also tested with independent training and test sets (Fig. 4). Overall, 175 individuals with T2D (D001–D175) and 25 individuals without diabetes (N001–N025) were selected as the training set, while the rest (D176–D200 and N026–N030) were used as the test set (Fig. 4a). As before, μ SORS spectra between 320 cm^{-1} and 2,000 cm^{-1} from offsets 2 and 3 were concatenated into a single vector as the input to the PLS model. Backtracked VPG concentrations with a time lag (Δt) were used as the reference for the PLS model (Extended Data Fig. 10 and ‘Calculation of backtracked VPG concentration’). The optimal number of PLS factors was selected using the subject-wise tenfold cross-validation within the training set. This number of factors was then used to fit the model on the whole training set. Box plot was used to display the overall trend of predicted and reference glucose concentration (Fig. 4d). In the box plot, box boundaries indicate Q1 (25th percentile) and Q3 (75th percentile), whiskers indicate $Q1 - 1.5 \times \text{interquartile range (IQR)}$ and $Q3 + 1.5 \times \text{IQR}$, and the central line indicates the median.

Performance evaluation of PLS model for glucose prediction

The performance of a glucose prediction model was evaluated by the coefficient of determination (R^2), the MARD as well as the CEG-related metrics (CEG A and CEG A + B). A better model corresponds to a higher R^2 , a lower MARD and higher CEG A and CEG A + B.

The metrics of R^2 and MARD can be expressed as:

$$R^2 = 1 - \frac{\sum_{i=1}^N (y_i - \hat{y}_i)^2}{\sum_{i=1}^N (y_i - \bar{y})^2},$$

and

$$\text{MARD} = \frac{1}{N} \sum_{i=1}^N \left| \frac{\hat{y}_i - y_i}{y_i} \right|,$$

where N is the total number of VPG–spectra pairs in the test set, indexed by i , y_i and \hat{y}_i are the reference and the predicted glucose concentration of the i th VPG–spectra pair, respectively. \bar{y} is the mean of all the y_i .

Calculation of backtracked VPG concentrations

Backtracked VPGs were calculated with polynomial fit (order adjusted manually between 3 and 7) of the OGTT measurements for each participant. Assuming that the Δt was the same for all the individuals, we varied its value from 0 min to –25 min with a step size of 1 min to find the optimum, with which the minimal root mean square error (r.m.s.e.) between the backtracked VPGs and the predictions was achieved. The r.m.s.e. was defined as

$$\text{r.m.s.e.} = \sqrt{\frac{\sum_{i=1}^N (\hat{y}_i - y_i)^2}{N}},$$

where N denotes the number of data points (VPG–spectra pairs, indexed by i), y_i and \hat{y}_i are the backtracked and predicted VPG concentrations. Among all the offsets, the minimal r.m.s.e. was achieved by offset 3 with a time lag of –16 min in the preliminary BESH and –13 min in the expanded BESHs (Extended Data Fig. 10). Backtracked VPG concentrations were used in PLS model training and validation instead of the original measurements.

Reporting summary

Further information on research design is available in the Nature Portfolio Reporting Summary linked to this article.

Data availability

The data supporting the findings of this study are available from the corresponding authors upon reasonable request. Source data are provided with this paper.

Code availability

Custom Python code has been applied for data analysis in this work. The code necessary for reanalysing the data presented in this paper is available in Zenodo at <https://doi.org/10.5281/zenodo.14605629> (ref. 46).

References

1. IDF Diabetes Atlas 10th edition (International Diabetes Federation, accessed 22 January 2025); <https://diabetesatlas.org/atlas/tenth-edition/>
2. Brownlee, M. Biochemistry and molecular cell biology of diabetic complications. *Nature* **414**, 813–820 (2001).
3. Guy, R. H. A sweeter life for diabetics? *Nat. Med.* **1**, 1132–1133 (1995).
4. Heinemann, L. Finger pricking and pain: a never ending story. *J. Diabetes Sci. Technol.* **2**, 919–921 (2008).
5. Fruhstorfer, H. & Lange, H. Capillary blood sampling: how much pain is necessary? Part 3: pricking the finger can be less painful. *Pract. Diabetes. Int.* **12**, 253–254 (1995).
6. Lin, R., Brown, F., James, S., Jones, J. & Ekinci, E. Continuous glucose monitoring: a review of the evidence in type 1 and 2 diabetes mellitus. *Diabet. Med.* **38**, e14528 (2021).
7. Xie, X. et al. Reduction of measurement noise in a continuous glucose monitor by coating the sensor with a zwitterionic polymer. *Nat. Biomed. Eng.* **2**, 894–906 (2018).
8. Gao, W. et al. Fully integrated wearable sensor arrays for multiplexed in situ perspiration analysis. *Nature* **529**, 509–514 (2016).
9. Villena Gonzales, W., Mobashsher, A. & Abbosh, A. The progress of glucose monitoring—a review of invasive to minimally and non-invasive techniques, devices and sensors. *Sensors* **19**, 800 (2019).
10. So, C.-F., Choi, K.-S., Wong, T. K. & Chung, J. W. Recent advances in noninvasive glucose monitoring. *Med. Devices* **5**, 45–52 (2012).
11. Lin, T. et al. Non-invasive glucose monitoring: a review of challenges and recent advances. *Sensors* **20**, 6925 (2017).
12. Rao, G. et al. Reverse iontophoresis: noninvasive glucose monitoring in vivo in humans. *Pharm. Res.* **12**, 1869–1873 (1995).
13. Martín-Mateos, P. et al. In-vivo, non-invasive detection of hyperglycemic states in animal models using mm-wave spectroscopy. *Sci. Rep.* **6**, 34035 (2016).
14. Sim, J. Y., Ahn, C. G., Jeong, E. J. & Kim, B. K. In vivo microscopic photoacoustic spectroscopy for non-invasive glucose monitoring invulnerable to skin secretion products. *Sci. Rep.* **8**, 1059 (2018).
15. Uluç, N. et al. Non-invasive measurements of blood glucose levels by time-gating mid-infrared optoacoustic signals. *Nat. Metab.* **6**, 678–686 (2024).
16. Maruo, K. et al. In vivo noninvasive measurement of blood glucose by near-infrared diffuse-reflectance spectroscopy. *Appl. Spectrosc.* **57**, 1236–1244 (2003).
17. Enejder, A. M. K. et al. Raman spectroscopy for noninvasive glucose measurements. *J. Biomed. Opt.* **10**, 031114 (2005).
18. Pleus, S. et al. Proof of concept for a new Raman-based prototype for noninvasive glucose monitoring. *J. Diabetes Sci. Technol.* **15**, 11–18 (2020).
19. Pors, A. et al. Accurate post-calibration predictions for noninvasive glucose measurements in people using confocal Raman spectroscopy. *ACS Sens.* **8**, 1272–1279 (2023).
20. Zhang, L. et al. Spectral tracing of deuterium for imaging glucose metabolism. *Nat. Biomed. Eng.* **3**, 402–413 (2019).
21. Kang, J. W. et al. Direct observation of glucose fingerprint using in vivo Raman spectroscopy. *Sci. Adv.* **6**, 5206–5230 (2020).

22. Matousek, P. et al. Subsurface probing in diffusely scattering media using spatially offset Raman spectroscopy. *Appl. Spectrosc.* **59**, 393–400 (2005).
23. Aleemardani, M., Trikić, M. Z., Green, N. H. & Claeysens, F. The importance of mimicking dermal–epidermal junction for skin tissue engineering: a review. *Bioengineering* **8**, 148 (2021).
24. Wold, S., Sjöström, M. & Eriksson, L. PLS-regression: a basic tool of chemometrics. *Chemom. Intell. Lab. Syst.* **58**, 109–130 (2001).
25. Jendrike, N., Baumstark, A., Kamecke, U., Haug, C. & Freckmann, G. ISO 15197: 2013 evaluation of a blood glucose monitoring system's measurement accuracy. *J. Diabetes Sci. Technol.* **11**, 1275–1276 (2017).
26. Mosca, S., Conti, C., Stone, N. & Matousek, P. Spatially offset Raman spectroscopy. *Nat. Rev. Methods Primers* **1**, 21 (2021).
27. Eliasson, C., Macleod, N. A. & Matousek, P. Noninvasive detection of concealed liquid explosives using Raman spectroscopy. *Anal. Chem.* **79**, 8185–8189 (2007).
28. Conti, C. et al. Advances in Raman spectroscopy for the non-destructive subsurface analysis of artworks: Micro-SORS. *J. Cult. Herit.* **43**, 319–328 (2020).
29. Ghita, A., Matousek, P. & Stone, N. High sensitivity non-invasive detection of calcifications deep inside biological tissue using transmission Raman spectroscopy. *J. Biophotonics* **11**, jbio.201600260 (2018).
30. Matousek, P. & Parker, A. W. Bulk Raman analysis of pharmaceutical tablets. *Appl. Spectrosc.* **60**, 1353–1357 (2006).
31. Vardaki, M. Z. & Kourkoumelis, N. Tissue phantoms for biomedical applications in Raman spectroscopy: a review. *Biomed. Eng. Comput. Biol.* **11**, 1179597220948100 (2020).
32. Braverman, I. M. The cutaneous microcirculation. *J. Investig. Dermatol. Symp. Proc.* **5**, 3–9 (2000).
33. Liu, Z. et al. Circulation and long-term fate of functionalized, biocompatible single-walled carbon nanotubes in mice probed by Raman spectroscopy. *Proc. Natl Acad. Sci. USA* **105**, 1410–1415 (2008).
34. Darvin, M. E. et al. Confocal Raman microscopy combined with optical clearing for identification of inks in multicolored tattooed skin in vivo. *Analyst* **143**, 4990–4999 (2018).
35. Stone, N., Kendall, C., Shepherd, N., Crow, P. & Barr, H. Near-infrared Raman spectroscopy for the classification of epithelial pre-cancers and cancers. *J. Raman Spectrosc.* **33**, 564–573 (2002).
36. Hastie, T., Tibshirani, R., Friedman, J. H. & Friedman, J. H. *The Elements of Statistical Learning: Data Mining, Inference, and Prediction* (Springer, 2009).
37. Leonardo, D. A. M., Luciana, P. A., Fabricio, C. S. G. & Fernando, G. Distinct metabolic profile according to the shape of the oral glucose tolerance test curve is related to whole glucose excursion: a cross-sectional study. *BMC Endocr. Disord.* **18**, 56 (2018).
38. Di, Z. et al. Spatially offset Raman microspectroscopy of highly scattering tissue: theory and experiment. *J. Mod. Opt.* **62**, 97–101 (2015).
39. Luo, R., Popp, J. & Bocklitz, T. Deep learning for Raman spectroscopy: a review. *Analytica* **3**, 287–301 (2022).
40. Soleimaninejad, H., Matroodi, F. & Tavassoli, S. H. Raman spectroscopy of Iranian region calcite using pulsed laser: an approach of fluorescence suppression by time-gating method. *J. Spectrosc.* **2013**, 254964 (2013).
41. Van Dorpe, P. et al. High optical throughput, high spectral resolution, on-chip Raman spectrometer. In *Proc. 26th International Conference on Raman Spectroscopy (ICORS 2018)* 03-1079 (ICORS, 2018).
42. Lintzeri, D. A., Karimian, N., Blume-Peytavi, U. & Kottner, J. Epidermal thickness in healthy humans: a systematic review and meta-analysis. *J. Eur. Acad. Dermatol. Venereol.* **36**, 1191–1200 (2022).
43. Pankrushina, E. A., Kobuzov, A. S., Shchapova, Y. V. & Votyakov, S. L. Analysis of temperature-dependent Raman spectra of minerals: statistical approaches. *J. Raman Spectrosc.* **51**, 1549–1562 (2020).
44. Schmelzeisen-Redeker, G. et al. Time delay of CGM sensors: relevance, causes, and countermeasures. *J. Diabetes Sci. Technol.* **9**, 1006–1015 (2015).
45. Basu, A. et al. Time lag of glucose from intravascular to interstitial compartment in humans. *Diabetes* **62**, 4083–4087 (2013).
46. Shao, S. Subcutaneous depth-selective spectral imaging with μSORS enables non-invasive glucose monitoring. *Zenodo* <https://doi.org/10.5281/zenodo.14605629> (2025).
47. Zakharov, P., Dewarrat, F., Caduff, A. & Talary, M. S. The effect of blood content on the optical and dielectric skin properties. *Physiol. Meas.* **32**, 131–149 (2011).

Acknowledgements

We thank the field workers at Ruijin Hospital and the engineers at Shanghai Photonic View Technology Co., Ltd. for their contribution and the participants for their cooperation in the BESH. The funding by the Noncommunicable Chronic Diseases-National Science and Technology Major Project (2023ZD0508100, Y.Z.), Shanghai Shen-Kang projects (SHDC12024109, L. Zhang and SHDC22022301, W.W.), the Leader Project of the Oriental Talent Program in 2022 (no. 153, Y.Z.), Shanghai Pujiang Program (23PJ059, S.S.), Guangci Innovative Technology Program (KY2023810, C.C.), Guangci Talent Program (RC20240018, C.C.) and Guangci Deep Mind Project of Ruijin Hospital-Shanghai Jiao Tong University School of Medicine are gratefully acknowledged.

Author contributions

Y.Z., L. Zhou, G.N., C.C. and W. W. conceived the study and supervised the experiments. C.H., X.Z., M.S. and C.C. built the optical system. L.W., Y.Z., B.T. and J.S. took charge of the recruitment of subjects. L. Zhang, L.W., B.T., Y.C. and H.C. performed the experiments. M.C. collected the OCT data. S.S., Y.S., S.P., C.J., L. Zhou and C.C. performed data analysis. Y.Z., L. Zhang, L.W., S.S., L. Zhou and C.C. wrote the paper. G.N., C.C. and W.W. obtained the funding.

Competing interests

The μSORS technology presented in this paper is the subject of patents (CN115137298B, CN115120233B and CN214252020U) by Shanghai Photonic View Technology Co., Ltd. C.C. is a shareholder of Shanghai Photonic View Technology Co., Ltd. and the inventor of the patents. The other authors declare no competing interests.

Additional information

Extended data is available for this paper at <https://doi.org/10.1038/s42255-025-01217-w>.

Supplementary information The online version contains supplementary material available at <https://doi.org/10.1038/s42255-025-01217-w>.

Correspondence and requests for materials should be addressed to Lin Zhou, Guang Ning, Chang Chen or Weiqing Wang.

Peer review information *Nature Metabolism* thanks Andreas Birkenfeld, Ioan Notingher, Eric Renard and the other, anonymous, reviewer(s) for their contribution to the peer review of this work. Primary Handling Editor: Christoph Schmitt, in collaboration with the *Nature Metabolism* team.

Reprints and permissions information is available at www.nature.com/reprints.

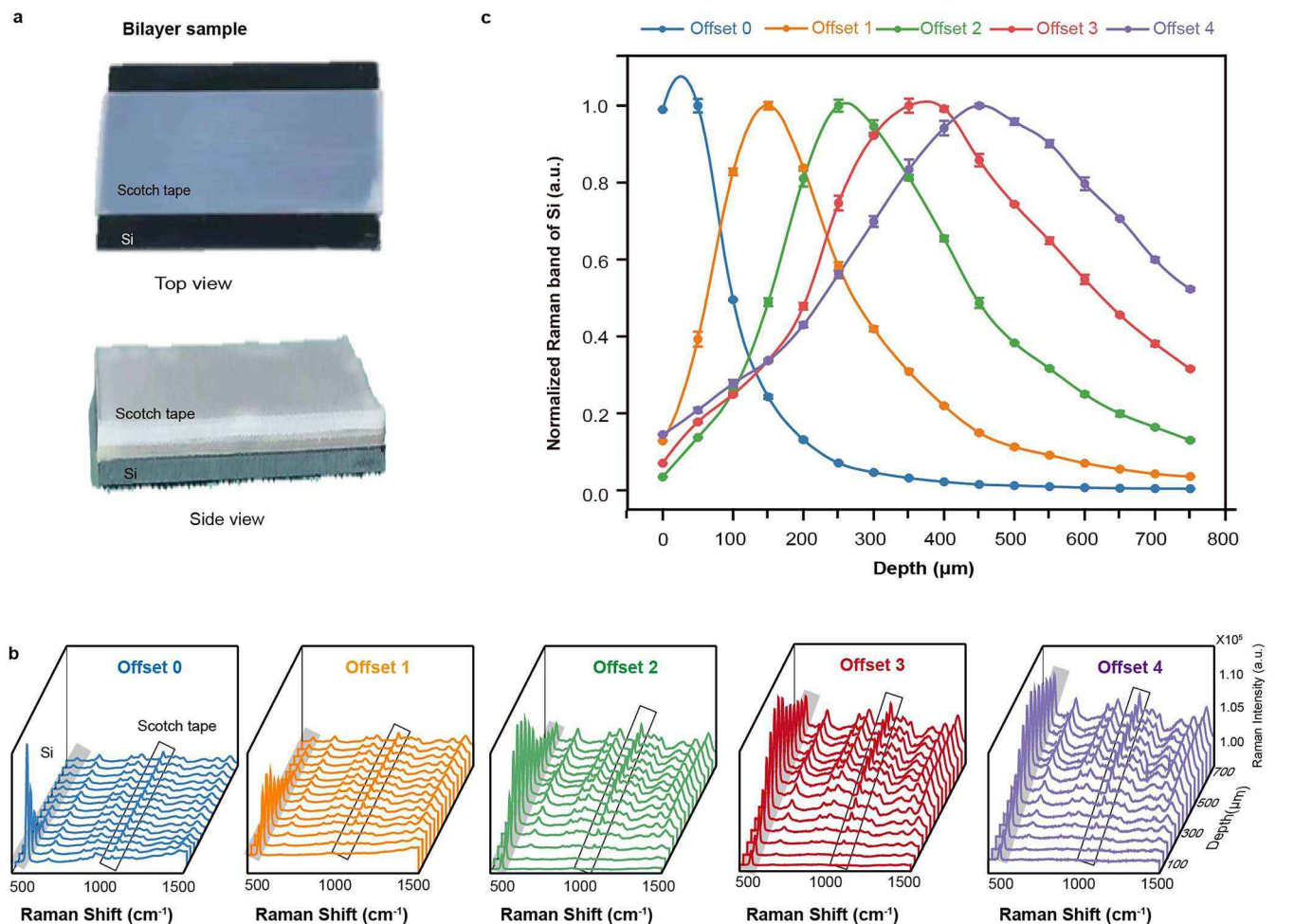
Publisher's note Springer Nature remains neutral with regard to jurisdictional claims in published maps and institutional affiliations.

Springer Nature or its licensor (e.g. a society or other partner) holds exclusive rights to this article under a publishing agreement with

the author(s) or other rightsholder(s); author self-archiving of the accepted manuscript version of this article is solely governed by the terms of such publishing agreement and applicable law.

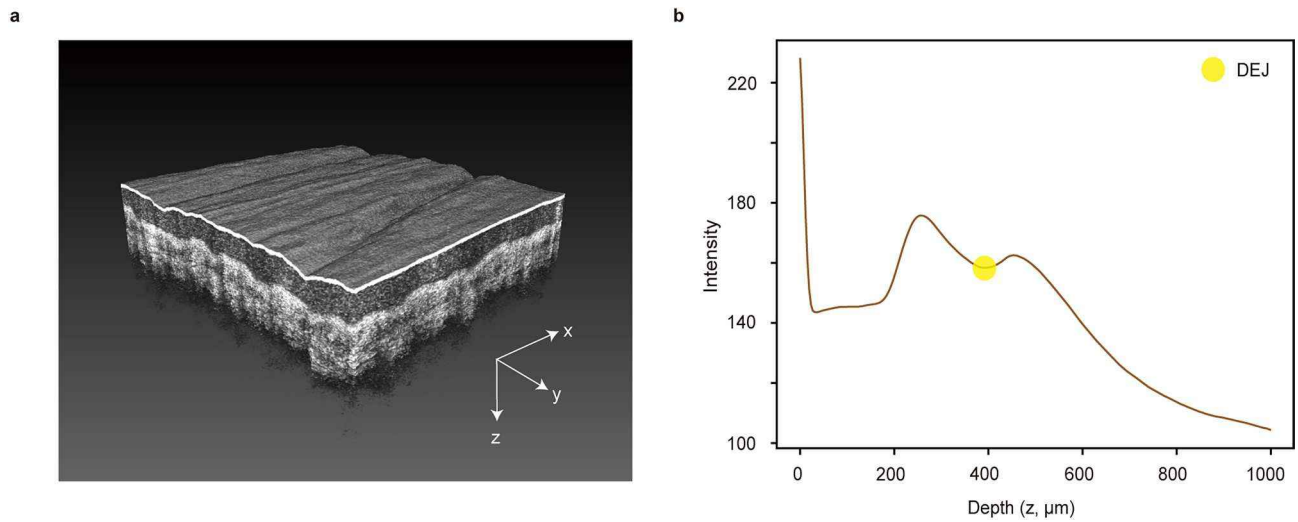
© The Author(s), under exclusive licence to Springer Nature Limited 2025

¹Department of Endocrine and Metabolic Diseases, Shanghai Institute of Endocrine and Metabolic Diseases, Ruijin Hospital, Shanghai Jiao Tong University School of Medicine, Shanghai, China. ²Shanghai National Clinical Research Center for Metabolic Diseases, Key Laboratory for Endocrine and Metabolic Diseases of the National Health Commission, Shanghai National Center for Translational Medicine, Ruijin Hospital, Shanghai Jiao Tong University School of Medicine, Shanghai, China. ³Shanghai Photonic View Technology Co., Ltd, Shanghai, China. ⁴Department of Dermatology, Ruijin Hospital, Shanghai Jiao Tong University School of Medicine, Shanghai, China. ⁵Shanghai Institute for Interventional Medical Devices, School of Health Science and Engineering, University of Shanghai for Science and Technology, Shanghai, China. ⁶State Key Laboratory of Transducer Technology, Shanghai Institute of Microsystem and Information Technology, Chinese Academy of Sciences, Shanghai, China. ⁷Institute of Medical Chip, Ruijin Hospital, Shanghai Jiao Tong University School of Medicine, Shanghai, China. ⁸These authors contributed equally: Yifei Zhang, Lili Zhang, Long Wang, Shuai Shao. ✉e-mail: lin.zhou@photonview.com; gning@sibs.ac.cn; changchen@sjtu.edu.cn; wqingw@shsmu.edu.cn

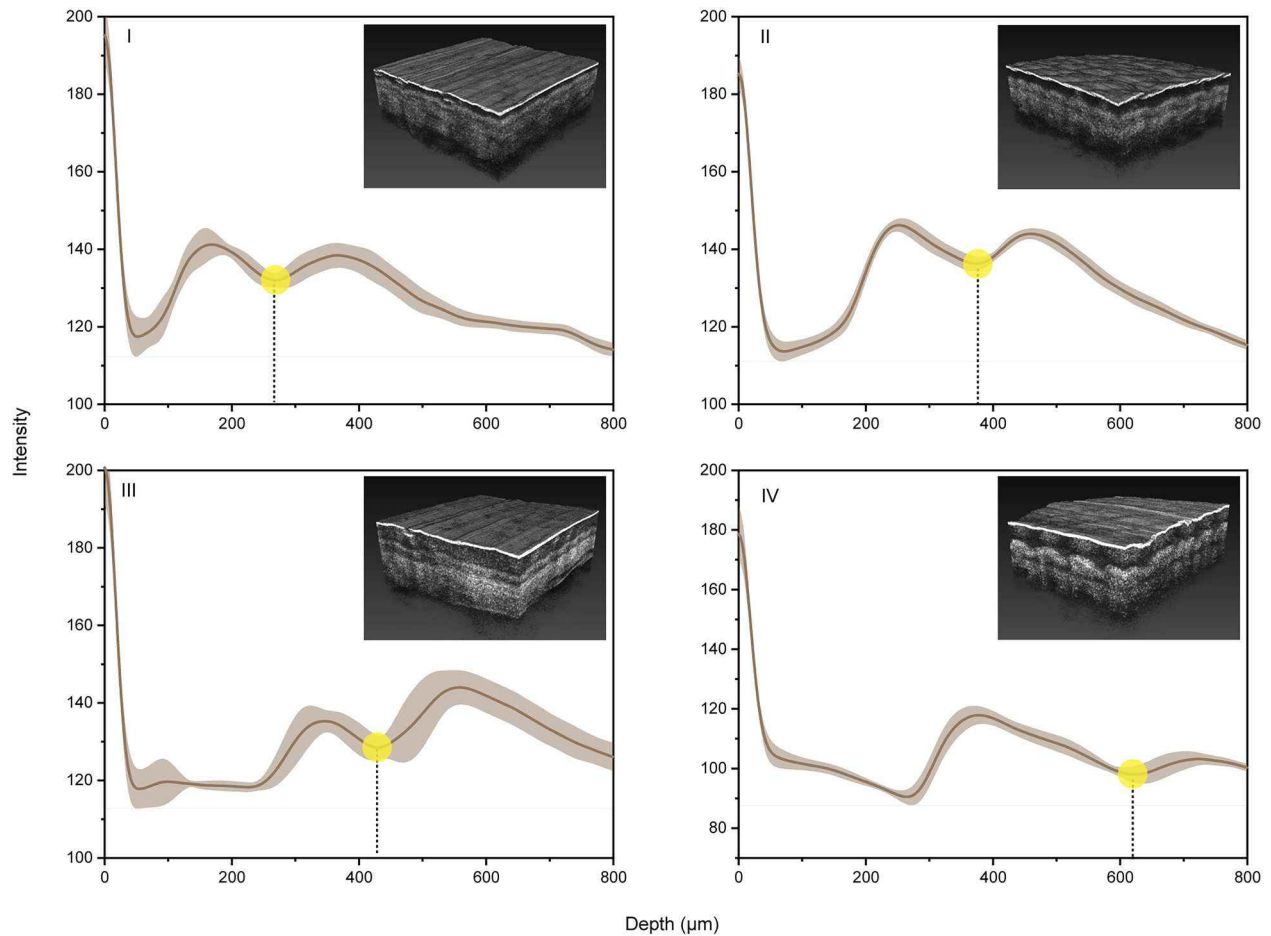


Extended Data Fig. 1 | Bilayer sample characterizes depth selectivity of $m\mu\text{SORS}$. **a**, Top view and side view of the Si-tape bilayer sample. **b**, Raman spectra of the bilayer sample displayed in three dimensions. Shade and box indicate characteristic Raman peaks at 520 cm^{-1} (Si) and 1041 cm^{-1} (Scotch tape), respectively. The depth of Si in 15 different phantoms increased from

$50\text{ }\mu\text{m}$ to $750\text{ }\mu\text{m}$ with a step of $50\text{ }\mu\text{m}$. **c**, Normalized Si (520 cm^{-1}) Raman band intensity varying with its depth for each offset. Error bars indicate mean and standard deviation (SD) over $n = 3$ measurements. Lines are derived from 9-order polynomial fitting of the measured points.

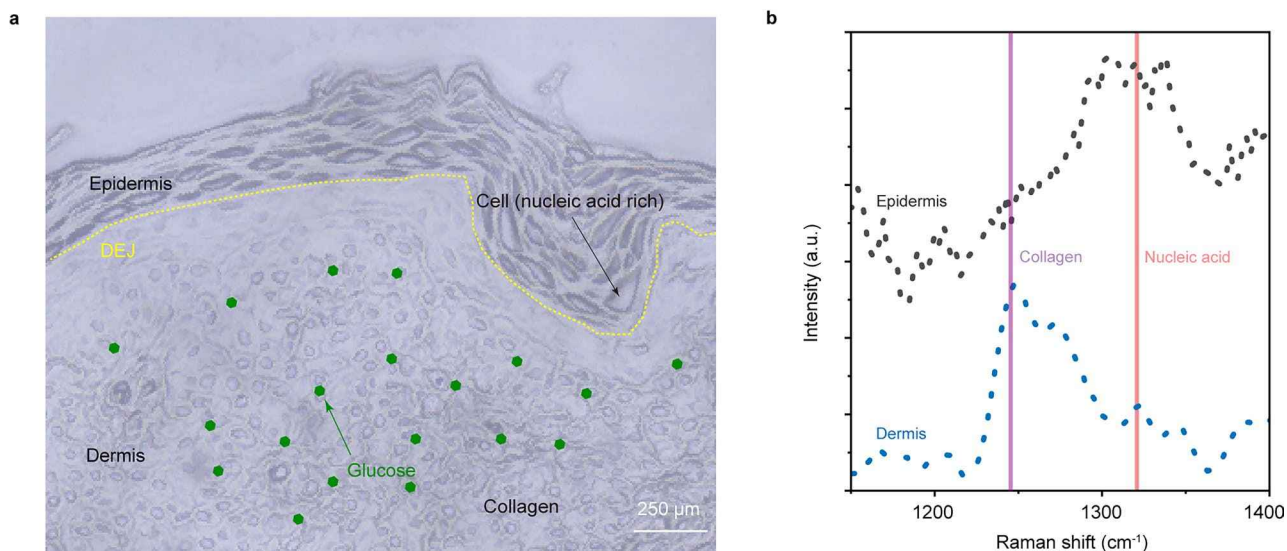


Extended Data Fig. 2 | Acquisition and analysis of OCT scans. a, The 3D image acquired by OCT (the left hand of D132 as an example). **b**, The intensity profile along the z (depth) dimension of Subject D132's left hand (same as a). $z = 0$ corresponds to the skin surface. Yellow dot indicates the characteristic points that were manually annotated and corresponded to the DEJ depth.



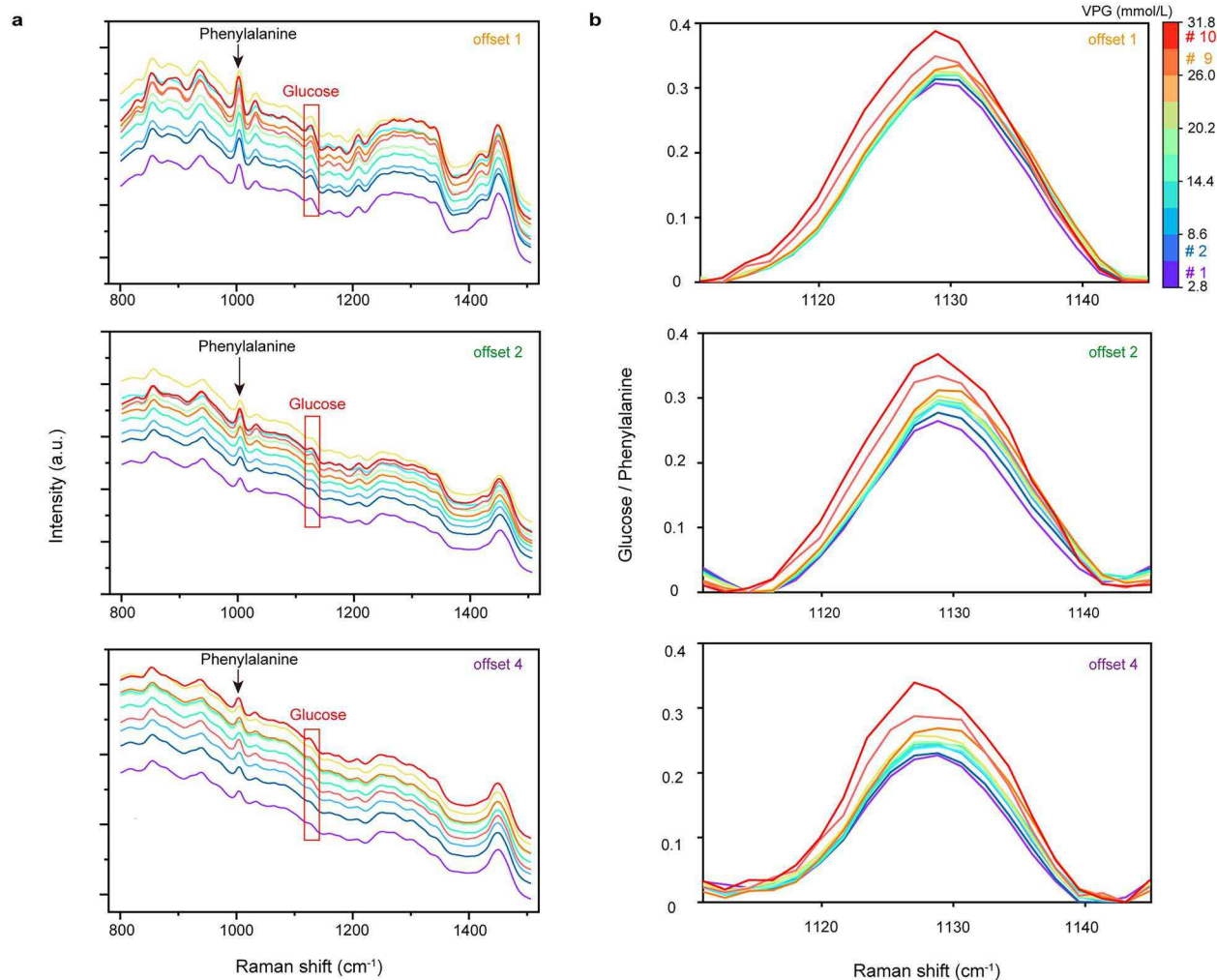
Extended Data Fig. 3 | Intensity profiles of four typical thenar OCT images. I–IV marked samples from a single hand of four typical subjects. The shades indicate the standard deviation (see **Methods**). Yellow dots indicate the characteristic

points that were manually annotated and corresponded to the DEJ depth. Insets: three-dimensional OCT images constructed from a volume of 3 mm (x) * 3 mm (y) * 1.95 mm (z).



Extended Data Fig. 4 | Anatomical and spectral characterization of epidermis and dermis of human skin samples. **a**, Bright field image of a processed *ex-vivo* human skin cross-section. A forearm cross-section from one woman of 29 years old were imaged and repeated independently five times with similar results, the zoom-in region of interest was shown. Epidermis is rich in cells, and thus, nucleic acid, while dermis is rich in collagen. The yellow dashed curve indicates the DEJ. Green dots indicate the distribution of glucose molecules, predominantly within

the dermis. Scale bar: 250 μm . **b**, Reference Raman spectra taken from *ex-vivo* epidermis (black) and dermis (blue) samples of human skin. An *ex-vivo* fresh upper back tissue from one man of 28 years old was obtained and cut manually to prepare epidermal and dermal samples, five spectra were collected from different region of interest for each sample and the mean spectra were shown as reference spectra. Pink and purple shades indicate characteristic Raman peaks of nucleic acid and collagen.



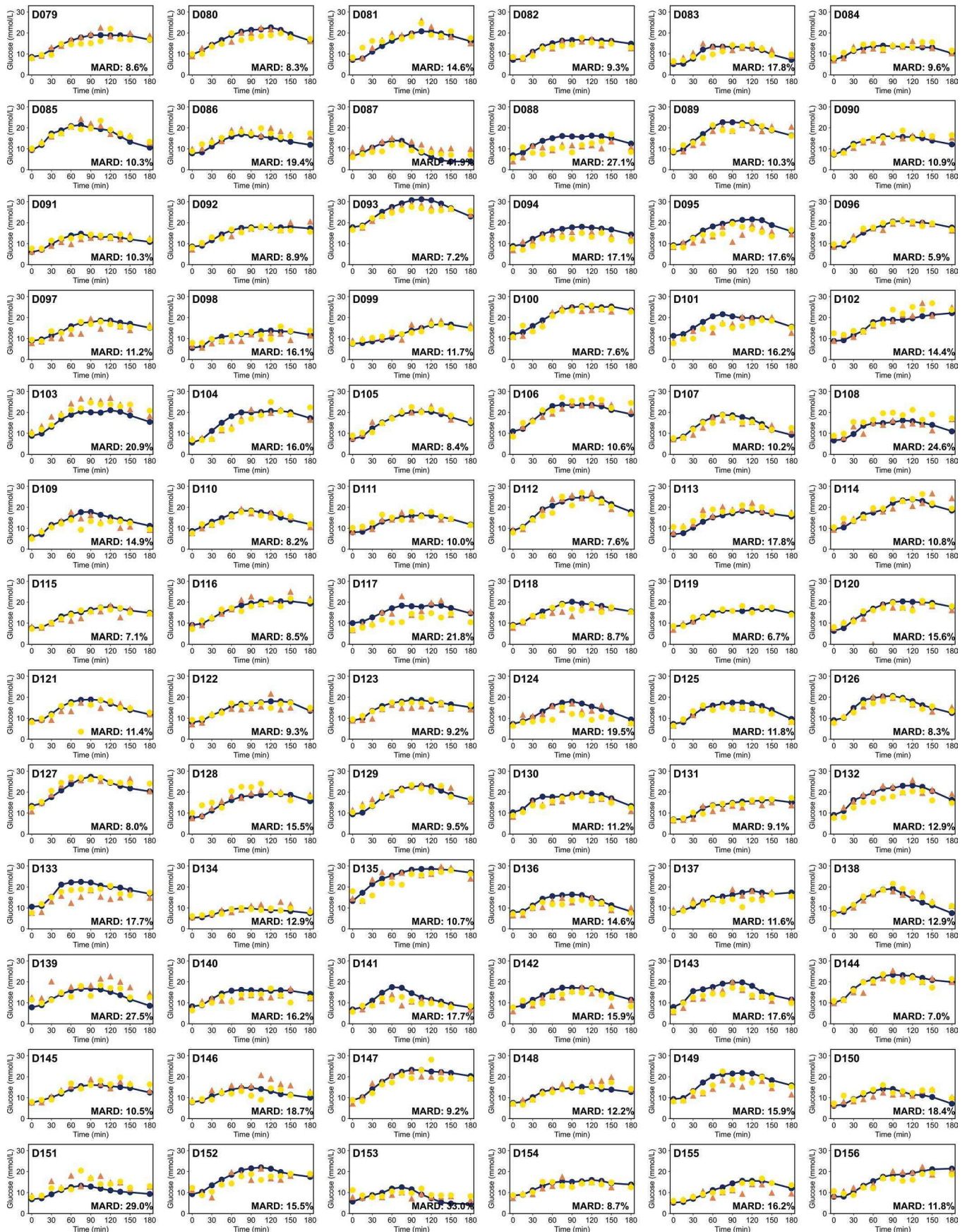
Extended Data Fig. 5 | μ SORS spectra of 10 groups partitioned by equal binning of VPG levels. a, Average spectra in the range of 800–1,500 cm^{-1} for each of the 10 VPG-spectra groups (Fig. 2e) at different offsets in the preliminary BESH of 35 subjects. The black arrow indicates the phenylalanine Raman peak

at 1001 cm^{-1} , while the red box indicates the characteristic glucose Raman peak at 1,125 cm^{-1} . **b**, Normalized Raman spectra (glucose Raman band divided by phenylalanine Raman band) of different offsets averaged over each of the 10 VPG-spectra groups (Fig. 2f), zoomed in around the glucose Raman peak at 1125 cm^{-1} .



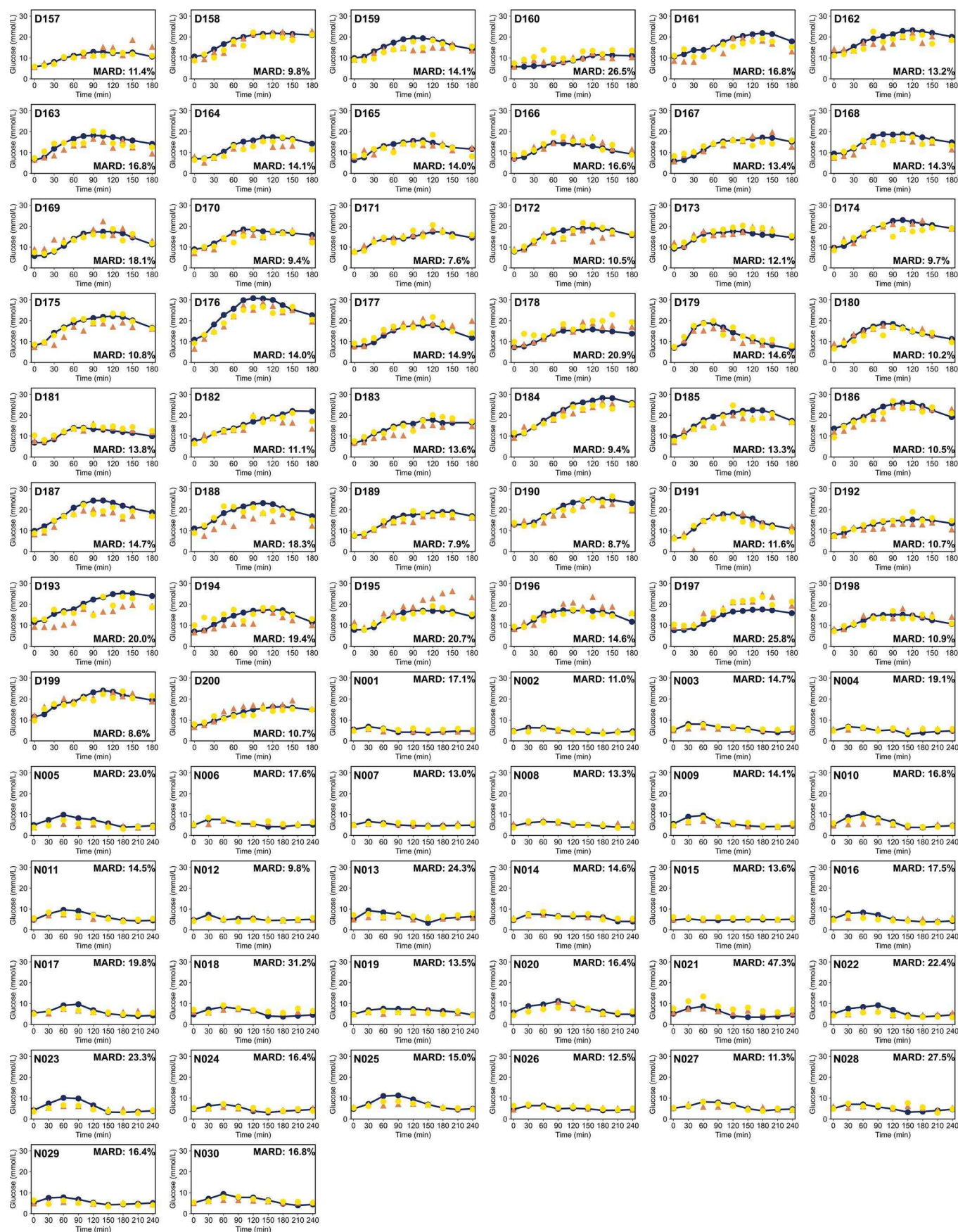
Extended Data Fig. 6 | Blood glucose prediction results for 78 subjects with type 2 diabetes (D001-D078) in all 230 subjects of expanded BESHs. Dark Blue lines: reference concentration (VPG, Fig. 3c). Orange triangles: glucose

concentration predicted from left-hand spectra. Yellow circles: glucose concentration predicted from the right-hand spectra. All predictions were generated using subject-wise tenfold cross-validation (Fig. 3d).



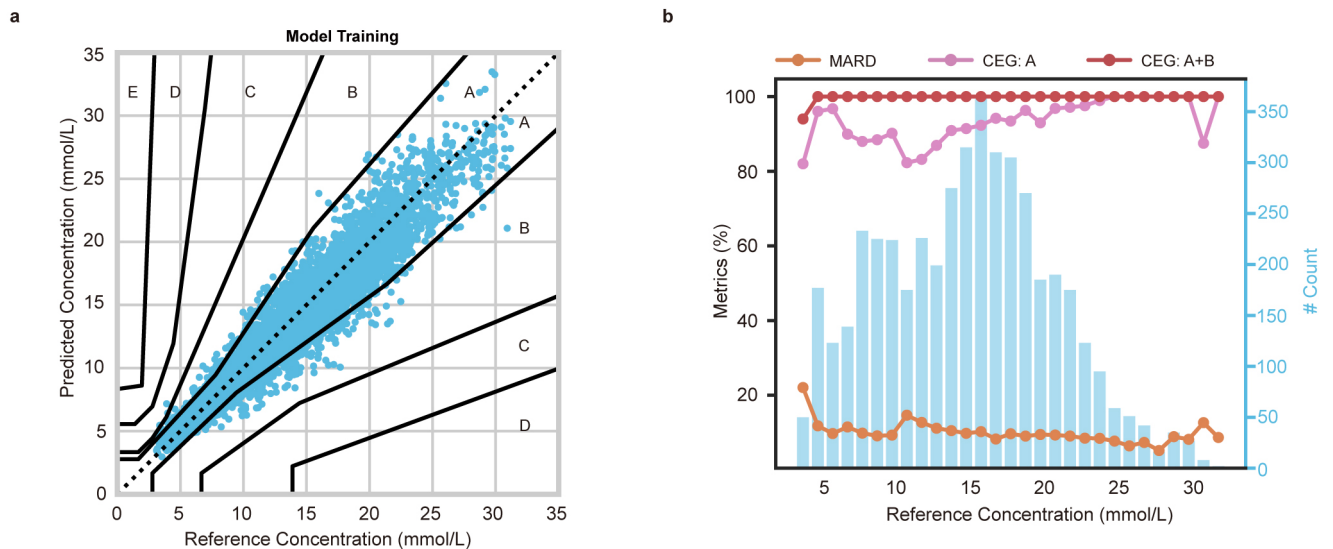
Extended Data Fig. 7 | Blood glucose prediction results for 78 subjects with type 2 diabetes (D079-D156) in all 230 subjects of expanded BESHs. Dark Blue lines: reference concentration (VPG, Fig. 3c). Orange triangles: glucose

concentration predicted from left-hand spectra. Yellow circles: glucose concentration predicted from the right-hand spectra. All predictions were generated using subject-wise tenfold cross-validation (Fig. 3d).



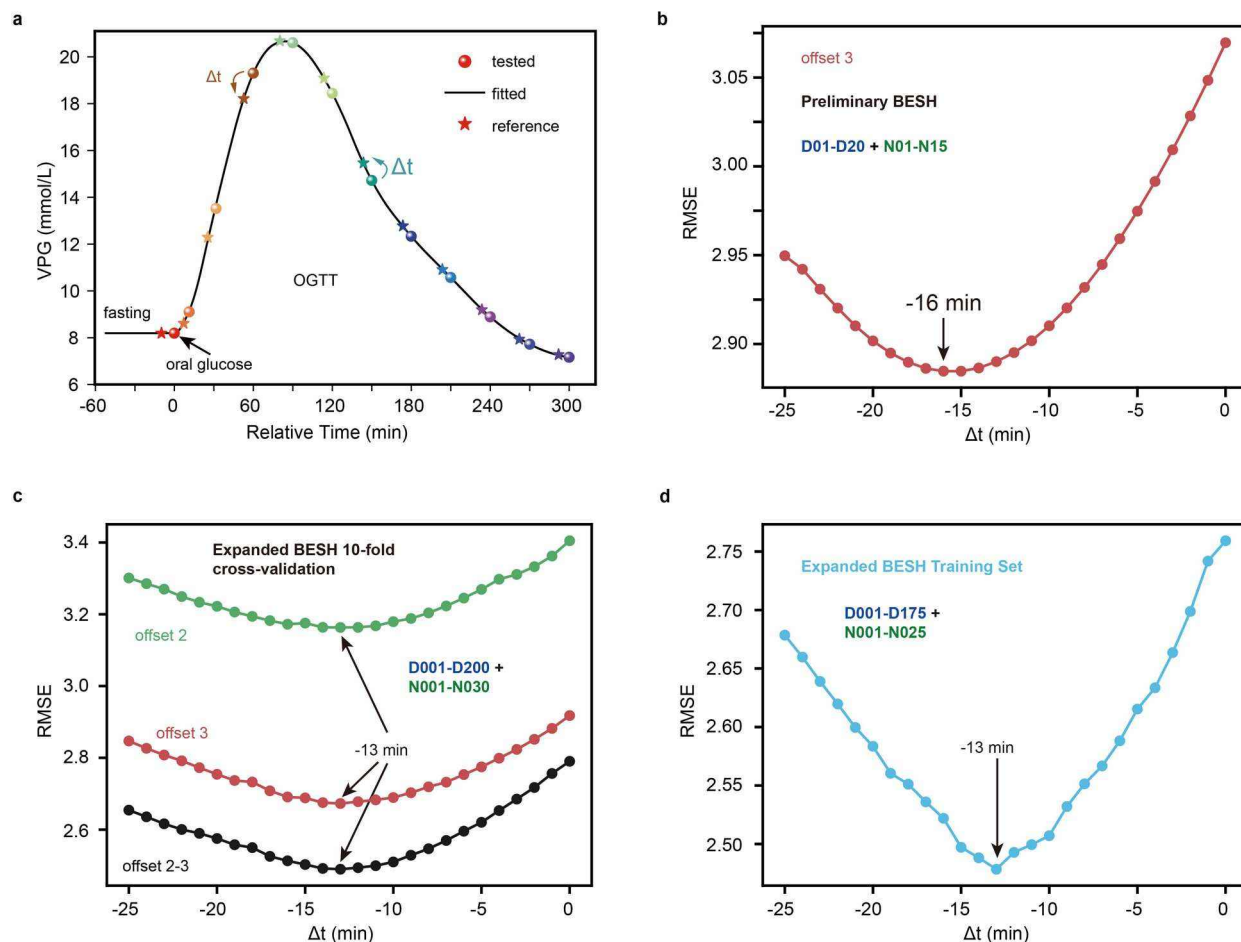
Extended Data Fig. 8 | Blood glucose prediction results for 48 subjects with type 2 diabetes (D157–D200) and 30 subjects without diabetes (N001–N030) in all 230 subjects of expanded BESHs. Dark Blue lines: reference concentration (VPG, Fig. 3c). Orange triangles: glucose concentration predicted from left-hand

spectra. Yellow circles: glucose concentration predicted from the right-hand spectra. All predictions were generated using subject-wise tenfold cross-validation (Fig. 3d).



Extended Data Fig. 9 | PLS model training for independent test. a. Consensus error grid (CEG) of the predictions obtained from the PLS regression model on the training set (n = 4,618). **b.** Model performance metrics plotted

against reference glucose concentration in the training set. Orange: MARD. Magenta: CEG: A. Red: CEG: A + B. Cyan shade: histogram of reference glucose concentration (VPG).



Extended Data Fig. 10 | Optimizing the time delay in the PLS model for glucose prediction. **a**, The VPG data of a typical subject with diabetes during the 5-h OGTT in the preliminary BESH. Measured VPGs (dots) were fitted with polynomials and the backtracked VPG with a certain time lag (stars) were used as reference in PLS models. **b**, RMSE between the model predictions and the reference VPGs, varying with the time lag from -25 to 0 min. The optimized time lag was at -16 min. The models were trained and tested with spectra from offset 3 in the preliminary BESH. Model predictions were generated using leave-one-

subject-out cross-validation scheme (Fig. 2h). **c**, Counterpart of **b** for offset 2 and 3 as well as the concatenation (offset 2–3) of these two offsets in the expanded BESHs of 230 subjects. The optimal time lag was at -13 min for both two offsets and the concatenation. Model predictions were generated using subject-wise tenfold cross-validation scheme (Fig. 3d). **d**, Counterpart of the black curve in **c** in the training set comprised of 200 subjects in the expanded BESHs (Fig. 4a). The optimal time lag was at -13 min.

Reporting Summary

Nature Portfolio wishes to improve the reproducibility of the work that we publish. This form provides structure for consistency and transparency in reporting. For further information on Nature Portfolio policies, see our [Editorial Policies](#) and the [Editorial Policy Checklist](#).

Statistics

For all statistical analyses, confirm that the following items are present in the figure legend, table legend, main text, or Methods section.

- | | |
|-------------------------------------|--|
| n/a | Confirmed |
| <input type="checkbox"/> | <input checked="" type="checkbox"/> The exact sample size (n) for each experimental group/condition, given as a discrete number and unit of measurement |
| <input type="checkbox"/> | <input checked="" type="checkbox"/> A statement on whether measurements were taken from distinct samples or whether the same sample was measured repeatedly |
| <input type="checkbox"/> | <input checked="" type="checkbox"/> The statistical test(s) used AND whether they are one- or two-sided
<i>Only common tests should be described solely by name; describe more complex techniques in the Methods section.</i> |
| <input checked="" type="checkbox"/> | <input type="checkbox"/> A description of all covariates tested |
| <input checked="" type="checkbox"/> | <input type="checkbox"/> A description of any assumptions or corrections, such as tests of normality and adjustment for multiple comparisons |
| <input type="checkbox"/> | <input checked="" type="checkbox"/> A full description of the statistical parameters including central tendency (e.g. means) or other basic estimates (e.g. regression coefficient) AND variation (e.g. standard deviation) or associated estimates of uncertainty (e.g. confidence intervals) |
| <input type="checkbox"/> | <input checked="" type="checkbox"/> For null hypothesis testing, the test statistic (e.g. F , t , r) with confidence intervals, effect sizes, degrees of freedom and P value noted
<i>Give P values as exact values whenever suitable.</i> |
| <input checked="" type="checkbox"/> | <input type="checkbox"/> For Bayesian analysis, information on the choice of priors and Markov chain Monte Carlo settings |
| <input checked="" type="checkbox"/> | <input type="checkbox"/> For hierarchical and complex designs, identification of the appropriate level for tests and full reporting of outcomes |
| <input type="checkbox"/> | <input checked="" type="checkbox"/> Estimates of effect sizes (e.g. Cohen's d , Pearson's r), indicating how they were calculated |

Our web collection on [statistics for biologists](#) contains articles on many of the points above.

Software and code

Policy information about [availability of computer code](#)

Data collection

Raman spectra are acquired by μ SORS system developed in this study.
Venous blood glucose (VBG) is measured by an autoanalyzer (AU5800, BECKMAN).
DEJ Depth of human thenar was determined by optical coherence tomography system (Ganymede SD-OCT System, Thorlabs).
Bright field image and Raman spectra of ex-vivo human skin were obtained from WITec alpha 300 imaging system (Germany).

Data analysis

Python version 3.9.13 is used with the base packages and the following additional packages: numpy (1.21.5), matplotlib (3.5.2), scipy (1.9.1), pandas (1.4.4), and seaborn (0.11.2). A standard PLS algorithm is used to build the regression models. The analysis codes used in the current study are available upon reasonable request addressed to the corresponding authors

For manuscripts utilizing custom algorithms or software that are central to the research but not yet described in published literature, software must be made available to editors and reviewers. We strongly encourage code deposition in a community repository (e.g. GitHub). See the Nature Portfolio [guidelines for submitting code & software](#) for further information.

Data

Policy information about [availability of data](#)

All manuscripts must include a [data availability statement](#). This statement should provide the following information, where applicable:

- Accession codes, unique identifiers, or web links for publicly available datasets
- A description of any restrictions on data availability
- For clinical datasets or third party data, please ensure that the statement adheres to our [policy](#)

Data and code showed in figures can be found with the link: <https://doi.org/10.6084/m9.figshare.25750602>. All data used in the current study are available upon reasonable request addressed to the corresponding authors

Research involving human participants, their data, or biological material

Policy information about studies with [human participants or human data](#). See also policy information about [sex, gender \(identity/presentation\), and sexual orientation](#) and [race, ethnicity and racism](#).

Reporting on sex and gender

In all basic experimental studies with humans (BESHs), the sex of the participants was reported as a number and percentage of the total number of participants. Sex or birth gender of participants was determined based on self-report and government-issued personal Identity Card (ID). We performed sex-based analyses and showed no significant difference in accuracy between female and male subjects.

Reporting on race, ethnicity, or other socially relevant groupings

All participants in the study were Chinese.

Population characteristics

In the preliminary BESH (No. NCT05504005): 1) Male or female, healthy or previously diagnosed type 2 diabetes. 2) Aged between 30 and 60 years. 3) For healthy subjects without diabetes history, fasting blood glucose (FPG) < 6.1 mmol/L and glycated hemoglobin (HbA1c) < 5.7% during the screening period and for patients with type 2 diabetes, FBG \geq 6.1 and < 13.3 mmol/L. 4) There are no scars, obvious pigmentation and other factors that interfere with the detection of the palm skin to be tested.

In the expanded BESH (No. NCT05921344): 1) Male or female, previously diagnosed type 2 diabetes. 2) Aged larger than or equal to 18 years old. 3) There are no scars, obvious pigmentation and other factors that interfere with the detection of the palm skin to be tested.

In the expanded BESH (No. NCT06512077): 1) Male or female, without diabetes history. 2) Aged larger than or equal to 18 years old. 3) Fasting blood glucose (FPG) < 6.1 mmol/L and glycated hemoglobin (HbA1c) < 5.7% during the screening period. 4) There are no scars, obvious pigmentation and other factors that interfere with the detection of the palm skin to be tested.

Recruitment

All BESHs were open, participants were recruited from Ruijin hospital. For the enrollment of T2D subjects, it is required that no acute complications of diabetes within 3 months before enrollment, or severe chronic complications of diabetes and comorbidities (including severe structural heart disease, chronic congestive heart failure (NYHA \geq III), and history of severe liver or kidney dysfunction, etc) were observed.

Ethics oversight

All ethics approvals were obtained from the RuiJin Hospital Ethics Committee, affiliated with Shanghai JiaoTong University School of Medicine. All the subjects have provided written informed consent and were compensated for the travel reimbursement and sampling.

Note that full information on the approval of the study protocol must also be provided in the manuscript.

Field-specific reporting

Please select the one below that is the best fit for your research. If you are not sure, read the appropriate sections before making your selection.

Life sciences Behavioural & social sciences Ecological, evolutionary & environmental sciences

For a reference copy of the document with all sections, see [nature.com/documents/nr-reporting-summary-flat.pdf](https://www.nature.com/documents/nr-reporting-summary-flat.pdf)

Life sciences study design

All studies must disclose on these points even when the disclosure is negative.

Sample size

35 participants in the preliminary BESH (No. NCT05504005).
200 participants in the expanded BESH (No. NCT05921344).
30 participants in the expanded BESH (No. NCT06512077).
No sample-size calculations were performed. Sample sizes were chosen based on similar previously published studies of non-invasive glucose blood monitoring (Stefan Pleus et al. J Diabetes Sci Technol. 15,11-18 (2020) & Anders Pors et al. ACS Sens. 2024 <https://doi.org/10.1021/acssensors.2c02756>). The numbers of samples are large enough to capture normal variation and glucose feature from Raman spectra according to the published data in this field.

Data exclusions

In the preliminary BESH (No. NCT05504005): Among all 420 sets of data, 5 spectra are lost due to technical issues.

Data exclusions	In the expanded BESH (No.NCT05921344): Among all 4800 sets of data, 24 from both hands of subject D016 were lost because the subject quit the BESH. 8 sampling points of subject D119 were lost due to technical problems. In the expanded BESH (No.NCT06512077): Among all 540 sets of data, no data lost.
Replication	We have demonstrated the replication with three independent BESHs.
Randomization	N/A - No randomization was used in this study, and all enrolled subjects were treated the same.
Blinding	N/A - Blinding was not necessary since there was no randomization nor experimental groups.

Reporting for specific materials, systems and methods

We require information from authors about some types of materials, experimental systems and methods used in many studies. Here, indicate whether each material, system or method listed is relevant to your study. If you are not sure if a list item applies to your research, read the appropriate section before selecting a response.

Materials & experimental systems

n/a	Involved in the study
<input checked="" type="checkbox"/>	<input type="checkbox"/> Antibodies
<input checked="" type="checkbox"/>	<input type="checkbox"/> Eukaryotic cell lines
<input checked="" type="checkbox"/>	<input type="checkbox"/> Palaeontology and archaeology
<input checked="" type="checkbox"/>	<input type="checkbox"/> Animals and other organisms
<input type="checkbox"/>	<input checked="" type="checkbox"/> Clinical data
<input checked="" type="checkbox"/>	<input type="checkbox"/> Dual use research of concern
<input checked="" type="checkbox"/>	<input type="checkbox"/> Plants

Methods

n/a	Involved in the study
<input checked="" type="checkbox"/>	<input type="checkbox"/> ChIP-seq
<input checked="" type="checkbox"/>	<input type="checkbox"/> Flow cytometry
<input checked="" type="checkbox"/>	<input type="checkbox"/> MRI-based neuroimaging

Clinical data

Policy information about [clinical studies](#)

All manuscripts should comply with the ICMJE [guidelines for publication of clinical research](#) and a completed [CONSORT checklist](#) must be included with all submissions.

Clinical trial registration	https://clinicaltrials.gov/ , No. NCT05504005, No. NCT05921344 and No.NCT06512077.
Study protocol	https://clinicaltrials.gov/
Data collection	We recruited all the participants, performed the study and collected all the data in Ruijin Hospital affiliated with Shanghai JiaoTong University School of Medicine in Shanghai of China. The data in preliminary BESH (No. NCT05504005) was collected from August to December in 2022. The data in expanded BESH (No. NCT05921344) was collected from July to September in 2023. The data in expanded BESH (No.NCT06512077) was collected in August of 2024.
Outcomes	Primary outcome: 1) Mean absolute relative deviation (MARD) of venous plasma glucose and glucose values measured by μ SORS at each time point of OGTT. 2) Consensus Error Grid (CEG) for venous plasma glucose and glucose values measured by μ SORS at each time point of OGTT. Secondary Outcome: 1) MARD for two measurement methods in different blood glucose ranges. 2) Incidence of treatment-emergent adverse events.

Plants

Seed stocks	N/A.
Novel plant genotypes	N/A.
Authentication	N/A.

Subcutaneous depth-selective spectral imaging with μ SORS enables noninvasive glucose monitoring

Received: 7 May 2024

Accepted: 8 January 2025

Published online: 05 February 2025

 Check for updates

Yifei Zhang^{1,2,8}, Lili Zhang^{3,8}, Long Wang^{1,2,8}, Shuai Shao^{3,8}, Bei Tao^{1,2}, Chunrui Hu³, Yufei Chen^{1,2}, Yue Shen³, Xianbiao Zhang³, Shijia Pan^{1,2}, Hua Cao⁴, Ming Sun³, Jia Shi^{1,2}, Chunhong Jiang^{1,2}, Minghui Chen⁵, Lin Zhou³✉, Guang Ning^{1,2}✉, Chang Chen^{3,6,7}✉ & Weiqing Wang^{1,2}✉

Noninvasive blood glucose monitoring offers substantial advantages for patients, but current technologies are often not sufficiently accurate for clinical applications or require personalized calibration. Here we report multiple μ -spatially offset Raman spectroscopy, which captures Raman signals at varying skin depths, and show that it accurately detects blood glucose levels in humans. In 35 individuals with or without type 2 diabetes, we first determine the optimal depth for glucose detection to be at or below the capillary-rich dermal–epidermal junction, where we observe a strong correlation between specific Raman bands and venous plasma glucose concentrations. In a second study, comprising 230 participants, we then improve accuracy of our regression model to reach a mean absolute relative difference of 14.6%, without personalized calibration, whereby 99.4% of calculated glucose values fall into clinically acceptable zones of the consensus error grid (zones A and B). These findings highlight the ability and robustness of multiple μ -spatially offset Raman spectroscopy for noninvasive blood glucose measurement in a clinical setting.

Blood glucose monitoring is critical for health management, especially for the over 500 million people with diabetes worldwide^{1,2}. Patients with diabetes typically receive recommendations to monitor their blood glucose level multiple times per day³. Nevertheless, conventional finger pricks induce pain and risk of infection, which thereby reduced the patients' quality of life and their adherence to treatment^{4,5}. More recently, minimally invasive continuous blood glucose monitoring technologies have been developed, utilizing indwelling sensors to measure glucose levels in interstitial compartments^{6,7}. However, these sensors require constant attachment to the user and cause inconvenience⁸. Hence, there remains a persistent need for practical solutions to noninvasive blood glucose monitoring⁹.

So far, the route to clinically applicable noninvasive blood glucose monitoring remains elusive^{10,11}. Among the various approaches,

including iontophoresis¹², transdermal impedance spectroscopy¹³, photoacoustic spectroscopy^{14,15} and infrared spectroscopy^{16,17}, Raman spectroscopy is highly anticipated due to its direct identification of glucose molecules with high specificity by spectral information^{18–22}, along with its selectable wavelengths for deep penetration in human skin. Recently developed paraboloidal mirror Raman¹⁸, confocal Raman¹⁹ and spatially offset Raman spectroscopy (SORS)²² have shown promising results for noninvasive blood glucose testing. However, these Raman spectroscopy methods require subject-specific training to build a proper mathematical model for each user, introducing additional procedures in practical applications. The main hindrance to higher robustness and accuracy in Raman spectroscopic measurements is the broad and strong fluorescence background signal from the skin surface. Therefore, a Raman spectroscopy method to reduce

A full list of affiliations appears at the end of the paper. ✉e-mail: lin.zhou@photonview.com; gning@sibs.ac.cn; changchen@sjtu.edu.cn; wqingw@shsmu.edu.cn

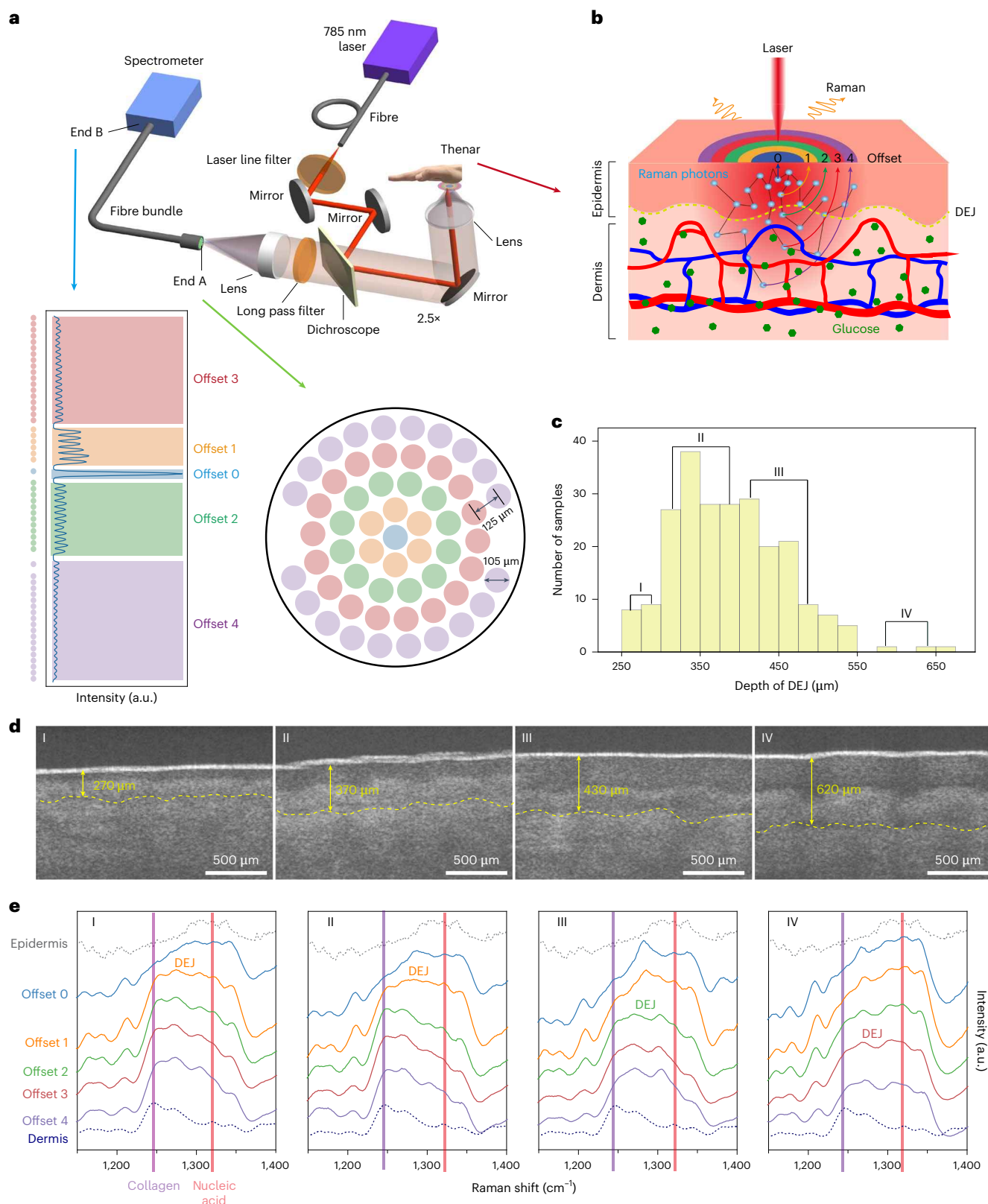


Fig. 1 | μ SORS system detects Raman signals from epidermis to dermis with depth selectivity. **a, Schematic of μ SORS system. μ SORS setup (top). Zoomed-in layout of fibres in the fibre bundle at End A (bottom right). Typical intensity profile across offsets 0–4 in the fibre bundle at End B (bottom left). **b**, Schematic of μ SORS detection on thenar. Yellow dashed curve indicates DEJ; green hexagons show glucose molecules; cyan dots indicate Raman photons. Schematics of blood vessels and skin layers were adapted from ref. 47 with permission. **c**, Histogram of DEJ depths from 232 human thenar samples**

identified by OCT. Roman numerals (I–IV) indicate four different depth ranges of DEJ, corresponding to OCT images in **d**. I, 250–300 μ m; II, 300–400 μ m; III, 400–500 μ m; IV, 575–600 μ m. **d**, Typical OCT images of four samples with mean DEJ depths of 270 μ m, 370 μ m, 430 μ m and 620 μ m were selected from I–IV marked in **c**. **e**, μ SORS spectra from the same samples in **d**, along with reference Raman spectra taken from ex vivo epidermis and dermis samples of human skin. Pink and purple shades indicate characteristic Raman peaks of nucleic acid and collagen.

Table 1 | Detection depth of each offset gauged by OCT and μ SORS spectra

Samples	I	II	III	IV	Depth (μ m)	Suitable
Thickness (μ m)	270	370	430	620	Depth (μ m)	Suitable
Offset 0	Epidermis	Epidermis	Epidermis	Epidermis	<270	0
Offset 1	Mix	Mix	Epidermis	Epidermis	270–370	46%
Offset 2	Dermis	Dermis	Mix	Epidermis	370–430	72%
Offset 3	Dermis	Dermis	Dermis	Mix	430–620	99%
Offset 4	Dermis	Dermis	Dermis	Dermis	>620	100%

Table 2 | Statistics of the 35 participants in the preliminary BESH

Statistics	Preliminary BESH (n=35)	
Participants (n)	With T2D (n=20)	Without diabetes (n=15)
Sex, male: female (%)	17 (85.0): 3 (15.0)	8 (53.3): 7 (46.7)
Age, years (mean \pm s.d., range)	47.6 \pm 8.4, 30–60	35.7 \pm 3.8, 30–60
BMI, kg m^{-2} (mean \pm s.d., range)	24.5 \pm 4.1, 17.7–31.8	24.3 \pm 4.0, 19.2–32.7
FPG, mmol l^{-1} (mean \pm s.d., range)	8.9 \pm 2.0, 5.1–12.4	5.4 \pm 0.4, 4.4–5.7
OGTT time, h (points)	5 (12)	
Sampling point, min	0, 10, 30, 60, 90, 120, 150, 180, 210, 240, 270, 300	
VPG, mmol l^{-1} (range)	2.9–31.8	
Data pairs, VPG and spectra	415	

the interference of the skin surface signal when capturing deeper glucose signals is imperative for clinically applicable noninvasive blood glucose monitoring.

In this work, we present multiple μ -spatially offset Raman spectroscopy (μ SORS), a technique capable of directly measuring Raman signals from both epidermal and dermal layers of human skin, and thus, potentially feasible for clinical noninvasive blood glucose monitoring. Utilizing an optical probe with fibre layout at five different offsets, μ SORS realized depth-selective detection of Raman signals, with larger offsets capturing a higher proportion of signals from greater depths. We first conducted a preliminary basic experimental study with humans (BESH) involving 35 participants that demonstrated that in contrast to the Raman signal from the skin surface, the μ SORS signal from deeper layers, especially around or below the dermal–epidermal junction (DEJ)²³, exhibits a statistically notable correlation of Raman glucose peaks to venous plasma glucose (VPG) levels. Based on this optimal detection depth, we then expanded the BESHs, monitoring the VPG of additional 230 participants while collecting Raman spectra from the optimal offsets using μ SORS. A partial least squares (PLS) regression model²⁴ was applied to predict the blood glucose level from the Raman spectra. Using independent training and test dataset consisting of data from different individuals (individual-independent), the model reached a mean absolute relative difference (MARD) of 14.6%, with 99.4% of the predictions in clinically acceptable zones of the consensus error grid (CEG; A + B)²⁵. This result indicates that μ SORS achieves a high accuracy in blood glucose measurement without personalized calibration and data acquisition, marking a valid demonstration of a clinically applicable technology for noninvasive blood glucose monitoring.

Results

μ SORS detects depth-selective Raman signals in skin layers

We tailored μ SORS for depth-selective detection of Raman signals from human skins. SORS is an advanced spectroscopic technology,

known for its ability to detect Raman signals beneath surfaces²⁶, and is widely applied in applications such as cargo content inspection²⁷, archaeology²⁸, cancer screening²⁹ and pharmaceutical analysis³⁰. Here, we reformed this technology at the scale of tens to hundreds of micrometres, aiming to obtain Raman signals from various depths of the skin to realize noninvasive blood glucose monitoring. An optical probe focused a 785-nm laser on the sample (human thenar in this work) and then collected the backscattered photons, directing them to a concentrically organized fibre bundle (Fig. 1a, top). The concentric layers of fibres were designed to capture photons emitted at specific lateral offsets, which were 0 μ m (offset 0), 50 μ m (offset 1), 100 μ m (offset 2), 150 μ m (offset 3) and 200 μ m (offset 4) from the incident beam centre, respectively (Fig. 1a, bottom right). The signal intensity is notably lower for larger offsets (Fig. 1a, bottom left). Nevertheless, the concentric layout led to more fibres at greater offsets, compensating for the decrease in signal intensity. We used a series of bilayer samples to assess the depth-selective detection capability of μ SORS^{26,31} (Extended Data Fig. 1a,b and Methods). Each offset exhibited a maximum intensity of the bottom layer at a different detection depth, indicating that Raman photons backscattered from larger offsets had a higher probability to have originated from greater depths (Extended Data Fig. 1c). Therefore, μ SORS technology proves capable of selectively collecting Raman signals at various depths on a sub-millimetre scale.

For the purpose of noninvasive glucose detection, the key is to acquire Raman signals dominated from the dermis, which is rich in interstitial fluid (ISF) and capillary loops and could provide direct evidence of blood glucose levels (Fig. 1b)³². The dermis lies under the DEJ, the depth of which can be identified from the optical coherence tomography (OCT) image (Extended Data Fig. 2). We first observed the biological variation in the histogram of DEJ depths from 232 samples (thenar from both hands of 116 individuals), which ranged from 250 to 700 μ m, with the most common depth around 350 μ m (Fig. 1c). We then selected four typical individuals with different DEJ depths (labelled I–IV, in the order of increasing DEJ depth; Fig. 1d and Extended Data Fig. 3) and measured their μ SORS spectra (Fig. 1e, offsets 0–4). Compared with the reference Raman spectra taken from ex vivo human epidermis and dermis samples (dashed lines in Fig. 1e, Extended Data Fig. 4 and Methods), the shape of spectra from offsets 0–4 exhibited a clear transition from epidermis-like to dermis-like for all four individuals, with corresponding shifts in the relative intensities of the Raman peaks assigned to collagen and nucleic acid (Fig. 1e). It is assumed that the distinct spectral features within the 1,200–1,400 cm^{-1} range, particularly evident in the relative intensities of the collagen Raman peak (1,240 cm^{-1}) and the nucleic acid Raman peak (1,320 cm^{-1})^{33–35}, mainly result from the compositional difference. This difference is shown in the skin tissue cross-section, where the epidermis consists of densely packed cells, whereas the dermis is rich in collagen (Extended Data Fig. 4 and Methods).

Combining the spectral transition and the DEJ depths derived from OCT, we can roughly characterize the detection depth of μ SORS in human thenar skin. The transition of μ SORS spectra from epidermis-like to dermis-like occurred at smaller offsets for samples with shallower DEJ depths and vice versa (Fig. 1e). Based on this trend,

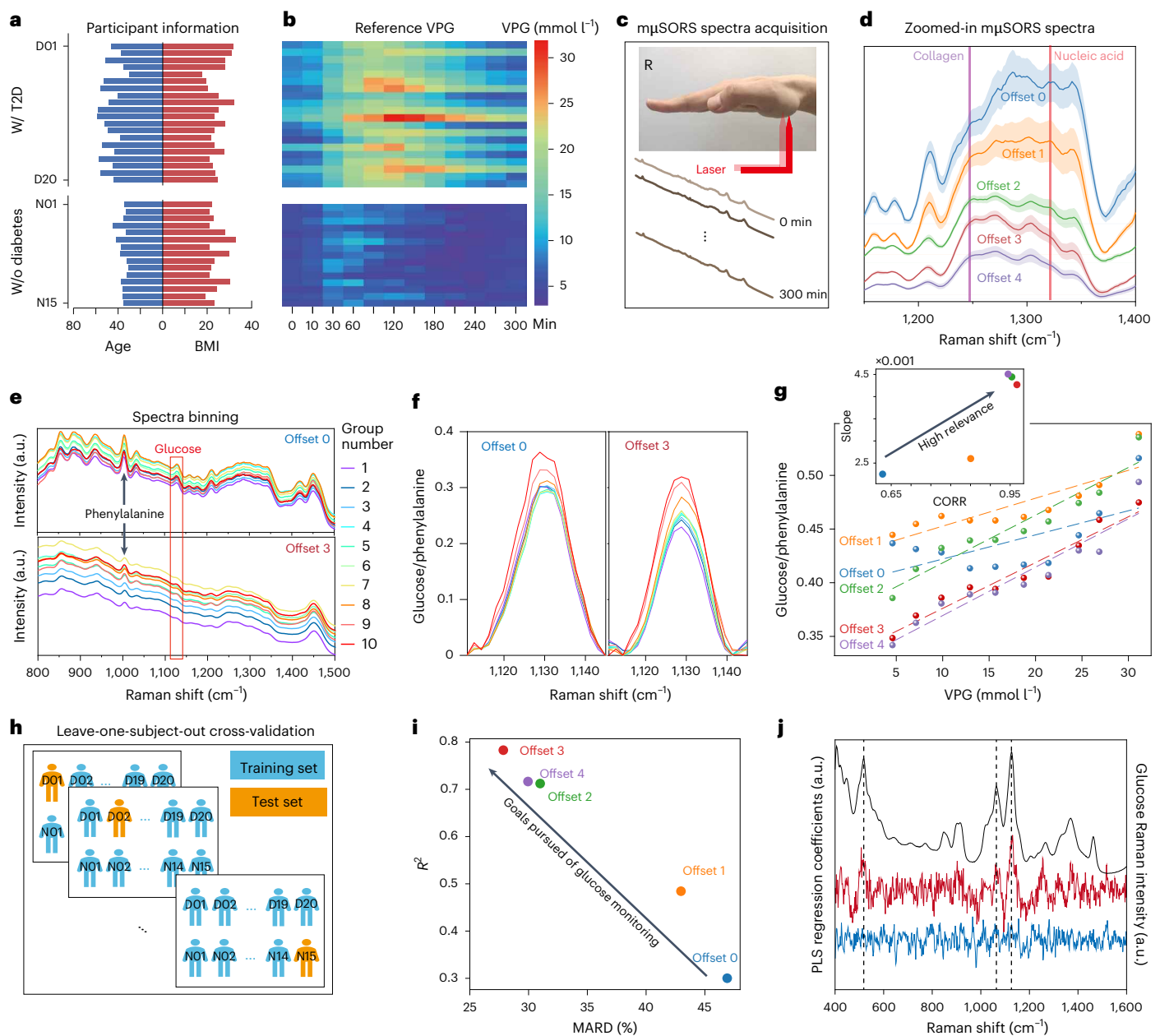


Fig. 2 | Correlation between μ SORS spectra and blood glucose levels in the preliminary BESH on 35 participants. **a**, Distribution of age and BMI of the 35 participants. **b**, VPG levels measured at 12 sampling points over the 5-h OGTT. **c**, Schematic of μ SORS spectra acquisition during OGTT. R, Right hand. **d**, Spectra averaged over all participants at each offset, zoomed in between 1,150 and 1,400 cm^{-1} . Solid lines indicate mean spectra. Shaded areas indicate s.d. Pink and purple shades show characteristic Raman peaks of nucleic acid and collagen. **e**, Mean μ SORS spectra from ten VPG bins with group number from 1 to 10. Offset 0 (top); offset 3 (bottom). **f**, Zoomed-in spectra around glucose

peak (red rectangle in **e**) after normalized by the phenylalanine band. Offset 0 (left). Offset 3 (right). **g**, Normalized glucose Raman band (**f**) against VPG levels for each offset. Dashed lines, linear fittings. Inset shows Pearson correlation coefficients and slopes of linear fittings. **h**, Schematic of the leave-one-subject-out cross-validation scheme for the PLS model. **i**, Metrics of model performance in **h** at different offsets. R^2 , coefficient of determination. **j**, Averaged regression coefficients obtained from **h** (light blue, offset 0; red, offset 3) and Raman spectrum of glucose solution (black). Black dashed lines indicate that the regression coefficients of offset 3 captured important spectral peaks of glucose.

we can use the DEJ depth determined by OCT as a 'ruler' to gauge the depth measured by a given offset of μ SORS. We thus roughly estimated the detection depths of five μ SORS offsets: 0–270 μm for offset 0, 270–370 μm for offset 1, 370–430 μm for offset 2, 430–620 μm for offset 3 and >620 μm for offset 4 (Table 1). In addition, μ SORS spectra at offsets 3 and 4 displayed dermis-like shapes or at least a mixture of epidermis-like and dermis-like features in all samples. Even offset 2 showed mixed features in Sample III, where the DEJ is deeper than 72% of all the 232 samples (Table 1). These results indicate that μ SORS also has a capability for depth-selective detection in human

skin, and it could effectively capture signals from the dermis for most individuals using offsets 2–4.

Dermal Raman spectra demonstrate high correlation with VPG
Having verified that μ SORS can selectively detect signals from various depths, including those deeper than the DEJ in human thenar skin, we proceeded to evaluate its capability for measuring glucose in the skin and predicting the blood glucose at a clinical setting. We conducted a preliminary BESH with 35 participants (Table 2 and Fig. 2a), in which we measured both μ SORS spectra from their right-hand thenar and their

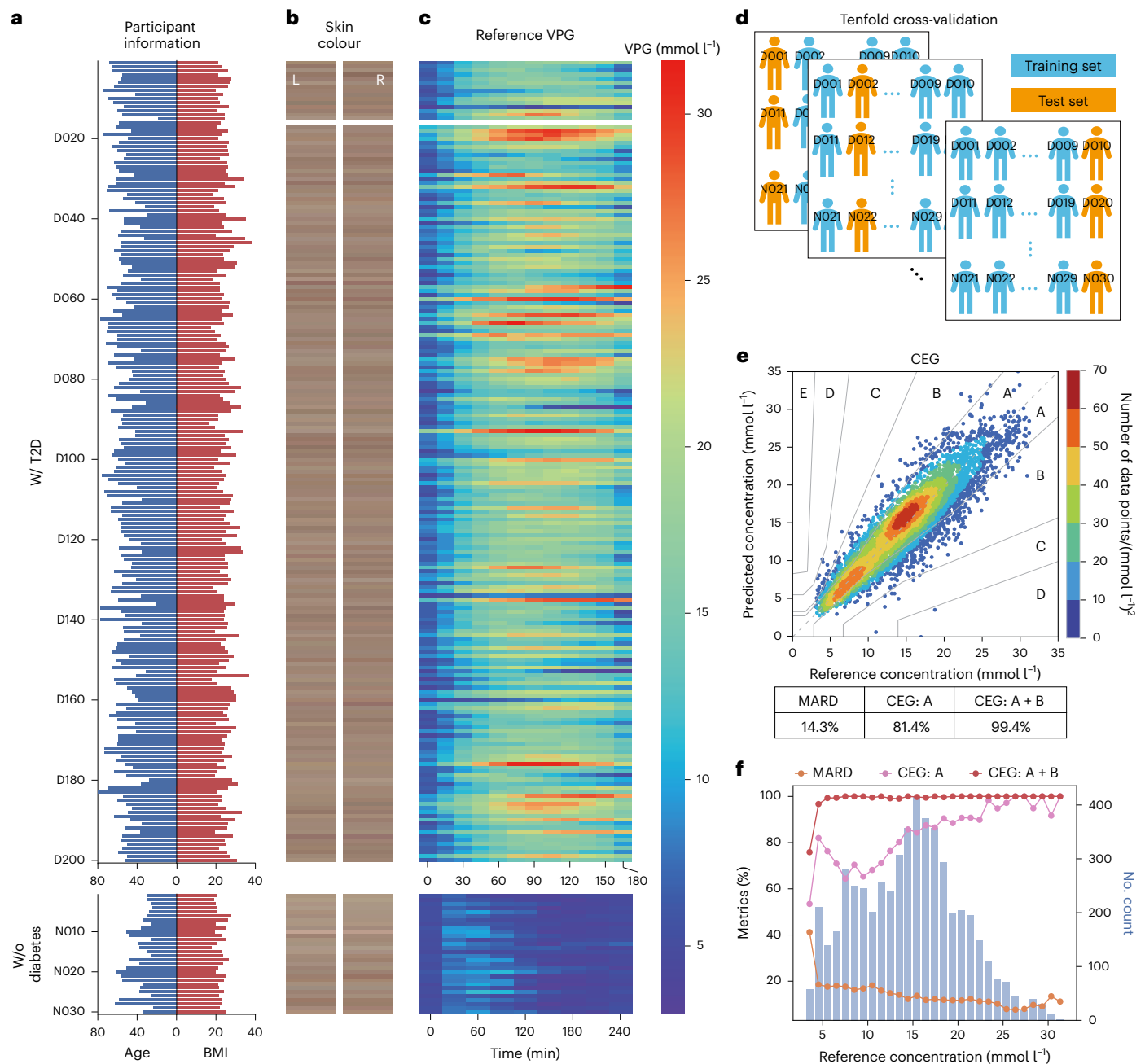


Fig. 3 | Blood glucose prediction of the 230 participants in expanded BESHs with subject-wise tenfold cross-validation. **a**, Distribution of age and BMI among the 230 participants. **b**, Thenar skin colours of the 230 participants. L and R indicate left and right hands, respectively. Missing data are marked in blank white. **c**, VPG levels of 230 participants measured during OGTT. **d**, Schematic of the subject-wise tenfold cross-validation scheme. Blue, training

set. Orange, test set. **e**, CEG of predictions from the PLS regression model in the cross-validation (**d**). Colours indicate the local density of data points. **f**, Model performance metrics plotted against reference glucose concentration. Orange, MARD. Magenta, percentage of data points in the A zone of the CEG (CEG A). Red, percentage of data points in the A or B zones of the CEG (CEG A + B). Blue shade, histogram of reference glucose concentrations (VPG).

VPG concentrations during a 5-h oral glucose tolerance test (OGTT) (Fig. 2b,c). Their VPG levels ranged from 2.9 to 31.8 mmol l⁻¹, covering the physiological to pathological blood glucose region (Table 2 and Fig. 2b). Individuals were free to take their hands off the setup or walk around in the sampling intervals (Fig. 2c). A total of 415 μSORS spectra sets (offsets 0–4) were acquired (Fig. 2d), each corresponding to VPG levels measured at the same time points, yielding 415 VPG–spectra data pairs. Consistent with before (Fig. 1e), the average spectra from the preliminary BESH exhibited a transition from epidermis-like to dermis-like with increasing offsets. Moreover, offsets 2–4 displayed highly similar spectral shapes and dermis-like spectral features between

1,150 and 1,400 cm⁻¹, indicating that all these three offsets are capable of detecting dermal signals (Fig. 2d).

To analyse Raman spectra across different glucose levels at different offsets, we categorized all the 415 VPG–spectra data pairs into ten groups based on the VPG level (equal binning; Fig. 2e and Supplementary Table 1). To account for variations in absolute spectrum intensity across groups, we normalized the glucose Raman band using the phenylalanine Raman band at 1,001 cm⁻¹, because phenylalanine is abundant in solid skin tissue compartments such as lipids, proteins and collagen. With a larger offset that can detect dermal signals, such as offset 3, the normalized glucose Raman peak increased notably

Table 3 | Statistics of the 230 participants in expanded BESHs

Statistics	Expanded BESHs (n=230)	
Participants (n)	With T2D (n=200)	Without diabetes (n=30)
Sex, male: female (%)	124 (62): 76 (38)	15 (50): 15 (50)
Age, years (mean±s.d., range)	55.1±11.4, 18–80	36.1±11.3, 22–59
BMI, kg m ⁻² (mean±s.d., range)	24.8±3.8, 16.2–38.1	22.5±2.5, 21.6–25.5
FPG, mmol l ⁻¹ (mean±s.d., range)	8.50±2.18, 4.82–17.84	5.15±0.32, 4.37–5.98
OGTT time, h (points)	3 (12)	4 (9)
Sampling, min	0, 15, 30, 45, 60, 75, 90, 105, 120, 135, 150, 180	0, 30, 60, 90, 120, 150, 180, 210, 240
VPG, mmol l ⁻¹ (range)	3.9–31.2	2.94–11.48
Data pairs, VPG and spectra	4,768	540
Statistics	Total data pairs (n=5,308)	

with VPG across the ten groups, exhibiting a trend not seen at offset 0 (Fig. 2f and Extended Data Fig. 5). Linear correlation analysis revealed a high correlation (with a Pearson correlation coefficient (CORR) of 0.94–0.97) between VPG and the normalized glucose Raman band at offsets 2–4, much higher than the correlation at offset 0 (CORR = 0.63) and offset 1 (CORR = 0.85) (Fig. 2g). The normalized glucose Raman band at offsets 2–4 also demonstrated notably greater sensitivity to VPG, as indicated by the steeper slopes in the linear fit (Fig. 2g, inset), suggesting that Raman spectra from dermal skin layers offer more relevant information about blood glucose levels. Both correlation and sensitivity to VPG are very similar for offsets 2–4 (Fig. 2g, inset), consistent with the highly similar shapes of average spectra observed at these three offsets (Fig. 2d).

To further determine the optimal offsets for individual-independent blood glucose monitoring, we built a PLS regression model to fit the VPG–spectra pairs from each offset individually, taking advantage of Raman features across the full spectral range. A leave-one-subject-out cross-validation scheme (Fig. 2h) was applied²⁴. The results indicated that offset 3 yielded the highest accuracy, closely followed by offset 4 and offset 2 (Fig. 2i). Notably, these offsets encompass the DEJ depths in the majority of individuals (Figs. 1c–e and 2d), supporting our hypothesis that signals from below the DEJ are more suitable for noninvasive blood glucose monitoring. In addition, our data analysis algorithm provided direct evidence of leveraging glucose-specific Raman spectral information. The PLS regression coefficients trained on spectra from offset 3 (Fig. 2j, red curve) aligned well with the characteristic Raman bands of glucose solution (Fig. 2j, black curve), a distinctive feature absent at offset 0 (Fig. 2j, blue curve). This alignment suggests that while analysing Raman signals from offset 3, we can leverage more directly relevant spectroscopic information of glucose molecules than other biomolecules in human skin. In contrast, at offset 0, neither glucose nor other biomolecular signals could be clearly identified.

Accurate and individual-independent glucose predictions

With the preliminary BESH, we identified direct evidence of glucose molecules in m μ SORS spectra, and determined that the optimal offsets to detect blood glucose Raman signals were offsets 2–4. However, due to the small sample size, the prediction accuracy remained low (MARD = 28.0% for offset 3) and failed to meet the clinical standards. To further improve the prediction accuracy, we initiated expanded BESHs of 230 individuals with two major improvements: (1) Raman spectra

were collected from the thenar of both hands to augment the dataset and eliminate hand-specificity; (2) spectra from offsets 2 and 3 were combined as the input to the PLS model according to the results of the preliminary BESH (Fig. 2i), whereas offset 4 was removed from the device due to its high spatial cost (requiring more fibres than other offsets; Fig. 1a) despite its high prediction accuracy. The 230 participants covered a wide range of age (18–80 years) and body mass indices (BMIs; 16.2–38.1 kg m⁻²) (Fig. 3a and Table 3). A relatively balanced representation of sex (91 female and 139 male; Table 3) and varied skin colours were also achieved (Fig. 3b). VPG levels of individuals ranged between 2.94 to 31.64, effectively covering the entire extent of physiological to pathological blood glucose levels (Fig. 3c and Table 3).

At each sampling point of the OGTT, we measured VPG and two m μ SORS spectra from the two hands of the participant, yielding a total of 5,308 VPG–spectra data pairs, -13 times larger than the dataset in the preliminary BESH. Each of these spectra was averaged over 60 frames (8 s per frame), providing a database with 318,480 single spectra in total. Spectra from offsets 2–3 and both hands were simultaneously used for model training and testing (with more details in Methods), generating separate predicted glucose concentrations for the left and right hands. Practically, this hand-independent approach allows users to freely choose either hand for blood glucose monitoring, thereby adding flexibility in the clinical use.

We employed a subject-wise tenfold cross-validation scheme (Fig. 3d)³⁶ to evaluate the prediction accuracy of m μ SORS for individual-independent blood glucose monitoring. Similar to the leave-one-subject-out scheme used in the preliminary BESH (Fig. 2), this approach simulated a scenario where a user's blood glucose levels can be directly measured and monitored without the need for personalized pre-calibration, validating the applicability of m μ SORS in real-life clinical settings and distinguishing it from various other works in the field¹⁹. Consequently, a total of 5,308 predicted glucose concentration values were generated, with each VPG value corresponding to two predicted concentration values, one from the left hand and the other from the right hand. Overall, 99.4% of these points fell within the clinically acceptable range (CEG A + B), achieving a MARD value of 14.3% (Fig. 3e). No significant difference in accuracy between female and male participants (13.43 ± 5.79% versus 14.98 ± 6.23%; *P* = 0.06, two-sample *t*-test) or between left and right hand (14.62 ± 6.65% versus 14.12 ± 7.16%; *P* = 0.247, paired sample *t*-test) was observed (Extended Data Figs. 6–8). For each participant, the predictions from the left-hand and right-hand spectra exhibited good consistency with each other, closely aligning with the VPG values and trends (Extended Data Figs. 6–8). Furthermore, the MARD value consistently remained below 20%, and the CEG A + B exceeded 99% across nearly all VPG intervals (Fig. 3f). In summary, m μ SORS provides real noninvasive blood glucose monitoring that is both accurate and flexible in clinical settings, without the need for personalized calibration.

Practical glucose monitoring on an independent test set

To mimic the conditions of clinical blood glucose monitoring even more closely and further validate the clinical applicability of m μ SORS, we performed model training and testing on two independent datasets. Overall, 30 participants (25 with type 2 diabetes (T2D) and 5 without diabetes) recruited at the end of each BESH were selected as an independent test set, while the rest 200 participants comprised the training set (Fig. 4a, Supplementary Table 2 and Extended Data Fig. 9). This generated 4,618 VPG–spectra data pairs in the training set and 690 in the test set, with diverse blood glucose trends and broad VPG distributions in both datasets. A PLS model was exclusively trained on the training set, after which the resulting regression coefficients were locked, and then used to predict the blood glucose level in the test set (Fig. 4a). A MARD value of 14.6% was achieved in the test set with 99.4% of predictions within the CEG A + B zone (Fig. 4b). Examining the prediction accuracy across different VPG concentrations, the

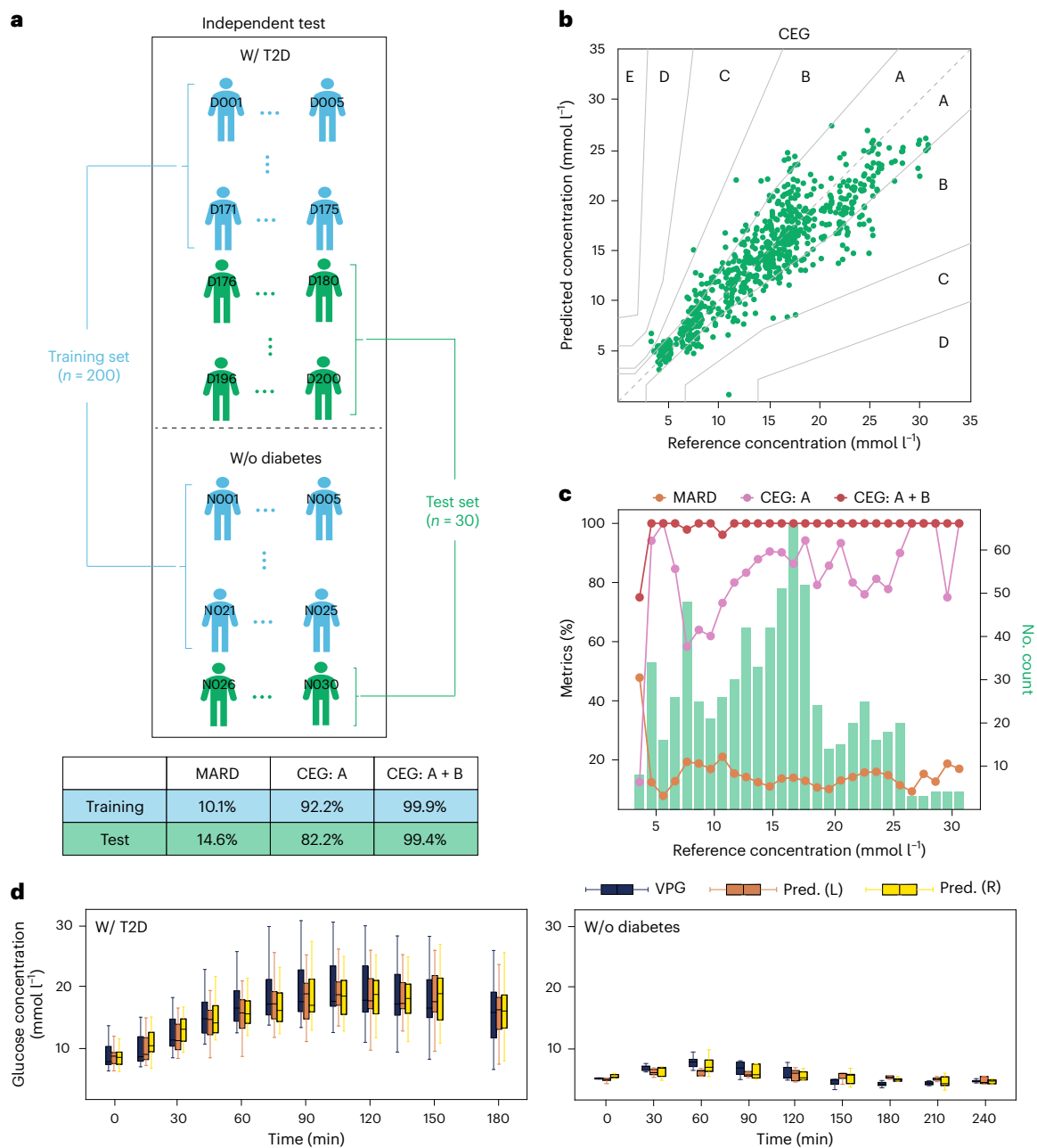


Fig. 4 | Blood glucose predictions on an independent test dataset. **a**, Schematic of model training ($n = 200$) and testing ($n = 30$) on independent datasets (top). Metrics of model performance on the training and test sets, respectively (bottom). **b**, CEG of predictions from the PLS regression model on the test set. **c**, Model performance metrics plotted against reference glucose concentration in the test set. Orange, MARD. Magenta, CEG A. Red, CEG A + B. Green shade, histogram of reference glucose concentration. **d**, Overall trends of predicted (orange, left hand; yellow, right hand) and reference glucose concentrations (dark blue) for participants with T2D (left, $n = 25$) and without diabetes (right, $n = 5$) in the test set during OGTT. In the box plot, box boundaries indicate Q1 (25th percentile) and Q3 (75th percentile), whiskers indicate Q1 $- 1.5 \times$ IQR and Q3 $+ 1.5 \times$ IQR and the centre indicates the median.

CEG A + B ratio consistently reached 100% in 25 out of 28 VPG intervals (1 mmol l^{-1} each), and the MARD value was lower than 20% in 26 out of 28 VPG intervals (Fig. 4c). These results in the independent test dataset again underscored the prominent capability of μSORS for noninvasive blood glucose monitoring.

For both hands, the predicted trends of blood glucose during OGTT closely matched the VPG trends, regardless of whether the individuals had diabetes (Fig. 4d). For participants with T2D, both VPG and predictions depicted monophasic OGTT response curves typical of T2D patients, in which the blood glucose level increases after the ingest of glucose and then decreases after reaching a peak³⁷. On the

other hand, the flat response curves observed in participants without diabetes reflected the capability of μSORS to generate accurate trend predictions even within the normal VPG range.

When it comes to every individual, the predicted glucose concentrations still demonstrated high accuracy and good alignment with the VPG, regardless of which hand the predictions came from (Fig. 5). This confirms the robustness of our system and offers users the flexibility to choose either hand for blood glucose measurements. In greater detail, participant D190 with the most accurate predictions in the test set showed a MARD value for both hands as small as 7.6%. Most participants showed typical prediction accuracy with MARD values

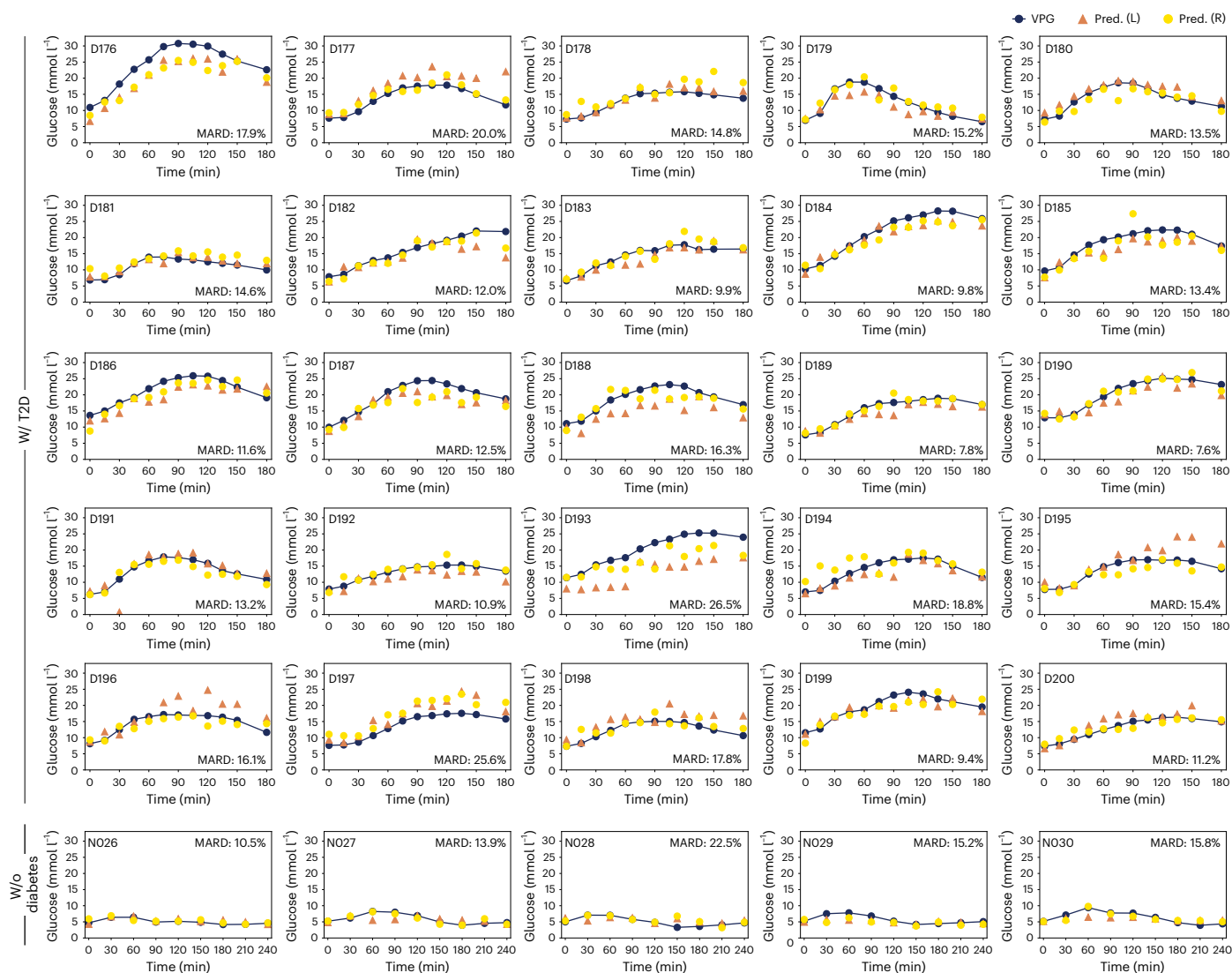


Fig. 5 Blood glucose prediction results for 30 participants in the test set with independent model testing. Dark blue shows reference glucose concentration during OGTT. Orange triangles show predictions from the left hand. Yellow circles show predictions from the right hand.

between 10% and 15%. Even for the participant with the highest MARD in the test set (D193, MARD = 26.5%), the predictions demonstrated a clear trend of increasing blood glucose concentration, consistent with the change of VPG, as well as a close proximity between predictions given by the two hands (Fig. 5). In summary, with the more rigorous validation provided by the independent test set, μ SORS once again proved itself of high accuracy and solid practical viability in clinical blood glucose monitoring.

Discussion

Depth-selectable sensing is critical to robust measurement of chemical levels in the blood. Based on the SORS technology^{22,38}, we developed the μ SORS system, in which the specially designed optical probe allows lateral offsets at the scale of tens of micrometres (Fig. 1a,b). Tested on a bilayer sample with tunable thickness of the surface layer, μ SORS achieved a depth resolution of 50–100 μ m (Extended Data Fig. 1c), which is a notable improvement from the millimetre resolution of the traditional SORS technology. Furthermore, combining the Raman spectral features and the DEJ depth estimated from the OCT data, we can conclude that the depth resolution of μ SORS in human skin is around 100–200 μ m (Fig. 1d,e and Table 1) and that for the majority of participants, the Raman signals from dermis layer can be captured

with offsets 2–4 (Table 1), which is well suited for noninvasive blood glucose sensing. In our preliminary BESH, a clear distinction emerged that Raman signals from the skin surface exhibited a much weaker correlation to VPG, whereas those from deeper depths corresponding to larger offsets displayed a precise linear correlation. In the expanded BESHs, utilizing spectra from offsets 2–3, our PLS model achieved high prediction accuracy for individual-independent and noninvasive blood glucose monitoring, with a MARD less than 15% and more than 99% predictions falling within the A + B zone of the CEG plot. Therefore, the critical and irreplaceable advantage of μ SORS in noninvasive blood glucose monitoring becomes evident. Meanwhile, it also offers a practical solution to systemic study on subsurface sensing.

Offsets 2–4 emerged as the most critical offsets with the highest relevance to the VPG concentration in the preliminary BESH (Fig. 2i). Combining OCT images and μ SORS spectra, we concluded that these offsets measured signals deeper than 370 μ m and up to over 620 μ m, beyond the DEJ in most participants (Fig. 1c and Table 1). This observation reaffirms our conclusion that DEJ is a critical depth for blood glucose monitoring, where both ISF and capillaries contribute to the detection of glucose Raman signals by μ SORS (Fig. 1b). Despite offset 4 having the deepest detection depth, its prediction accuracy was slightly lower than offset 3. This suggests that excessive detection

depths may actually reduce the accuracy of blood glucose measurement, likely due to the low signal-to-noise ratio caused by intensity decay in deeper layers. Therefore, considering the trade-off between human skin composition and the signal-to-noise ratio, the optimal depth for blood glucose monitoring could be just below the DEJ. Recent experiments of noninvasive blood glucose measurements in mice also targeted this depth, agreeing with our results that the signal from the DEJ is highly related to the VPG level¹⁵.

μ SORS-based blood glucose monitoring is characterized by its exceptional robustness, which provides great flexibility for the users. First, the depth-specificity of the signal and the high signal-to-noise ratio of the optical system enabled a completely noninvasive approach, effectively substituting traditional needles with laser technology. Second, users can freely move away from the device during sampling intervals. This design highlights an important advantage of our technology: it is highly robust to the reposition of hands which is usually considered as a difficult challenge in previous work. With this unique feature, there is no need to constantly attach the device on the patient, providing more convenience and comfort of using noninvasive glucose measurements. Most notably, μ SORS allows for individual-independent blood glucose monitoring. It eliminates the need for user-specific device calibration or model training, while still reaching clinically valuable MARD lower than 15%. Last but not least, a high accuracy was consistently achieved across the vast majority of VPG levels, covering nearly the entire physiological to pathological blood glucose range (Figs. 3f and 4c). It was also independent of the sex of the user and from which hand the spectra were measured. Therefore, μ SORS-based blood glucose monitoring can be applied to most random participants without any previous preparation and instantaneously acquire reliable predictions, a distinctive feature not achieved by many other recent technologies in the field^{18,19}.

Despite substantial technological advances and clinical applicability, μ SORS is still faced with several challenges. First, the prediction accuracy is still limited for a small percentage of participants. Second, μ SORS requires a relatively long acquisition time to reduce noise and distinguish Raman bands from the background signal. This potentially limits the model's accuracy to capture rapid glucose fluctuations, such as those during immediate correction of hypoglycaemia episodes caused by antidiabetic medication. Another important shortcoming is that μ SORS is still a large setup with a size comparable to a desktop computer. Moreover, thenar is the only measuring site so far due to its flat, large and soft surface, and we lack data for other possible areas of human skin. Finally, given that our BESHs were performed in China, additional local datasets are to be built when using μ SORS in other countries, considering potential physiological differences across ethnicities.

Future technological advances are expected to improve μ SORS from multiple aspects and address the challenges above. With the accumulation of more cases in further BESH or clinical studies, our PLS model could be refined to cover the physiological diversity of the population. More complicated algorithms, especially deep neural networks³⁹, are also expected to enhance the prediction accuracy of μ SORS and make it effective for a broader spectrum of users. The cause of the long acquisition time is that fluorescence from the tissue is still dominating, forming a strong optical background and also introducing considerable shot noise. Multiple newly developed technologies, such as time-gating technology, are promising to reduce the fluorescence background⁴⁰. Incorporating these technologies may reduce the time and laser power required for spectra collection, and even enable noninvasive monitoring of other chemicals in human bodies. Efforts are underway to transform this machine into a portable or even wearable device. This involves miniaturizing the Raman spectrometer to a chip level using spatial heterodyne spectroscopy that can be fabricated in a 200 mm CMOS compatible silicon

photonics platform⁴¹. Such chip technology may also reduce the cost of μ SORS, making it more affordable to the general public. Furthermore, packing μ SORS into a wearable device could extend its capability to measure various sites on human skin, some of which may have a thinner epidermis compared with the thenar region (for example, neck, abdomen, wrist or thigh)⁴². Glucose Raman spectra measured at these sites may attain higher signal-to-noise ratios due to shallower DEJ depths.

To sum up, we presented μ SORS technology, which is capable of measuring a depth-selective Raman signal, including glucose-related spectra from the dermis of human skin. This detection capability enables μ SORS to realize noninvasive blood glucose monitoring with high accuracy, without the need for personalized calibration.

Methods

μ SORS system design and setup

As shown in the overall schematic (Fig. 1a), a 65-mW laser was generated using a 785-nm diode multimode laser source (Cobolt 08-NLD) and directed through an optical probe to focus on the sample in a \sim 40- μ m spot. The scattered photons were collected using the same probe, filtered with a long-pass filter and then directed to a fibre bundle. The fibre bundle directed the signal to a near-infrared spectrometer (Blaze 400HR, LS785, Teledyne Princeton Instruments) equipped with an electrically cooled charge-coupled device.

To distinguish photons emitted with different offsets from the incident beam, at End A of the fibre bundle, the optical fibres were arranged in concentric ring structures (Fig. 1a). Each ring corresponded to a different offset between 0 μ m and 200 μ m at the surface of the sample, with a spacing of 50 μ m between adjacent offsets. This spacing step matches the distance between adjacent fibres of 125 μ m, after the 2.5-fold magnification by the lens (Fig. 1a). At End B of the fibre bundle, the fibres were arranged linearly and grouped according to their offsets before being directed to the spectrometer (Fig. 1a).

μ SORS system characterization with bilayer samples

0–15 Scotch tapes with 50- μ m thickness were layered on silicon substrate to create 16 bilayer samples, with the total tape thicknesses (top layer) ranging from 0 μ m to 750 μ m. We tested each sample three times at different locations with an acquisition time of 6 s. The Raman band area of Si was calculated with the integrals within the range of 500–540 cm^{-1} (Extended Data Fig. 1). For each offset, the areas of Si band from all 16 bilayer samples were normalized by their maximal value (Extended Data Fig. 1c).

Spectral calibration

After the acquisition of μ SORS spectra, a spectral calibration was performed using a neon–argon lamp (IntelliCal, Princeton Instrument). For each fibre, the pixels corresponding to ten standard neon–argon peaks were identified, and a four-order polynomial function was fitted between these identified pixels and the corresponding wavelengths for each fibre independently, thereby establishing the desired correspondence between spectrometer pixels and wavelengths. The wavelengths were then converted to the wavenumbers, which were later interpolated to the same abscissa for the spectra from all the fibres.

Human DEJ depth determination with OCT imaging

We performed OCT (Ganymede SD-OCT System, Thorlabs) on 232 thenars of both hands for $n = 116$ participants. For each hand, an area of 3 mm (x) \times 3 mm (y) was scanned up to a maximal depth (z) of 1.95 mm. The spatial resolution was 3.81 μ m in x and z dimensions and 12 μ m in the y dimension (Extended Data Fig. 2a). The refractive index of the target was set to 1.3. An intensity profile along the z dimension was calculated by averaging all the pixels along both x and y dimensions. The DEJ depth of the skin was manually annotated from the intensity profile using the characteristic points (Fig. 1d and Extended Data Fig. 2b).

Measurements on ex vivo human skin samples

After obtaining human skin tissue via punch biopsy, the sample was immediately fixed in 10% formaldehyde to preserve its architecture. It was then dehydrated through a gradient of alcohol, cleared with xylene and infiltrated with paraffin wax to form a solid block. The paraffin block was sliced into thin sections using a microtome and affixed to glass slides. These slides were subsequently analysed under bright-field microscopy using a WITec alpha 300 imaging system.

Ex vivo fresh human skin tissue from a participant was cut manually to prepare epidermal and dermal samples, which were diluted with phosphate-buffered saline (Hyclone), placed on a glass slide and sealed with a cover glass for Raman spectra measurements (WITec alpha 300) with a laser power of 75 mW and acquisition time of 120 s. Ex vivo human skin tissues used in this study have been sourced from the study approved by the Institutional Review Board of Ruijin Hospital (no. 2023-166) and Human Genetic Resource Administration of China. Both participants have provided written informed consent, which include a written description authorizing the use of his/her samples for other research.

Raman spectrum of glucose solution

The 1,000 mmol l⁻¹ glucose stock solution (Macklin, G885129) was loaded onto the probe with a pipette and its m μ SORS spectra were measured with an acquisition time of 8 s. The Raman spectra of glucose solution detected by offset 0 of m μ SORS system was used in this work (Fig. 2j).

Basic experimental study with humans

In the preliminary BESH, 20 participants with T2D and 15 participants without diabetes were selected. For the expanded BESHs, 200 participants with T2D and 30 participants without diabetes were included (Supplementary Table 2). The statistics of their age, sex (determined based on self-report and government-issued personal identity card) and fasting plasma glucose (FPG) levels are given in Tables 2 and 3. The study protocols were approved by the Institutional Review Board of Ruijin Hospital, affiliated with Shanghai Jiao Tong University School of Medicine, according to the Declaration of Helsinki. The studies are registered at ClinicalTrials.gov (NCT05504005, NCT05921344 and NCT06512077). All BESHs were open, and data collection and analysis were not performed blind to the conditions of the experiments. All the participants provided written informed consent and were compensated for their travel reimbursement and sampling.

The individuals were screened 1–7 days before the experiment. In the preliminary BESH, the recruiting criteria for participants without diabetes were that the FPG should be less than 6.1 mmol l⁻¹ and the glycosylated haemoglobin (HbA1c) should be less than 5.7%. For participants with T2D, their FPG levels were between 6.1–13.3 mmol l⁻¹. For the enrolment of T2D participants, it was required that no acute complications of diabetes within 3 months before enrolment, or severe chronic complications of diabetes and comorbidities (including severe structural heart disease, chronic congestive heart failure (NYHA \geq III) and history of severe liver or kidney dysfunction) were observed. All participants had no scars, pigmentation and other factors interfering with the test on the tested part of palm skin. Baseline physical examination, blood biochemistry test and a pregnancy test were conducted to confirm that no clinically notable abnormality was found for any of the participants.

All individuals had been fasted for at least 10 h before an OGTT with 75 g (50 g for individuals without diabetes in the expanded BESHs) glucose was given. Both m μ SORS spectra and the VPG concentration were taken for each participant at 12 (9 for individuals without diabetes in the expanded BESHs) sampling points, where individuals were allowed to move freely between sampling points. In the preliminary BESH, the 12 sampling points spanned across 5 h (0, 10, 30, 60, 90, 120, 150, 180, 210, 240, 270 and 300 min after glucose administration). In the expanded

BESHs, for individuals with T2D, the 12 sampling points spanned across 3 h (0, 15, 30, 45, 60, 75, 90, 105, 120, 135, 150 and 180 min after glucose administration); for individuals without diabetes, the 9 sampling points spanned across 4 h (0, 30, 60, 90, 120, 150, 180, 210 and 240 min after glucose administration) (Tables 2 and 3 and Supplementary Table 2). To measure the VPG concentration in both studies, 2 ml venous blood was taken and the plasma glucose concentration was measured by the biochemistry laboratory using the glucose oxidation method on an autoanalyser (AU5800, BECKMAN).

In the preliminary BESH, m μ SORS spectra (offsets 0–4) were taken from right hand with a total time of 8 min, a spectral range of 214 cm⁻¹ and 2,400 cm⁻¹, an integration time of 8 s and 60 frames averaged for each sampling point. Then, 415 valid VPG–m μ SORS spectra data pairs were acquired and used for data analysis (Fig. 2), while 5 pairs were discarded due to technical problems. In the expanded BESHs, different from before, m μ SORS spectra were taken from both hands simultaneously with two m μ SORS setups. A break was set at 4 min for participants to adjust their hand positions during the 8 min measurement. Overall, 5,308 VPG–m μ SORS spectra (offsets 0, 2 and 3, 0–2,450 cm⁻¹) data pairs were available for data analysis (Figs. 3 and 4), after excluding participant D016 who dropped out of the BESH and eight sampling points of participant D119's left hand due to technical problems. The skin colour of participants was measured using colorimeters (Colorimeter Max, CHN Spec) and saved as coordinates in the CIELAB colour space (Fig. 3b). No substantial improvement was found when skin colour was included in the PLS models.

Evaluation of the correlation between m μ SORS spectra and VPG

In the preliminary BESH, we divided the 415 VPG–spectra data pairs into ten groups based on equal binning of the VPG level (Supplementary Table 1). For each of the ten groups of spectra corresponding to different VPG, the average spectra for each offset were calculated (Fig. 2e and Extended Data Fig. 5). The glucose Raman band was defined as the area under the curve between 1,115 cm⁻¹ and 1,142 cm⁻¹ after removing the baseline (the straight line between the two end points) while that of phenylalanine was defined in the same way but between 990 cm⁻¹ and 1,020 cm⁻¹ (Extended Data Fig. 5)²¹. The ratio between these two was defined as the normalized glucose Raman band. The Pearson correlation coefficient (CORR) between the normalized glucose Raman band and the VPG was calculated to quantify the relevance of the spectra to the VPG (Fig. 2g). The slopes of linear fitting between the normalized glucose Raman band and the VPG were calculated to quantify the sensitivity of the spectra to the VPG (Fig. 2g, inset).

PLS cross-validation

We applied a PLS regression model⁴³ to predict the VPG concentrations from the Raman spectra in the BESHs. In the preliminary BESH, m μ SORS spectra between 400 cm⁻¹ and 1,600 cm⁻¹ from each offset were used as the input to the PLS model. Model cross-validation was conducted in the leave-one-subject-out procedure, where data from one participant was left to be predicted with the model trained on all the other data points, and this process was iterated to cover all participants once in the prediction (Fig. 2h). In the expanded BESHs, different from before, m μ SORS spectra between 320 cm⁻¹ and 2,000 cm⁻¹ from offsets 2 and 3 were concatenated into a single vector as the input to the PLS model. The model performance was evaluated using subject-wise tenfold cross-validation (Fig. 3d), where the dataset of all VPG–spectra pairs was partitioned into ten subsets ('tenfold') based on the last digit of the participant ID ('subject-wise'). In each iteration, one subset was selected as the validation set, while the remaining subsets were combined as the training set to train the PLS model. This process was iterated ten times, ensuring that every data point was included in the validation set once and only once (Fig. 3e,f). Considering that m μ SORS measures the spectra of the skin, where the glucose level is reported to have a time

lag (Δt) from the VPG^{44,45}, backtracked VPG concentrations were used as the reference for the PLS model (Extended Data Fig. 10).

PLS modelling and independent test

In the expanded BESHs, the PLS model was also tested with independent training and test sets (Fig. 4). Overall, 175 individuals with T2D (D001–D175) and 25 individuals without diabetes (N001–N025) were selected as the training set, while the rest (D176–D200 and N026–N030) were used as the test set (Fig. 4a). As before, μ SORS spectra between 320 cm^{-1} and 2,000 cm^{-1} from offsets 2 and 3 were concatenated into a single vector as the input to the PLS model. Backtracked VPG concentrations with a time lag (Δt) were used as the reference for the PLS model (Extended Data Fig. 10 and ‘Calculation of backtracked VPG concentration’). The optimal number of PLS factors was selected using the subject-wise tenfold cross-validation within the training set. This number of factors was then used to fit the model on the whole training set. Box plot was used to display the overall trend of predicted and reference glucose concentration (Fig. 4d). In the box plot, box boundaries indicate Q1 (25th percentile) and Q3 (75th percentile), whiskers indicate $Q1 - 1.5 \times \text{interquartile range (IQR)}$ and $Q3 + 1.5 \times \text{IQR}$, and the central line indicates the median.

Performance evaluation of PLS model for glucose prediction

The performance of a glucose prediction model was evaluated by the coefficient of determination (R^2), the MARD as well as the CEG-related metrics (CEG A and CEG A + B). A better model corresponds to a higher R^2 , a lower MARD and higher CEG A and CEG A + B.

The metrics of R^2 and MARD can be expressed as:

$$R^2 = 1 - \frac{\sum_{i=1}^N (y_i - \hat{y}_i)^2}{\sum_{i=1}^N (y_i - \bar{y})^2},$$

and

$$\text{MARD} = \frac{1}{N} \sum_{i=1}^N \left| \frac{\hat{y}_i - y_i}{y_i} \right|,$$

where N is the total number of VPG–spectra pairs in the test set, indexed by i , y_i and \hat{y}_i are the reference and the predicted glucose concentration of the i th VPG–spectra pair, respectively. \bar{y} is the mean of all the y_i .

Calculation of backtracked VPG concentrations

Backtracked VPGs were calculated with polynomial fit (order adjusted manually between 3 and 7) of the OGTT measurements for each participant. Assuming that the Δt was the same for all the individuals, we varied its value from 0 min to –25 min with a step size of 1 min to find the optimum, with which the minimal root mean square error (r.m.s.e.) between the backtracked VPGs and the predictions was achieved. The r.m.s.e. was defined as

$$\text{r.m.s.e.} = \sqrt{\frac{\sum_{i=1}^N (\hat{y}_i - y_i)^2}{N}},$$

where N denotes the number of data points (VPG–spectra pairs, indexed by i), y_i and \hat{y}_i are the backtracked and predicted VPG concentrations. Among all the offsets, the minimal r.m.s.e. was achieved by offset 3 with a time lag of –16 min in the preliminary BESH and –13 min in the expanded BESHs (Extended Data Fig. 10). Backtracked VPG concentrations were used in PLS model training and validation instead of the original measurements.

Reporting summary

Further information on research design is available in the Nature Portfolio Reporting Summary linked to this article.

Data availability

The data supporting the findings of this study are available from the corresponding authors upon reasonable request. Source data are provided with this paper.

Code availability

Custom Python code has been applied for data analysis in this work. The code necessary for reanalysing the data presented in this paper is available in Zenodo at <https://doi.org/10.5281/zenodo.14605629> (ref. 46).

References

1. IDF Diabetes Atlas 10th edition (International Diabetes Federation, accessed 22 January 2025); <https://diabetesatlas.org/atlas/tenth-edition/>
2. Brownlee, M. Biochemistry and molecular cell biology of diabetic complications. *Nature* **414**, 813–820 (2001).
3. Guy, R. H. A sweeter life for diabetics? *Nat. Med.* **1**, 1132–1133 (1995).
4. Heinemann, L. Finger pricking and pain: a never ending story. *J. Diabetes Sci. Technol.* **2**, 919–921 (2008).
5. Fruhstorfer, H. & Lange, H. Capillary blood sampling: how much pain is necessary? Part 3: pricking the finger can be less painful. *Pract. Diabetes. Int.* **12**, 253–254 (1995).
6. Lin, R., Brown, F., James, S., Jones, J. & Ekinci, E. Continuous glucose monitoring: a review of the evidence in type 1 and 2 diabetes mellitus. *Diabet. Med.* **38**, e14528 (2021).
7. Xie, X. et al. Reduction of measurement noise in a continuous glucose monitor by coating the sensor with a zwitterionic polymer. *Nat. Biomed. Eng.* **2**, 894–906 (2018).
8. Gao, W. et al. Fully integrated wearable sensor arrays for multiplexed in situ perspiration analysis. *Nature* **529**, 509–514 (2016).
9. Villena Gonzales, W., Mobashsher, A. & Abbosh, A. The progress of glucose monitoring—a review of invasive to minimally and non-invasive techniques, devices and sensors. *Sensors* **19**, 800 (2019).
10. So, C.-F., Choi, K.-S., Wong, T. K. & Chung, J. W. Recent advances in noninvasive glucose monitoring. *Med. Devices* **5**, 45–52 (2012).
11. Lin, T. et al. Non-invasive glucose monitoring: a review of challenges and recent advances. *Sensors* **20**, 6925 (2017).
12. Rao, G. et al. Reverse iontophoresis: noninvasive glucose monitoring in vivo in humans. *Pharm. Res.* **12**, 1869–1873 (1995).
13. Martín-Mateos, P. et al. In-vivo, non-invasive detection of hyperglycemic states in animal models using mm-wave spectroscopy. *Sci. Rep.* **6**, 34035 (2016).
14. Sim, J. Y., Ahn, C. G., Jeong, E. J. & Kim, B. K. In vivo microscopic photoacoustic spectroscopy for non-invasive glucose monitoring invulnerable to skin secretion products. *Sci. Rep.* **8**, 1059 (2018).
15. Uluç, N. et al. Non-invasive measurements of blood glucose levels by time-gating mid-infrared optoacoustic signals. *Nat. Metab.* **6**, 678–686 (2024).
16. Maruo, K. et al. In vivo noninvasive measurement of blood glucose by near-infrared diffuse-reflectance spectroscopy. *Appl. Spectrosc.* **57**, 1236–1244 (2003).
17. Enejder, A. M. K. et al. Raman spectroscopy for noninvasive glucose measurements. *J. Biomed. Opt.* **10**, 031114 (2005).
18. Pleus, S. et al. Proof of concept for a new Raman-based prototype for noninvasive glucose monitoring. *J. Diabetes Sci. Technol.* **15**, 11–18 (2020).
19. Pors, A. et al. Accurate post-calibration predictions for noninvasive glucose measurements in people using confocal Raman spectroscopy. *ACS Sens.* **8**, 1272–1279 (2023).
20. Zhang, L. et al. Spectral tracing of deuterium for imaging glucose metabolism. *Nat. Biomed. Eng.* **3**, 402–413 (2019).
21. Kang, J. W. et al. Direct observation of glucose fingerprint using in vivo Raman spectroscopy. *Sci. Adv.* **6**, 5206–5230 (2020).

22. Matousek, P. et al. Subsurface probing in diffusely scattering media using spatially offset Raman spectroscopy. *Appl. Spectrosc.* **59**, 393–400 (2005).
23. Aleemardani, M., Trikić, M. Z., Green, N. H. & Claeysens, F. The importance of mimicking dermal–epidermal junction for skin tissue engineering: a review. *Bioengineering* **8**, 148 (2021).
24. Wold, S., Sjöström, M. & Eriksson, L. PLS-regression: a basic tool of chemometrics. *Chemom. Intell. Lab. Syst.* **58**, 109–130 (2001).
25. Jendrike, N., Baumstark, A., Kamecke, U., Haug, C. & Freckmann, G. ISO 15197: 2013 evaluation of a blood glucose monitoring system's measurement accuracy. *J. Diabetes Sci. Technol.* **11**, 1275–1276 (2017).
26. Mosca, S., Conti, C., Stone, N. & Matousek, P. Spatially offset Raman spectroscopy. *Nat. Rev. Methods Primers* **1**, 21 (2021).
27. Eliasson, C., Macleod, N. A. & Matousek, P. Noninvasive detection of concealed liquid explosives using Raman spectroscopy. *Anal. Chem.* **79**, 8185–8189 (2007).
28. Conti, C. et al. Advances in Raman spectroscopy for the non-destructive subsurface analysis of artworks: Micro-SORS. *J. Cult. Herit.* **43**, 319–328 (2020).
29. Ghita, A., Matousek, P. & Stone, N. High sensitivity non-invasive detection of calcifications deep inside biological tissue using transmission Raman spectroscopy. *J. Biophotonics* **11**, jbio.201600260 (2018).
30. Matousek, P. & Parker, A. W. Bulk Raman analysis of pharmaceutical tablets. *Appl. Spectrosc.* **60**, 1353–1357 (2006).
31. Vardaki, M. Z. & Kourkoumelis, N. Tissue phantoms for biomedical applications in Raman spectroscopy: a review. *Biomed. Eng. Comput. Biol.* **11**, 1179597220948100 (2020).
32. Braverman, I. M. The cutaneous microcirculation. *J. Investig. Dermatol. Symp. Proc.* **5**, 3–9 (2000).
33. Liu, Z. et al. Circulation and long-term fate of functionalized, biocompatible single-walled carbon nanotubes in mice probed by Raman spectroscopy. *Proc. Natl Acad. Sci. USA* **105**, 1410–1415 (2008).
34. Darvin, M. E. et al. Confocal Raman microscopy combined with optical clearing for identification of inks in multicolored tattooed skin in vivo. *Analyst* **143**, 4990–4999 (2018).
35. Stone, N., Kendall, C., Shepherd, N., Crow, P. & Barr, H. Near-infrared Raman spectroscopy for the classification of epithelial pre-cancers and cancers. *J. Raman Spectrosc.* **33**, 564–573 (2002).
36. Hastie, T., Tibshirani, R., Friedman, J. H. & Friedman, J. H. *The Elements of Statistical Learning: Data Mining, Inference, and Prediction* (Springer, 2009).
37. Leonardo, D. A. M., Luciana, P. A., Fabricio, C. S. G. & Fernando, G. Distinct metabolic profile according to the shape of the oral glucose tolerance test curve is related to whole glucose excursion: a cross-sectional study. *BMC Endocr. Disord.* **18**, 56 (2018).
38. Di, Z. et al. Spatially offset Raman microspectroscopy of highly scattering tissue: theory and experiment. *J. Mod. Opt.* **62**, 97–101 (2015).
39. Luo, R., Popp, J. & Bocklitz, T. Deep learning for Raman spectroscopy: a review. *Analytica* **3**, 287–301 (2022).
40. Soleimaninejad, H., Matroodi, F. & Tavassoli, S. H. Raman spectroscopy of Iranian region calcite using pulsed laser: an approach of fluorescence suppression by time-gating method. *J. Spectrosc.* **2013**, 254964 (2013).
41. Van Dorpe, P. et al. High optical throughput, high spectral resolution, on-chip Raman spectrometer. In *Proc. 26th International Conference on Raman Spectroscopy (ICORS 2018)* 03-1079 (ICORS, 2018).
42. Lintzeri, D. A., Karimian, N., Blume-Peytavi, U. & Kottner, J. Epidermal thickness in healthy humans: a systematic review and meta-analysis. *J. Eur. Acad. Dermatol. Venereol.* **36**, 1191–1200 (2022).
43. Pankrushina, E. A., Kobuzov, A. S., Shchapova, Y. V. & Votyakov, S. L. Analysis of temperature-dependent Raman spectra of minerals: statistical approaches. *J. Raman Spectrosc.* **51**, 1549–1562 (2020).
44. Schmelzeisen-Redeker, G. et al. Time delay of CGM sensors: relevance, causes, and countermeasures. *J. Diabetes Sci. Technol.* **9**, 1006–1015 (2015).
45. Basu, A. et al. Time lag of glucose from intravascular to interstitial compartment in humans. *Diabetes* **62**, 4083–4087 (2013).
46. Shao, S. Subcutaneous depth-selective spectral imaging with μSORS enables non-invasive glucose monitoring. *Zenodo* <https://doi.org/10.5281/zenodo.14605629> (2025).
47. Zakharov, P., Dewarrat, F., Caduff, A. & Talary, M. S. The effect of blood content on the optical and dielectric skin properties. *Physiol. Meas.* **32**, 131–149 (2011).

Acknowledgements

We thank the field workers at Ruijin Hospital and the engineers at Shanghai Photonic View Technology Co., Ltd. for their contribution and the participants for their cooperation in the BESH. The funding by the Noncommunicable Chronic Diseases-National Science and Technology Major Project (2023ZD0508100, Y.Z.), Shanghai Shen-Kang projects (SHDC12024109, L. Zhang and SHDC22022301, W.W.), the Leader Project of the Oriental Talent Program in 2022 (no. 153, Y.Z.), Shanghai Pujiang Program (23PJ059, S.S.), Guangci Innovative Technology Program (KY2023810, C.C.), Guangci Talent Program (RC20240018, C.C.) and Guangci Deep Mind Project of Ruijin Hospital-Shanghai Jiao Tong University School of Medicine are gratefully acknowledged.

Author contributions

Y.Z., L. Zhou, G.N., C.C. and W. W. conceived the study and supervised the experiments. C.H., X.Z., M.S. and C.C. built the optical system. L.W., Y.Z., B.T. and J.S. took charge of the recruitment of subjects. L. Zhang, L.W., B.T., Y.C. and H.C. performed the experiments. M.C. collected the OCT data. S.S., Y.S., S.P., C.J., L. Zhou and C.C. performed data analysis. Y.Z., L. Zhang, L.W., S.S., L. Zhou and C.C. wrote the paper. G.N., C.C. and W.W. obtained the funding.

Competing interests

The μSORS technology presented in this paper is the subject of patents (CN115137298B, CN115120233B and CN214252020U) by Shanghai Photonic View Technology Co., Ltd. C.C. is a shareholder of Shanghai Photonic View Technology Co., Ltd. and the inventor of the patents. The other authors declare no competing interests.

Additional information

Extended data is available for this paper at <https://doi.org/10.1038/s42255-025-01217-w>.

Supplementary information The online version contains supplementary material available at <https://doi.org/10.1038/s42255-025-01217-w>.

Correspondence and requests for materials should be addressed to Lin Zhou, Guang Ning, Chang Chen or Weiqing Wang.

Peer review information *Nature Metabolism* thanks Andreas Birkenfeld, Ioan Notingher, Eric Renard and the other, anonymous, reviewer(s) for their contribution to the peer review of this work. Primary Handling Editor: Christoph Schmitt, in collaboration with the *Nature Metabolism* team.

Reprints and permissions information is available at www.nature.com/reprints.

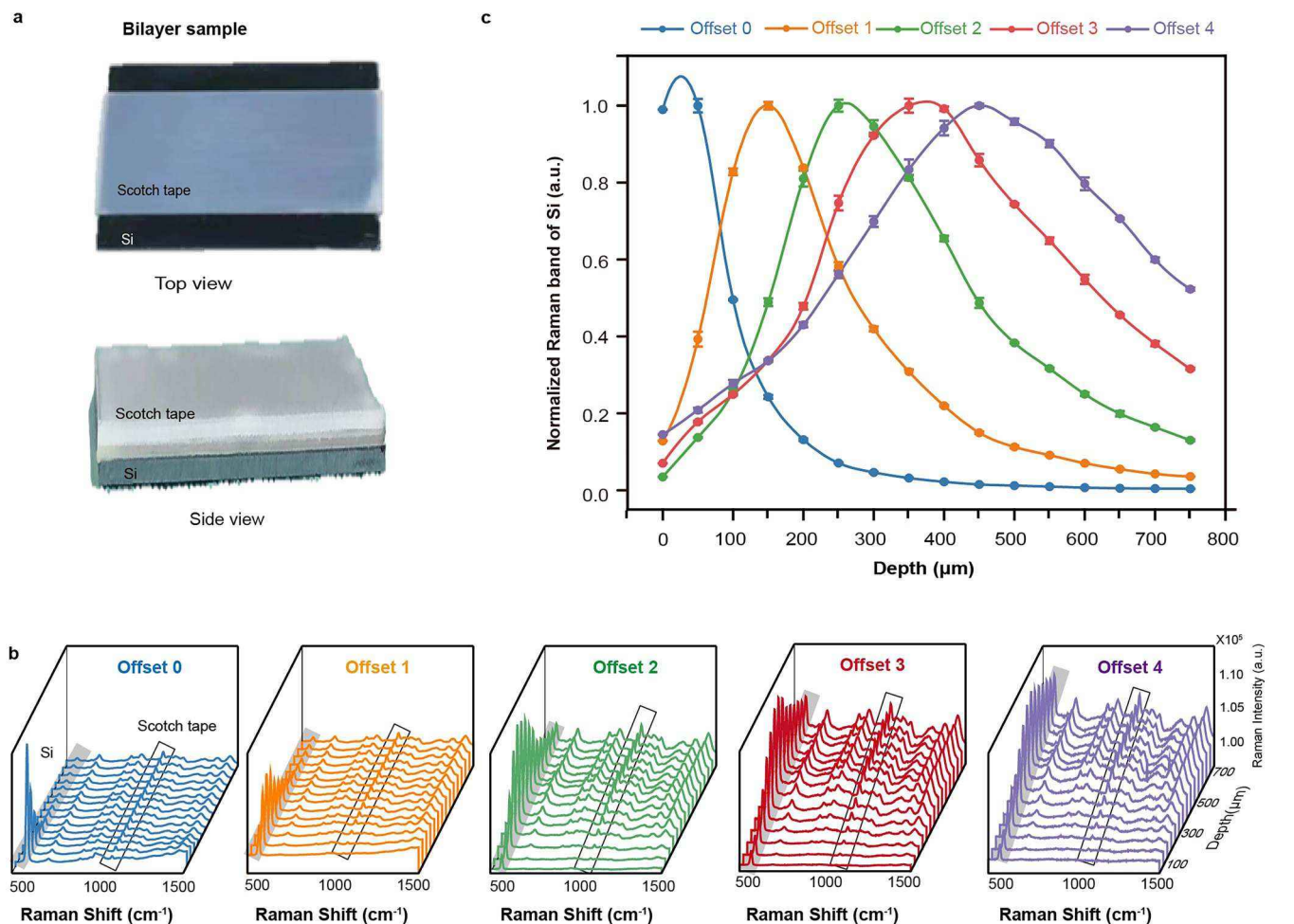
Publisher's note Springer Nature remains neutral with regard to jurisdictional claims in published maps and institutional affiliations.

Springer Nature or its licensor (e.g. a society or other partner) holds exclusive rights to this article under a publishing agreement with

the author(s) or other rightsholder(s); author self-archiving of the accepted manuscript version of this article is solely governed by the terms of such publishing agreement and applicable law.

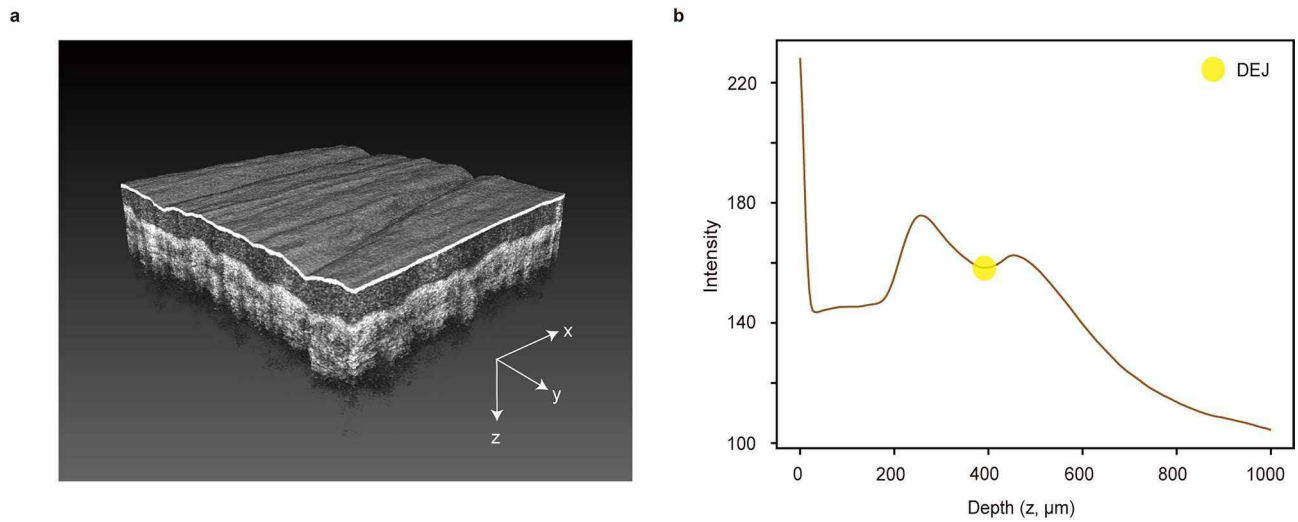
© The Author(s), under exclusive licence to Springer Nature Limited 2025

¹Department of Endocrine and Metabolic Diseases, Shanghai Institute of Endocrine and Metabolic Diseases, Ruijin Hospital, Shanghai Jiao Tong University School of Medicine, Shanghai, China. ²Shanghai National Clinical Research Center for Metabolic Diseases, Key Laboratory for Endocrine and Metabolic Diseases of the National Health Commission, Shanghai National Center for Translational Medicine, Ruijin Hospital, Shanghai Jiao Tong University School of Medicine, Shanghai, China. ³Shanghai Photonic View Technology Co., Ltd, Shanghai, China. ⁴Department of Dermatology, Ruijin Hospital, Shanghai Jiao Tong University School of Medicine, Shanghai, China. ⁵Shanghai Institute for Interventional Medical Devices, School of Health Science and Engineering, University of Shanghai for Science and Technology, Shanghai, China. ⁶State Key Laboratory of Transducer Technology, Shanghai Institute of Microsystem and Information Technology, Chinese Academy of Sciences, Shanghai, China. ⁷Institute of Medical Chip, Ruijin Hospital, Shanghai Jiao Tong University School of Medicine, Shanghai, China. ⁸These authors contributed equally: Yifei Zhang, Lili Zhang, Long Wang, Shuai Shao. ✉e-mail: lin.zhou@photonview.com; gning@sibs.ac.cn; changchen@sjtu.edu.cn; wqingw@shsmu.edu.cn

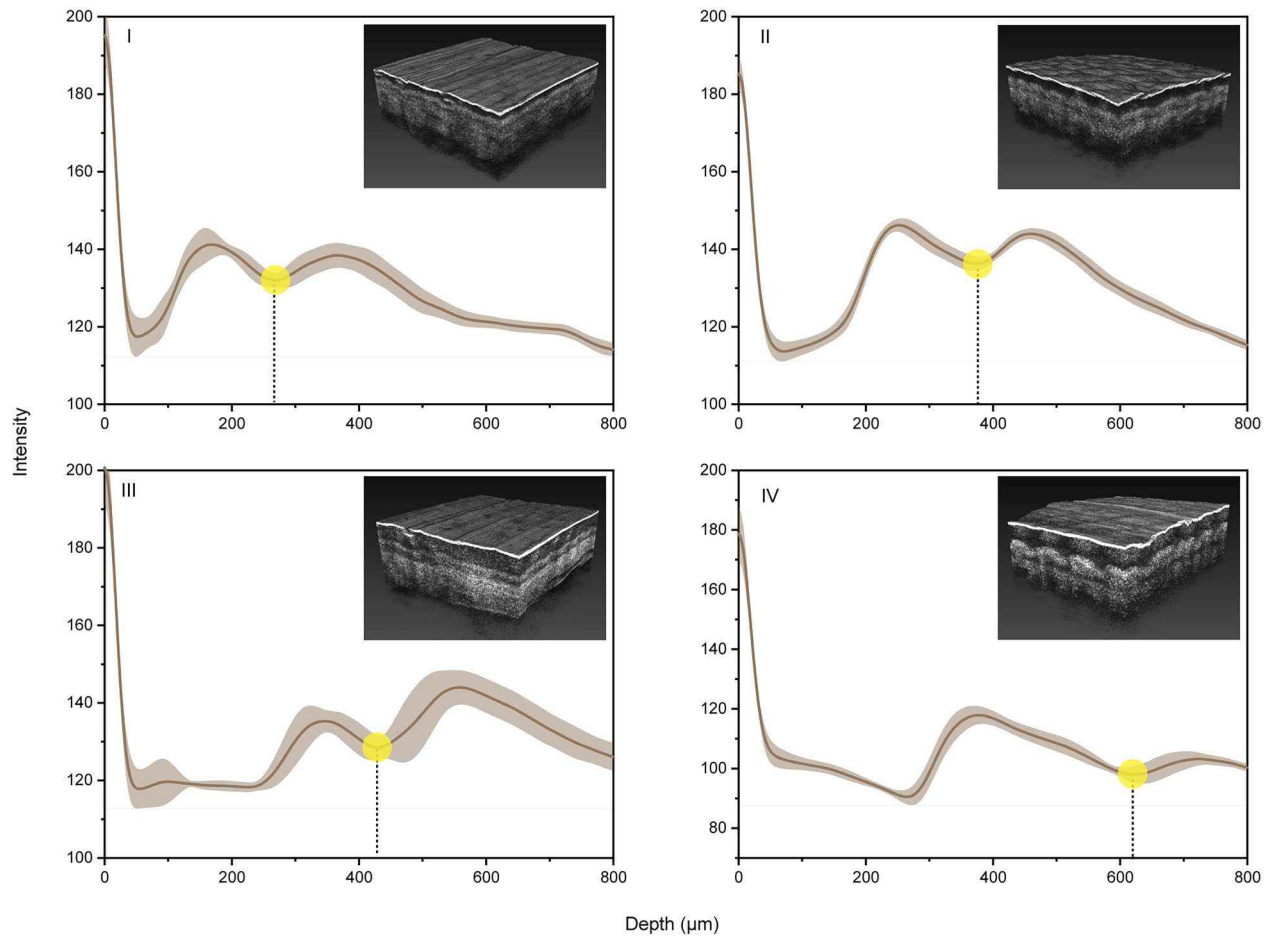


Extended Data Fig. 1 | Bilayer sample characterizes depth selectivity of $m\mu\text{SORS}$. **a**, Top view and side view of the Si-tape bilayer sample. **b**, Raman spectra of the bilayer sample displayed in three dimensions. Shade and box indicate characteristic Raman peaks at 520 cm^{-1} (Si) and 1041 cm^{-1} (Scotch tape), respectively. The depth of Si in 15 different phantoms increased from

$50\text{ }\mu\text{m}$ to $750\text{ }\mu\text{m}$ with a step of $50\text{ }\mu\text{m}$. **c**, Normalized Si (520 cm^{-1}) Raman band intensity varying with its depth for each offset. Error bars indicate mean and standard deviation (SD) over $n = 3$ measurements. Lines are derived from 9-order polynomial fitting of the measured points.

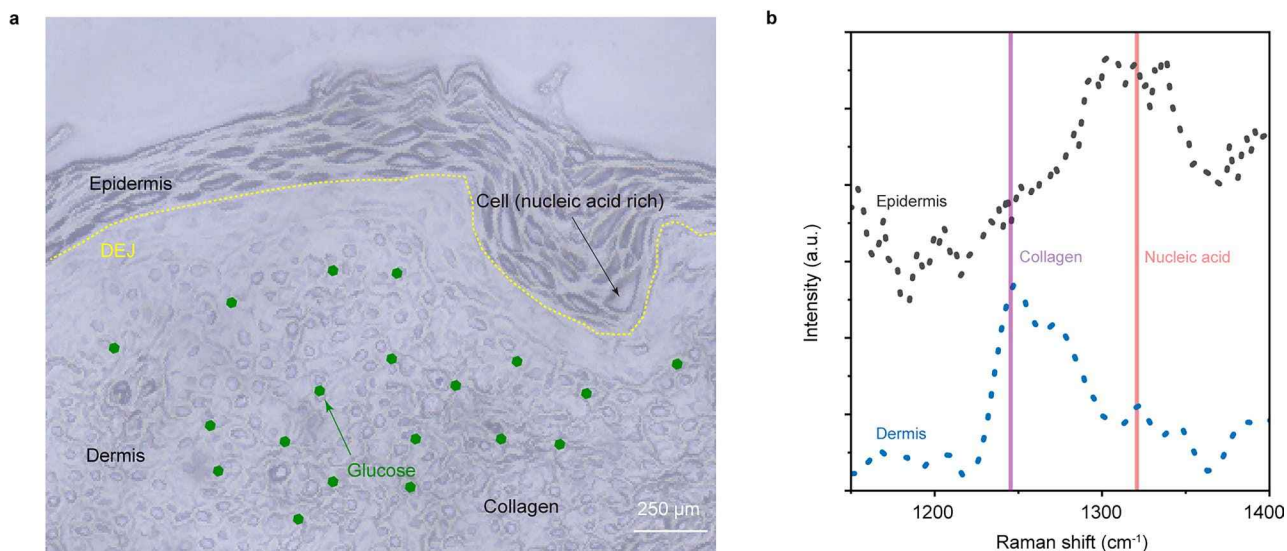


Extended Data Fig. 2 | Acquisition and analysis of OCT scans. a, The 3D image acquired by OCT (the left hand of D132 as an example). **b,** The intensity profile along the z (depth) dimension of Subject D132's left hand (same as a). z = 0 corresponds to the skin surface. Yellow dot indicates the characteristic points that were manually annotated and corresponded to the DEJ depth.



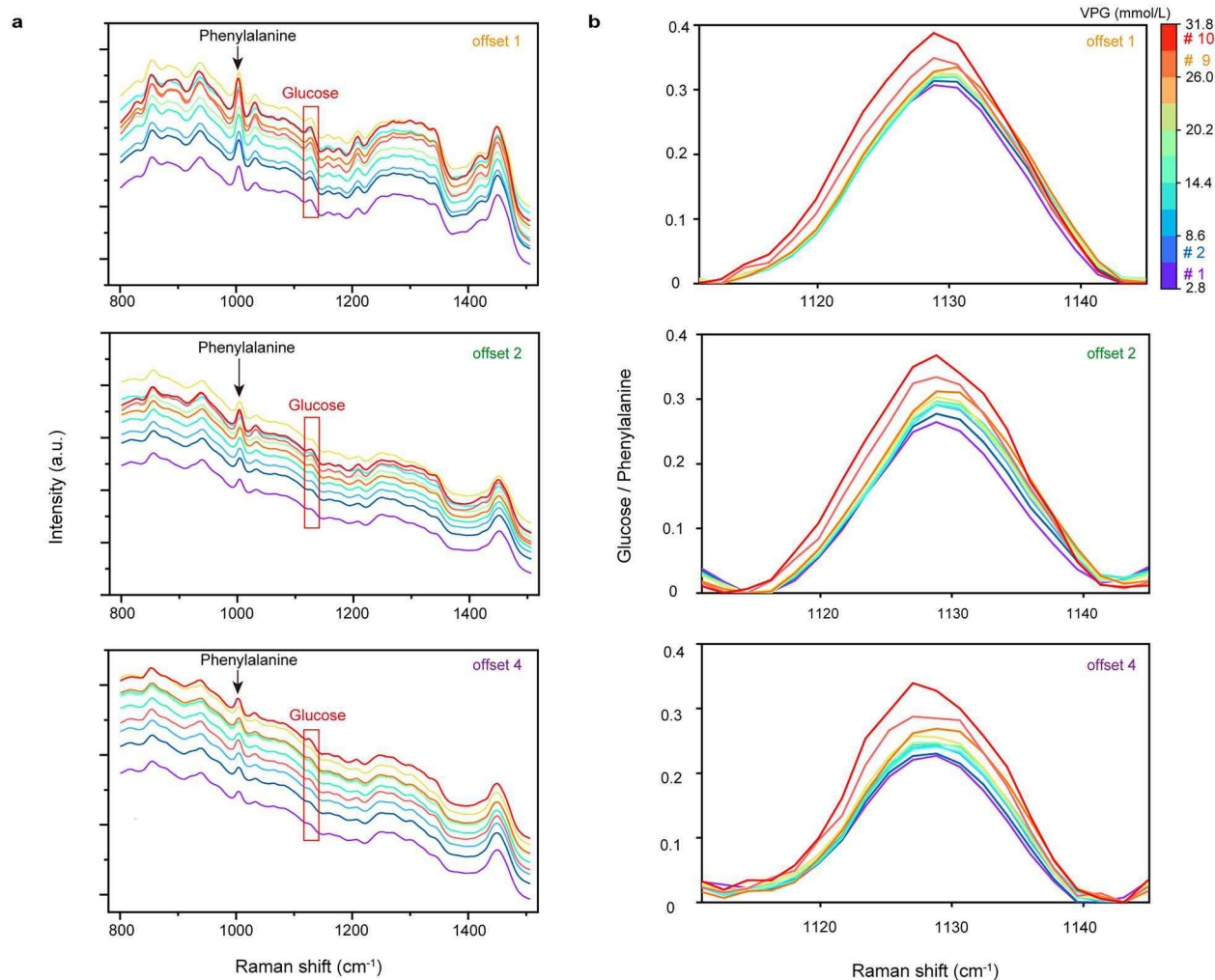
Extended Data Fig. 3 | Intensity profiles of four typical thenar OCT images. I–IV marked samples from a single hand of four typical subjects. The shades indicate the standard deviation (see **Methods**). Yellow dots indicate the characteristic

points that were manually annotated and corresponded to the DEJ depth. Insets: three-dimensional OCT images constructed from a volume of 3 mm (x) * 3 mm (y) * 1.95 mm (z).



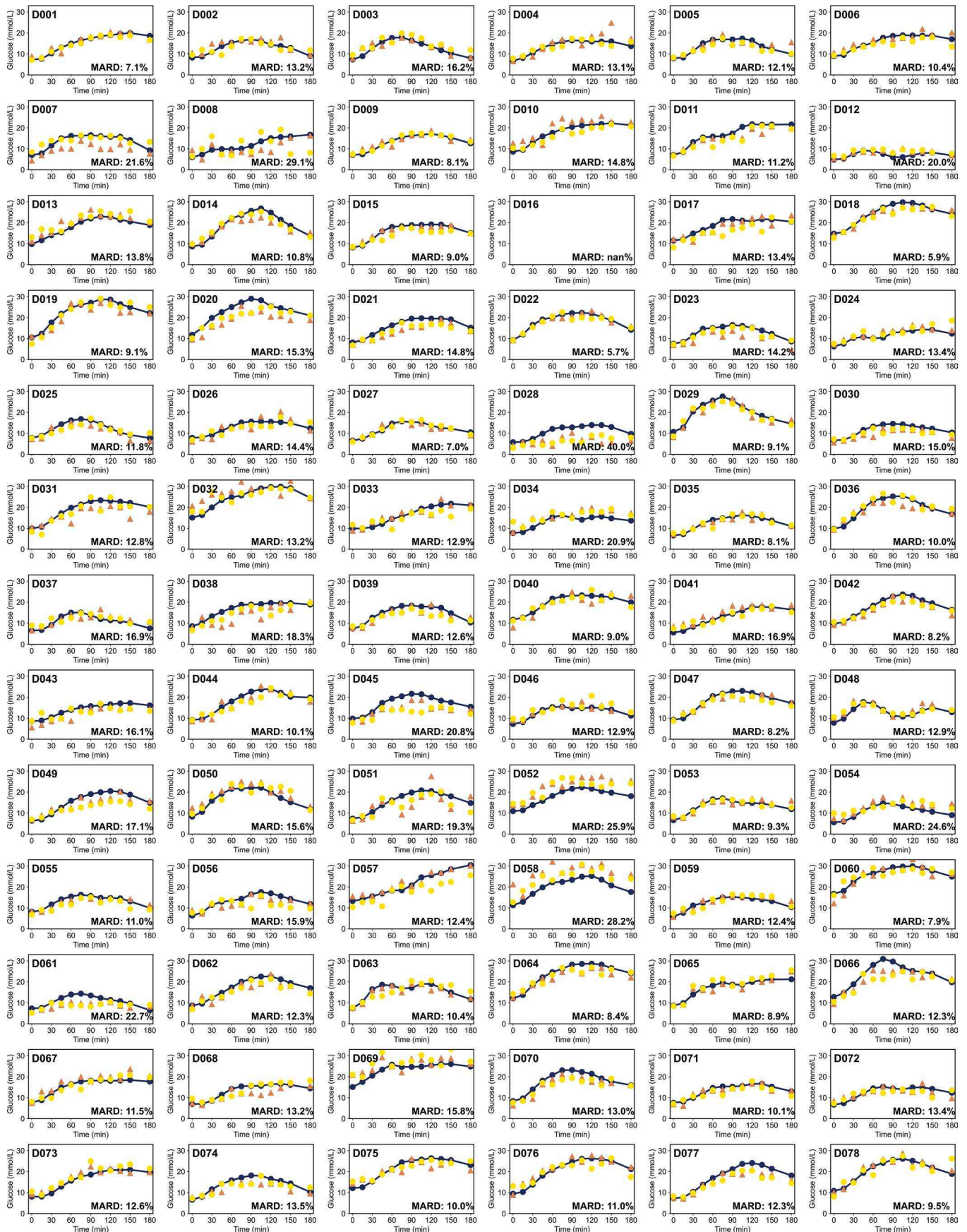
Extended Data Fig. 4 | Anatomical and spectral characterization of epidermis and dermis of human skin samples. **a**, Bright field image of a processed *ex-vivo* human skin cross-section. A forearm cross-section from one woman of 29 years old were imaged and repeated independently five times with similar results, the zoom-in region of interest was shown. Epidermis is rich in cells, and thus, nucleic acid, while dermis is rich in collagen. The yellow dashed curve indicates the DEJ. Green dots indicate the distribution of glucose molecules, predominantly within

the dermis. Scale bar: 250 μm . **b**, Reference Raman spectra taken from *ex-vivo* epidermis (black) and dermis (blue) samples of human skin. An *ex-vivo* fresh upper back tissue from one man of 28 years old was obtained and cut manually to prepare epidermal and dermal samples, five spectra were collected from different region of interest for each sample and the mean spectra were shown as reference spectra. Pink and purple shades indicate characteristic Raman peaks of nucleic acid and collagen.



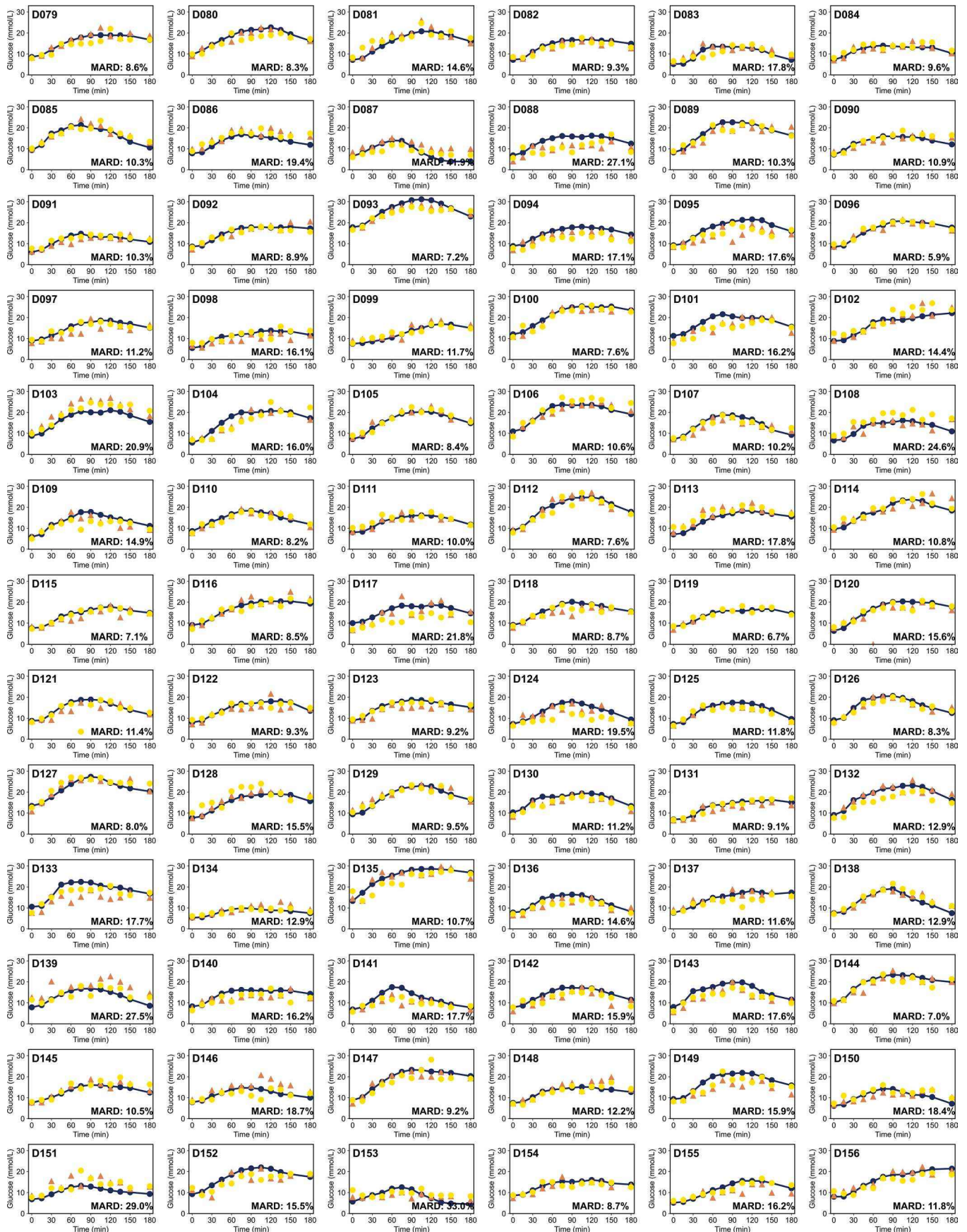
Extended Data Fig. 5 | μ SORS spectra of 10 groups partitioned by equal binning of VPG levels. a, Average spectra in the range of 800–1,500 cm^{-1} for each of the 10 VPG-spectra groups (Fig. 2e) at different offsets in the preliminary BESH of 35 subjects. The black arrow indicates the phenylalanine Raman peak

at 1001 cm^{-1} , while the red box indicates the characteristic glucose Raman peak at 1,125 cm^{-1} . **b**, Normalized Raman spectra (glucose Raman band divided by phenylalanine Raman band) of different offsets averaged over each of the 10 VPG-spectra groups (Fig. 2f), zoomed in around the glucose Raman peak at 1125 cm^{-1} .



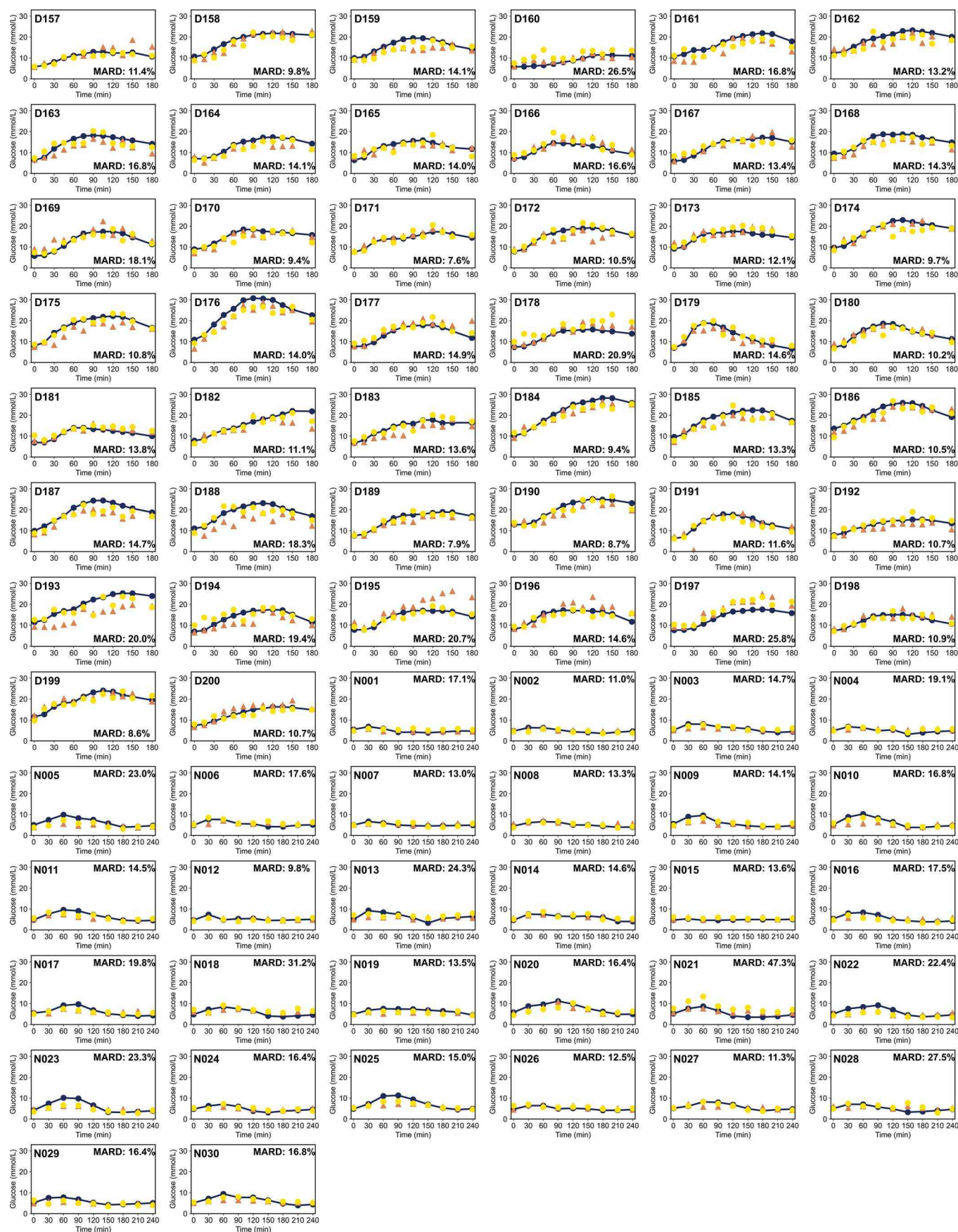
Extended Data Fig. 6 | Blood glucose prediction results for 78 subjects with type 2 diabetes (D001-D078) in all 230 subjects of expanded BESHs. Dark Blue lines: reference concentration (VPG, Fig. 3c). Orange triangles: glucose

concentration predicted from left-hand spectra. Yellow circles: glucose concentration predicted from the right-hand spectra. All predictions were generated using subject-wise tenfold cross-validation (Fig. 3d).



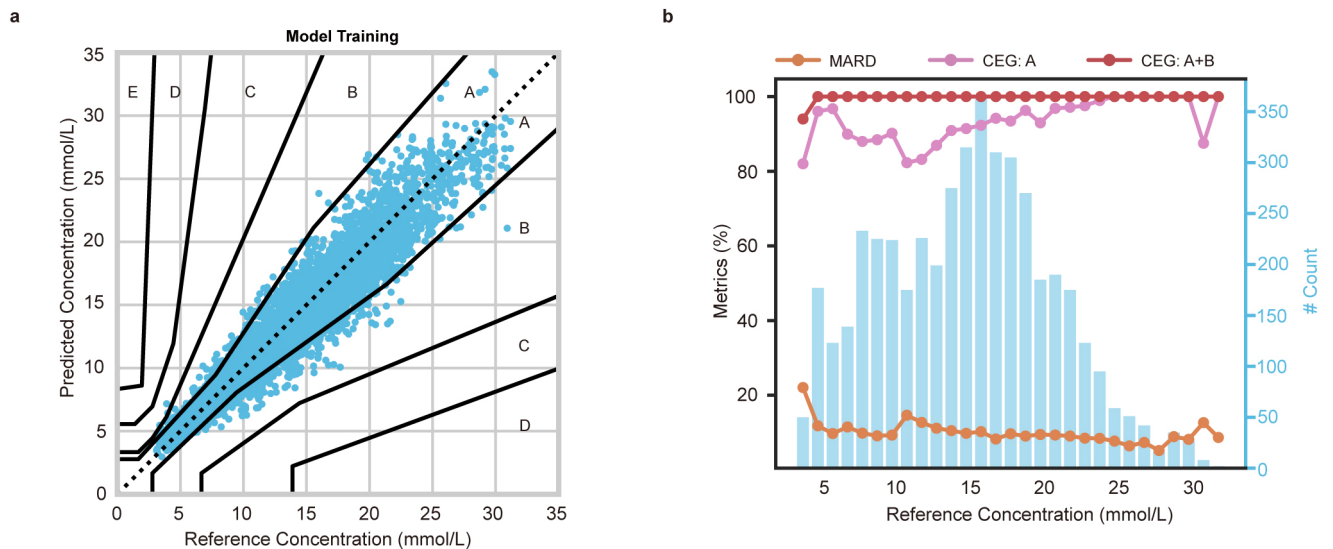
Extended Data Fig. 7 | Blood glucose prediction results for 78 subjects with type 2 diabetes (D079-D156) in all 230 subjects of expanded BESHs. Dark Blue lines: reference concentration (VPG, Fig. 3c). Orange triangles: glucose

concentration predicted from left-hand spectra. Yellow circles: glucose concentration predicted from the right-hand spectra. All predictions were generated using subject-wise tenfold cross-validation (Fig. 3d).



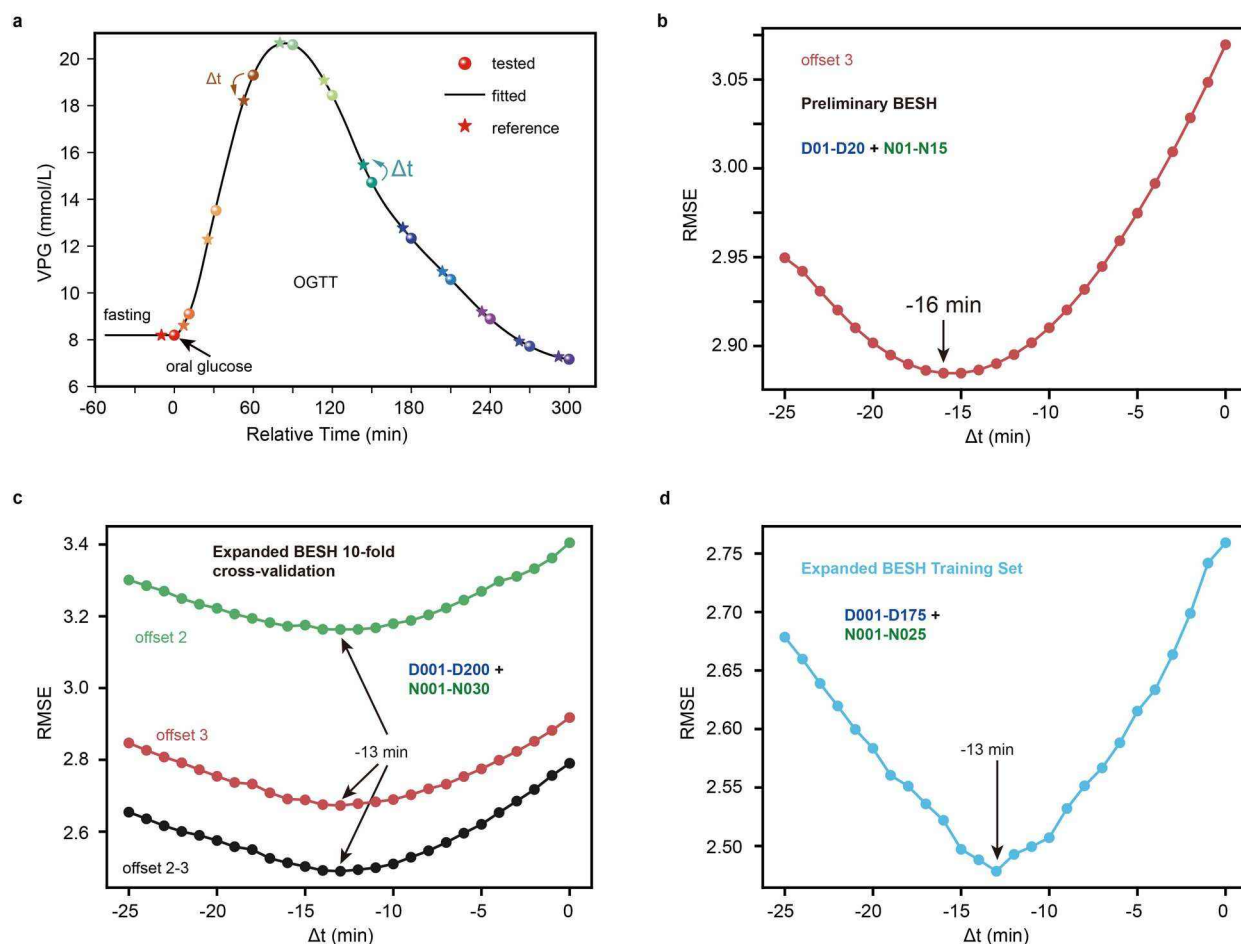
Extended Data Fig. 8 | Blood glucose prediction results for 48 subjects with type 2 diabetes (D157–D200) and 30 subjects without diabetes (N001–N030) in all 230 subjects of expanded BESHs. Dark Blue lines: reference concentration (VPG, Fig. 3c). Orange triangles: glucose concentration predicted from left-hand

spectra. Yellow circles: glucose concentration predicted from the right-hand spectra. All predictions were generated using subject-wise tenfold cross-validation (Fig. 3d).



Extended Data Fig. 9 | PLS model training for independent test. a. Consensus error grid (CEG) of the predictions obtained from the PLS regression model on the training set ($n = 4,618$). **b.** Model performance metrics plotted

against reference glucose concentration in the training set. Orange: MARD. Magenta: CEG: A. Red: CEG: A + B. Cyan shade: histogram of reference glucose concentration (VPG).



Extended Data Fig. 10 | Optimizing the time delay in the PLS model for glucose prediction. **a**, The VPG data of a typical subject with diabetes during the 5-h OGTT in the preliminary BESH. Measured VPGs (dots) were fitted with polynomials and the backtracked VPG with a certain time lag (stars) were used as reference in PLS models. **b**, RMSE between the model predictions and the reference VPGs, varying with the time lag from -25 to 0 min. The optimized time lag was at -16 min. The models were trained and tested with spectra from offset 3 in the preliminary BESH. Model predictions were generated using leave-one-

subject-out cross-validation scheme (Fig. 2h). **c**, Counterpart of **b** for offset 2 and 3 as well as the concatenation (offset 2–3) of these two offsets in the expanded BESHs of 230 subjects. The optimal time lag was at -13 min for both two offsets and the concatenation. Model predictions were generated using subject-wise tenfold cross-validation scheme (Fig. 3d). **d**, Counterpart of the black curve in **c** in the training set comprised of 200 subjects in the expanded BESHs (Fig. 4a). The optimal time lag was at -13 min.

Reporting Summary

Nature Portfolio wishes to improve the reproducibility of the work that we publish. This form provides structure for consistency and transparency in reporting. For further information on Nature Portfolio policies, see our [Editorial Policies](#) and the [Editorial Policy Checklist](#).

Statistics

For all statistical analyses, confirm that the following items are present in the figure legend, table legend, main text, or Methods section.

- | | |
|-------------------------------------|--|
| n/a | Confirmed |
| <input type="checkbox"/> | <input checked="" type="checkbox"/> The exact sample size (n) for each experimental group/condition, given as a discrete number and unit of measurement |
| <input type="checkbox"/> | <input checked="" type="checkbox"/> A statement on whether measurements were taken from distinct samples or whether the same sample was measured repeatedly |
| <input type="checkbox"/> | <input checked="" type="checkbox"/> The statistical test(s) used AND whether they are one- or two-sided
<i>Only common tests should be described solely by name; describe more complex techniques in the Methods section.</i> |
| <input checked="" type="checkbox"/> | <input type="checkbox"/> A description of all covariates tested |
| <input checked="" type="checkbox"/> | <input type="checkbox"/> A description of any assumptions or corrections, such as tests of normality and adjustment for multiple comparisons |
| <input type="checkbox"/> | <input checked="" type="checkbox"/> A full description of the statistical parameters including central tendency (e.g. means) or other basic estimates (e.g. regression coefficient) AND variation (e.g. standard deviation) or associated estimates of uncertainty (e.g. confidence intervals) |
| <input type="checkbox"/> | <input checked="" type="checkbox"/> For null hypothesis testing, the test statistic (e.g. F , t , r) with confidence intervals, effect sizes, degrees of freedom and P value noted
<i>Give P values as exact values whenever suitable.</i> |
| <input checked="" type="checkbox"/> | <input type="checkbox"/> For Bayesian analysis, information on the choice of priors and Markov chain Monte Carlo settings |
| <input checked="" type="checkbox"/> | <input type="checkbox"/> For hierarchical and complex designs, identification of the appropriate level for tests and full reporting of outcomes |
| <input type="checkbox"/> | <input checked="" type="checkbox"/> Estimates of effect sizes (e.g. Cohen's d , Pearson's r), indicating how they were calculated |

Our web collection on [statistics for biologists](#) contains articles on many of the points above.

Software and code

Policy information about [availability of computer code](#)

- | | |
|-----------------|--|
| Data collection | Raman spectra are acquired by μ SORS system developed in this study.
Venous blood glucose (VBG) is measured by an autoanalyzer (AU5800, BECKMAN).
DEJ Depth of human thenar was determined by optical coherence tomography system (Ganymede SD-OCT System, Thorlabs).
Bright field image and Raman spectra of ex-vivo human skin were obtained from WITec alpha 300 imaging system (Germany). |
| Data analysis | Python version 3.9.13 is used with the base packages and the following additional packages: numpy (1.21.5), matplotlib (3.5.2), scipy (1.9.1), pandas (1.4.4), and seaborn (0.11.2). A standard PLS algorithm is used to build the regression models. The analysis codes used in the current study are available upon reasonable request addressed to the corresponding authors |

For manuscripts utilizing custom algorithms or software that are central to the research but not yet described in published literature, software must be made available to editors and reviewers. We strongly encourage code deposition in a community repository (e.g. GitHub). See the Nature Portfolio [guidelines for submitting code & software](#) for further information.

Data

Policy information about [availability of data](#)

All manuscripts must include a [data availability statement](#). This statement should provide the following information, where applicable:

- Accession codes, unique identifiers, or web links for publicly available datasets
- A description of any restrictions on data availability
- For clinical datasets or third party data, please ensure that the statement adheres to our [policy](#)

Data and code showed in figures can be found with the link: <https://doi.org/10.6084/m9.figshare.25750602>. All data used in the current study are available upon reasonable request addressed to the corresponding authors

Research involving human participants, their data, or biological material

Policy information about studies with [human participants or human data](#). See also policy information about [sex, gender \(identity/presentation\), and sexual orientation](#) and [race, ethnicity and racism](#).

Reporting on sex and gender

In all basic experimental studies with humans (BESHs), the sex of the participants was reported as a number and percentage of the total number of participants. Sex or birth gender of participants was determined based on self-report and government-issued personal Identity Card (ID). We performed sex-based analyses and showed no significant difference in accuracy between female and male subjects.

Reporting on race, ethnicity, or other socially relevant groupings

All participants in the study were Chinese.

Population characteristics

In the preliminary BESH (No. NCT05504005): 1) Male or female, healthy or previously diagnosed type 2 diabetes. 2) Aged between 30 and 60 years. 3) For healthy subjects without diabetes history, fasting blood glucose (FPG) < 6.1 mmol/L and glycated hemoglobin (HbA1c) < 5.7% during the screening period and for patients with type 2 diabetes, FBG \geq 6.1 and < 13.3 mmol/L. 4) There are no scars, obvious pigmentation and other factors that interfere with the detection of the palm skin to be tested.

In the expanded BESH (No. NCT05921344): 1) Male or female, previously diagnosed type 2 diabetes. 2) Aged larger than or equal to 18 years old. 3) There are no scars, obvious pigmentation and other factors that interfere with the detection of the palm skin to be tested.

In the expanded BESH (No. NCT06512077): 1) Male or female, without diabetes history. 2) Aged larger than or equal to 18 years old. 3) Fasting blood glucose (FPG) < 6.1 mmol/L and glycated hemoglobin (HbA1c) < 5.7% during the screening period. 4) There are no scars, obvious pigmentation and other factors that interfere with the detection of the palm skin to be tested.

Recruitment

All BESHs were open, participants were recruited from Ruijin hospital. For the enrollment of T2D subjects, it is required that no acute complications of diabetes within 3 months before enrollment, or severe chronic complications of diabetes and comorbidities (including severe structural heart disease, chronic congestive heart failure (NYHA \geq III), and history of severe liver or kidney dysfunction, etc) were observed.

Ethics oversight

All ethics approvals were obtained from the RuiJin Hospital Ethics Committee, affiliated with Shanghai JiaoTong University School of Medicine. All the subjects have provided written informed consent and were compensated for the travel reimbursement and sampling.

Note that full information on the approval of the study protocol must also be provided in the manuscript.

Field-specific reporting

Please select the one below that is the best fit for your research. If you are not sure, read the appropriate sections before making your selection.

Life sciences Behavioural & social sciences Ecological, evolutionary & environmental sciences

For a reference copy of the document with all sections, see nature.com/documents/nr-reporting-summary-flat.pdf

Life sciences study design

All studies must disclose on these points even when the disclosure is negative.

Sample size

35 participants in the preliminary BESH (No. NCT05504005).
200 participants in the expanded BESH (No. NCT05921344).
30 participants in the expanded BESH (No. NCT06512077).
No sample-size calculations were performed. Sample sizes were chosen based on similar previously published studies of non-invasive glucose blood monitoring (Stefan Pleus et al. J Diabetes Sci Technol. 15,11-18 (2020) & Anders Pors et al. ACS Sens. 2024 <https://doi.org/10.1021/acssensors.2c02756>). The numbers of samples are large enough to capture normal variation and glucose feature from Raman spectra according to the published data in this field.

Data exclusions

In the preliminary BESH (No. NCT05504005): Among all 420 sets of data, 5 spectra are lost due to technical issues.

Data exclusions	In the expanded BESH (No.NCT05921344): Among all 4800 sets of data, 24 from both hands of subject D016 were lost because the subject quit the BESH. 8 sampling points of subject D119 were lost due to technical problems. In the expanded BESH (No.NCT06512077): Among all 540 sets of data, no data lost.
Replication	We have demonstrated the replication with three independent BESHs.
Randomization	N/A - No randomization was used in this study, and all enrolled subjects were treated the same.
Blinding	N/A - Blinding was not necessary since there was no randomization nor experimental groups.

Reporting for specific materials, systems and methods

We require information from authors about some types of materials, experimental systems and methods used in many studies. Here, indicate whether each material, system or method listed is relevant to your study. If you are not sure if a list item applies to your research, read the appropriate section before selecting a response.

Materials & experimental systems

n/a	Involvement
<input checked="" type="checkbox"/>	<input type="checkbox"/> Antibodies
<input checked="" type="checkbox"/>	<input type="checkbox"/> Eukaryotic cell lines
<input checked="" type="checkbox"/>	<input type="checkbox"/> Palaeontology and archaeology
<input checked="" type="checkbox"/>	<input type="checkbox"/> Animals and other organisms
<input type="checkbox"/>	<input checked="" type="checkbox"/> Clinical data
<input checked="" type="checkbox"/>	<input type="checkbox"/> Dual use research of concern
<input checked="" type="checkbox"/>	<input type="checkbox"/> Plants

Methods

n/a	Involvement
<input checked="" type="checkbox"/>	<input type="checkbox"/> ChIP-seq
<input checked="" type="checkbox"/>	<input type="checkbox"/> Flow cytometry
<input checked="" type="checkbox"/>	<input type="checkbox"/> MRI-based neuroimaging

Clinical data

Policy information about [clinical studies](#)

All manuscripts should comply with the ICMJE [guidelines for publication of clinical research](#) and a completed [CONSORT checklist](#) must be included with all submissions.

Clinical trial registration	https://clinicaltrials.gov/ , No. NCT05504005, No. NCT05921344 and No.NCT06512077.
Study protocol	https://clinicaltrials.gov/
Data collection	We recruited all the participants, performed the study and collected all the data in Ruijin Hospital affiliated with Shanghai JiaoTong University School of Medicine in Shanghai of China. The data in preliminary BESH (No. NCT05504005) was collected from August to December in 2022. The data in expanded BESH (No. NCT05921344) was collected from July to September in 2023. The data in expanded BESH (No.NCT06512077) was collected in August of 2024.
Outcomes	Primary outcome: 1) Mean absolute relative deviation (MARD) of venous plasma glucose and glucose values measured by μ SORS at each time point of OGTT. 2) Consensus Error Grid (CEG) for venous plasma glucose and glucose values measured by μ SORS at each time point of OGTT. Secondary Outcome: 1) MARD for two measurement methods in different blood glucose ranges. 2) Incidence of treatment-emergent adverse events.

Plants

Seed stocks	N/A.
Novel plant genotypes	N/A.
Authentication	N/A.

Subcutaneous depth-selective spectral imaging with $m\mu$ SORS enables noninvasive glucose monitoring

In the format provided by the authors and unedited

1 **Supplementary Table 1 | Equal binning of 415 data pairs into 10 groups based on**
2 **VPG levels.**

Group Number	VPG range (mmol/L)	Mean VPG (mmol/L)	Number of m μ SORS spectra
#1	2.8 - 5.7	4.6	110
#2	5.7 - 8.6	7.1	96
#3	8.6 - 11.5	9.8	54
#4	11.5 - 14.4	12.9	44
#5	14.4 - 17.3	15.7	30
#6	17.3 - 20.2	18.7	40
#7	20.2 - 23.1	21.4	24
#8	23.1 - 26.0	24.7	12
#9	26.0 - 28.9	26.9	3
#10	28.9 - 31.8	31.1	2

3
4

5 **Supplementary Table 2 | Details about 3 BESHs and data division.**

	Preliminary BESH (n=35)	Expanded BESHs (n=230)	
		Expanded BESH I	Expanded BESH II
Registration number	NCT05504005	NCT05921344	NCT06512077
Subjects	20 with T2D 15 without diabetes	200 with T2D (D)	30 without diabetes (N)
OGTT duration	5 h	3 h	4 h
VPG sampling points	12 points	12 points	9 points
Spectral acquisition	Right hand	Dual hands	Dual hands
PLS cross validation	Leave-one-subject-out (n=35) (Fig. 2h-j)	Subject-wise 10-fold cross validation (n=230) (Fig. 3d-f, Extended Data Fig. 6)	
PLS independent test	N. A.	Training (n=200): 175D + 25N subjects (Fig. 4a, Extended Data Fig. 7) Independent test (n=30): 25D + 5N subjects (Fig. 4, Fig. 5)	

6

Reporting Summary

Nature Portfolio wishes to improve the reproducibility of the work that we publish. This form provides structure for consistency and transparency in reporting. For further information on Nature Portfolio policies, see our [Editorial Policies](#) and the [Editorial Policy Checklist](#).

Statistics

For all statistical analyses, confirm that the following items are present in the figure legend, table legend, main text, or Methods section.

n/a Confirmed

- The exact sample size (n) for each experimental group/condition, given as a discrete number and unit of measurement
- A statement on whether measurements were taken from distinct samples or whether the same sample was measured repeatedly
- The statistical test(s) used AND whether they are one- or two-sided
Only common tests should be described solely by name; describe more complex techniques in the Methods section.
- A description of all covariates tested
- A description of any assumptions or corrections, such as tests of normality and adjustment for multiple comparisons
- A full description of the statistical parameters including central tendency (e.g. means) or other basic estimates (e.g. regression coefficient) AND variation (e.g. standard deviation) or associated estimates of uncertainty (e.g. confidence intervals)
- For null hypothesis testing, the test statistic (e.g. F , t , r) with confidence intervals, effect sizes, degrees of freedom and P value noted
Give P values as exact values whenever suitable.
- For Bayesian analysis, information on the choice of priors and Markov chain Monte Carlo settings
- For hierarchical and complex designs, identification of the appropriate level for tests and full reporting of outcomes
- Estimates of effect sizes (e.g. Cohen's d , Pearson's r), indicating how they were calculated

Our web collection on [statistics for biologists](#) contains articles on many of the points above.

Software and code

Policy information about [availability of computer code](#)

Data collection

Raman spectra are acquired by μ SORS system developed in this study.
Venous blood glucose (VBG) is measured by an autoanalyzer (AU5800, BECKMAN).
DEJ Depth of human thenar was determined by optical coherence tomography system (Ganymede SD-OCT System, Thorlabs).
Bright field image and Raman spectra of ex-vivo human skin were obtained from WITec alpha 300 imaging system (Germany).

Data analysis

Python version 3.9.13 is used with the base packages and the following additional packages: numpy (1.21.5), matplotlib (3.5.2), scipy (1.9.1), pandas (1.4.4), and seaborn (0.11.2). A standard PLS algorithm is used to build the regression models. The analysis codes used in the current study are available upon reasonable request addressed to the corresponding authors

For manuscripts utilizing custom algorithms or software that are central to the research but not yet described in published literature, software must be made available to editors and reviewers. We strongly encourage code deposition in a community repository (e.g. GitHub). See the Nature Portfolio [guidelines for submitting code & software](#) for further information.

Data

Policy information about [availability of data](#)

All manuscripts must include a [data availability statement](#). This statement should provide the following information, where applicable:

- Accession codes, unique identifiers, or web links for publicly available datasets
- A description of any restrictions on data availability
- For clinical datasets or third party data, please ensure that the statement adheres to our [policy](#)

Data and code shown in figures can be found with the link: <https://doi.org/10.6084/m9.figshare.25750602>. All data used in the current study are available upon reasonable request addressed to the corresponding authors

Research involving human participants, their data, or biological material

Policy information about studies with [human participants or human data](#). See also policy information about [sex, gender \(identity/presentation\), and sexual orientation](#) and [race, ethnicity and racism](#).

Reporting on sex and gender

In all basic experimental studies with humans (BESHs), the sex of the participants was reported as a number and percentage of the total number of participants. Sex or birth gender of participants was determined based on self-report and government-issued personal Identity Card (ID). We performed sex-based analyses and showed no significant difference in accuracy between female and male subjects.

Reporting on race, ethnicity, or other socially relevant groupings

All participants in the study were Chinese.

Population characteristics

In the preliminary BESH (No. NCT05504005): 1) Male or female, healthy or previously diagnosed type 2 diabetes. 2) Aged between 30 and 60 years. 3) For healthy subjects without diabetes history, fasting blood glucose (FPG) < 6.1 mmol/L and glycated hemoglobin (HbA1c) < 5.7% during the screening period and for patients with type 2 diabetes, FBG \geq 6.1 and < 13.3 mmol/L. 4) There are no scars, obvious pigmentation and other factors that interfere with the detection of the palm skin to be tested.

In the expanded BESH (No. NCT05921344): 1) Male or female, previously diagnosed type 2 diabetes. 2) Aged larger than or equal to 18 years old. 3) There are no scars, obvious pigmentation and other factors that interfere with the detection of the palm skin to be tested.

In the expanded BESH (No. NCT06512077): 1) Male or female, without diabetes history. 2) Aged larger than or equal to 18 years old. 3) Fasting blood glucose (FPG) < 6.1 mmol/L and glycated hemoglobin (HbA1c) < 5.7% during the screening period. 4) There are no scars, obvious pigmentation and other factors that interfere with the detection of the palm skin to be tested.

Recruitment

All BESHs were open, participants were recruited from Ruijin hospital. For the enrollment of T2D subjects, it is required that no acute complications of diabetes within 3 months before enrollment, or severe chronic complications of diabetes and comorbidities (including severe structural heart disease, chronic congestive heart failure (NYHA \geq III), and history of severe liver or kidney dysfunction, etc) were observed.

Ethics oversight

All ethics approvals were obtained from the RuiJin Hospital Ethics Committee, affiliated with Shanghai JiaoTong University School of Medicine. All the subjects have provided written informed consent and were compensated for the travel reimbursement and sampling.

Note that full information on the approval of the study protocol must also be provided in the manuscript.

Field-specific reporting

Please select the one below that is the best fit for your research. If you are not sure, read the appropriate sections before making your selection.

Life sciences Behavioural & social sciences Ecological, evolutionary & environmental sciences

For a reference copy of the document with all sections, see nature.com/documents/nr-reporting-summary-flat.pdf

Life sciences study design

All studies must disclose on these points even when the disclosure is negative.

Sample size

35 participants in the preliminary BESH (No. NCT05504005).
200 participants in the expanded BESH (No. NCT05921344).
30 participants in the expanded BESH (No. NCT06512077).
No sample-size calculations were performed. Sample sizes were chosen based on similar previously published studies of non-invasive glucose blood monitoring (Stefan Pleus et al. J Diabetes Sci Technol. 15,11-18 (2020) & Anders Pors et al. ACS Sens. 2024 <https://doi.org/10.1021/acssensors.2c02756>). The numbers of samples are large enough to capture normal variation and glucose feature from Raman spectra according to the published data in this field.

Data exclusions

In the preliminary BESH (No. NCT05504005): Among all 420 sets of data, 5 spectra are lost due to technical issues.

Data exclusions	In the expanded BESH (No.NCT05921344): Among all 4800 sets of data, 24 from both hands of subject D016 were lost because the subject quit the BESH. 8 sampling points of subject D119 were lost due to technical problems. In the expanded BESH (No.NCT06512077): Among all 540 sets of data, no data lost.
Replication	We have demonstrated the replication with three independent BESHs.
Randomization	N/A - No randomization was used in this study, and all enrolled subjects were treated the same.
Blinding	N/A - Blinding was not necessary since there was no randomization nor experimental groups.

Reporting for specific materials, systems and methods

We require information from authors about some types of materials, experimental systems and methods used in many studies. Here, indicate whether each material, system or method listed is relevant to your study. If you are not sure if a list item applies to your research, read the appropriate section before selecting a response.

Materials & experimental systems

n/a	Involvement in the study
<input checked="" type="checkbox"/>	<input type="checkbox"/> Antibodies
<input checked="" type="checkbox"/>	<input type="checkbox"/> Eukaryotic cell lines
<input checked="" type="checkbox"/>	<input type="checkbox"/> Palaeontology and archaeology
<input checked="" type="checkbox"/>	<input type="checkbox"/> Animals and other organisms
<input type="checkbox"/>	<input checked="" type="checkbox"/> Clinical data
<input checked="" type="checkbox"/>	<input type="checkbox"/> Dual use research of concern
<input checked="" type="checkbox"/>	<input type="checkbox"/> Plants

Methods

n/a	Involvement in the study
<input checked="" type="checkbox"/>	<input type="checkbox"/> ChIP-seq
<input checked="" type="checkbox"/>	<input type="checkbox"/> Flow cytometry
<input checked="" type="checkbox"/>	<input type="checkbox"/> MRI-based neuroimaging

Clinical data

Policy information about [clinical studies](#)

All manuscripts should comply with the ICMJE [guidelines for publication of clinical research](#) and a completed [CONSORT checklist](#) must be included with all submissions.

Clinical trial registration	https://clinicaltrials.gov/ , No. NCT05504005, No. NCT05921344 and No.NCT06512077.
Study protocol	https://clinicaltrials.gov/
Data collection	We recruited all the participants, performed the study and collected all the data in Ruijin Hospital affiliated with Shanghai JiaoTong University School of Medicine in Shanghai of China. The data in preliminary BESH (No. NCT05504005) was collected from August to December in 2022. The data in expanded BESH (No. NCT05921344) was collected from July to September in 2023. The data in expanded BESH (No.NCT06512077) was collected in August of 2024.
Outcomes	Primary outcome: 1) Mean absolute relative deviation (MARD) of venous plasma glucose and glucose values measured by μ SORS at each time point of OGTT. 2) Consensus Error Grid (CEG) for venous plasma glucose and glucose values measured by μ SORS at each time point of OGTT. Secondary Outcome: 1) MARD for two measurement methods in different blood glucose ranges. 2) Incidence of treatment-emergent adverse events.

Plants

Seed stocks	N/A.
Novel plant genotypes	N/A.
Authentication	N/A.